Master's thesis

Spatial Localization in coupled nonlinear Micro-Cavities near self-imaging Conditions

Submitted by

Lukas Jäcker

March 3, 2022

First examiner
PD Dr. Svetlana Gurevich

Second examiner
Prof. Dr. Julien Joseph Pierre Javaloyes

Westfälische Wilhelms-Universität Münster
Fachbereich Physik
Institut für theoretische Physik

Contents

1 Introduction

Localized states (LSs) are certain confined states that appear in nonlinear systems. Their characteristics are a spatial size and correlation range much shorter than the size of the system. They can be observed in many different systems on a wide range of scales and can sometimes - in the weak dissipative limit - be interpreted as dissipative solitons. Examples are nonpropagating "hydrostatic" solitons in water [12] as well as vibrational excitations in granular media [17] or light pulses in nonlinear optics [23]. Latter - the generation of short optical pulses - has attracted a lot of scientific interest primarily due to the possible use as elementary bits in data processing. Besides other scenarios, LSs may form as connecting orbits when two homogeneous solutions coexist for the same parameter values. Another common mechanism for their appearence is the coexistence of a homogeneous and a modulated solution, leading to the so called cellular patterns [13].
In laser optics, one distinguishes two cases of LS-formation constraints. One is the possibility of creating LSs inside a laser cavity by injecting a coherent electromagnetic field. This can for example be observed in the tranverse section of broad-area semiconductor microcavities or in the temporal output of fibers [19]. In the second case the system doesn't require an external injection beam but the LSs arise from spontaneous emisson noise. These lasing LSs show fundamentally different properties the aforementioned because, unlike them, they generally appear in phase invariant systems. This regime of localization can e.g. be achieved by passive mode-locking (PML) which is a common method to achieve (ultra)short optical pulses [10]. PLM can be accomplished inside a laser cavity by combining a laser amplifier providing gain and a nonlinear loss element which is usually a saturable absorber (SA). Other than in the continous-wave operation, where the longitudinal laser modes oscillate independently, this combination of elements can induce a fixed-phase relation between the longitudinal modes of the laser's resonant cavity. The saturable absorber attenuates the continous-wave (CW) like components of the light field, while it transmits the higher intensity pulses which occur randomly in the noisy CW background. The result is a locking between the longitudinal laser modes as sketched in Fig. 1.1 which leads to the emission of short optical pulses.

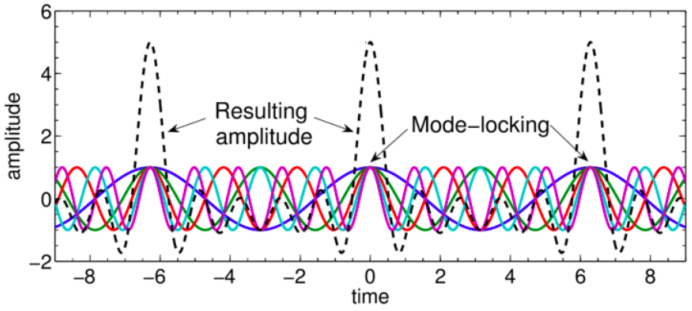

Figure 1.1: Sketch of mode locked longitudinal modes in the temporal output of a laser. Figure extracted from [16].

Usually PML occurs above the laser threshold, supported by the unstable CW-background. In this regime the number of pulses that travel in the cavity is fixed by the available gain meaning that just one stable mode-locked solution exists for a given gain value.
Recently a regime of temporal localization was predicted [11] and experimentally demonstrated [14] in a semiconductor passively mode-locked laser, operated below the lasing threshold in the long cavity regime. Other than in the regime above threshold where the

mode-locked solution emerges from the CW-solution via a Hopf-bifurcation, the PML pulses below threshold arise from saddle node bifurcations of limit cycles and become under certain conditions individually addressable phase invariant lasing LSs. For the occurrence of these LSs two conditions have to be fullfilled:

- the cavity round-trip τ_{cavity} is much larger than the slowest laser medium time scale (usually the gain recovery time τ_{gain} of approximately 0.5 ns)
- the mode-locked solution coexists with the zero intensity solution (off-solution)

These two conditions enable the coexistence of a large quantity of stable solutions, each of them being characterized by a different number of pulses per round-trip and with different arrangements. This fundamentally differs from the operation mode above threshold where the pulses are created by the CW background and the number of pulses in the cavity is therefore fixed for a given gain value (compare sketch 1.1).
A prototypical system for the generation of lasing LSs is the VCSEL-SESAM geometry, where a vertical cavity surface-emitting laser (VCSEL) is coupled to a distant semiconductor saturable absorber mirror (SESAM). In figure 1.2 the ordinary operation mode above threshold and for a short roundtrip of $\tau_{cavity} = 10\tau_{gain}$ (panels (a) and (b)) is compared to the operation mode below threshold for a long cavity with $\tau_{cavity} = 100\tau_{gain}$ (panels (c) and (d)) in a VCSEL-SESAM geometry laser setup. In the operation mode above thereshold (a,b) the intensity and the losses reach an equilibrium value, but the gain grows until it is big enough to saturate the absorber and trigger another pulse. In the long cavity regime below threshold (c,d) the gain can reach its equilibrium value without triggering another pulse. The off-solution is stable and pulses can be adressed individually, allowing arbitrary low repetition rates (i.e., LS-generation).

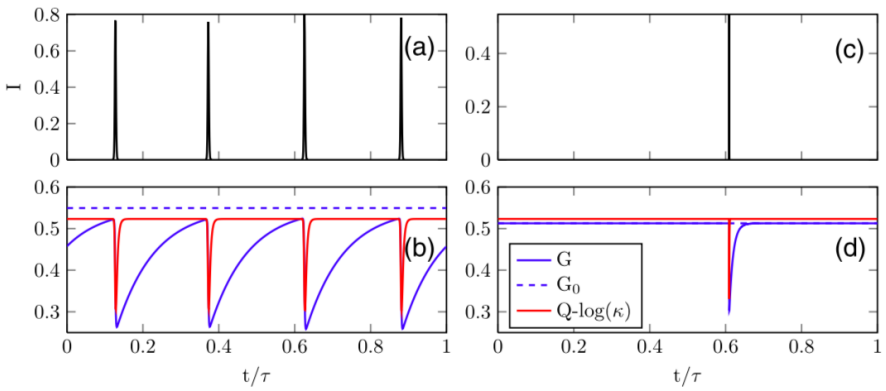

Figure 1.2: Intensity of the field (a, c) as well as gain (blue) and total losses (red) (b, d)for a semiconductor VCSEL-SESAM laser system. (a) and (b) correspond to $\tau_{cavity} = 10\tau_{gain}$ and $G_0/G_{th} = 1.1$, (c) and (d) to $\tau_{cavity} = 100\tau_{gain}$ and $G_0/G_{th} = 0.98$. The absicissa shows the time normalized to the round trip time t/τ. Figure adapted from [14].

The long cavity limit, where $\tau_{cavity} \gg \tau_{gain}$ corresponds to a distance of the two microcavities of the order of 1 m, so that the cavity round trip is $\tau_{cavity} > 10$ns. A gain recovery time of $\tau_{gain} \approx 0.5ns$ and the pulse width of approximately 10 ps imply an essential theoretical and numerical difficulty and also clarify the exact nature of these LSs: a strongly multiple timescale object in which the optical pulse of a few picoseconds

is "followed" by a long trail due to the material gain recovery that is of the order of a nanosecond [11]. Since the pulses arise from saddle node bifurcations of limit cycles another unstable solution branch exists besides the stable LS-solution and the off-solution. This unstable LS-solution plays the role of a separatrix between the stable LS-solution and the off-solution.
It was further shown [11] that the regime of LSs is compatible with an additional spatial confinement mechanism in transverse direction, leading to three dimensional dissipative localized structures, so called *light bullets* (LBs), found in the same conditions like the LSs. The system described here is a broad area gain device (a VCSEL for example) coupled to a distant saturable absorber mirror with telescopic optics, described by a truncated version of the Haus partial differential equation [10]. The lasing LBs can be understood as hybrids between temporal LS and diffractive autosolitons. In Fig. 1.3 such a LB is shown including the gain and absorber dynamics.

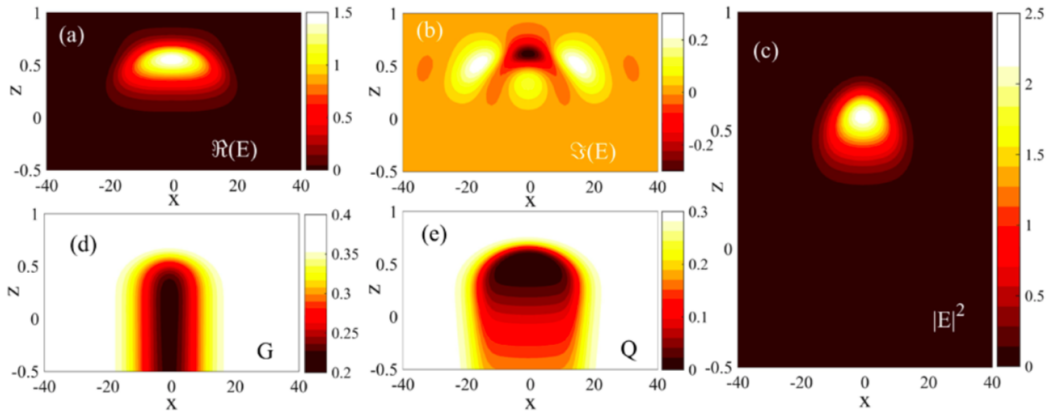

Figure 1.3: Real and imaginary parts (a), (b) and intensity (c) spatiotemporal distributions in the case of a single LB. The arbitrary phase of the LB was chosen to be zero at the peak intensity. The gain and absorption spatiotemporal profiles are represented in (d) and (e), respectively. The gain value is $G = 0.687 G_{th}$. Figure adapted from [11].

Fig. 1.3 illustrates the multiscale nature of the LB. Especially the gain stays visually unchanged after the emergence of the light bullet.
The main idea to solve the spatio-temporal dynamics of three-dimensional LBs is to seperate the longitudinal from the transverse dynamics. This is done by approximating the solution by the product of a slowly evolving transverse profile and a short pulse propagating inside the cavity. Recently it was shown [23] that the transverse field profile $A(r_\perp, t)$ is governed by an effective Rosanov equation [18]:

$$\partial_t A = (d + iB)\Delta_\perp A + f(|A|^2)A, \tag{1.1}$$

where d is the diffusion, B the diffraction and $\Delta_\perp$ the transverse laplacian. This effective equation allowed a detailed multiparameter bifurcation study and the identification of different mechanisms of instability for the transverse confinement. The solution branch of the two-dimensional single LS-solution in Fig. 1.4 (a) and (b) reveal, that the LS is stable between the saddle-node bifurcation point (SN) and the Andronov-Hopf (AH) bifurcation point (H2; thick blue line). It was found that the LS experience dominantly

either homogeneous oscillation or symmetry-breaking transversal wave radiation [23]. The inset in (b) illustrates the difference in intensity between a solution on the stable branch and a solution on the unstable branch for a given gain value.

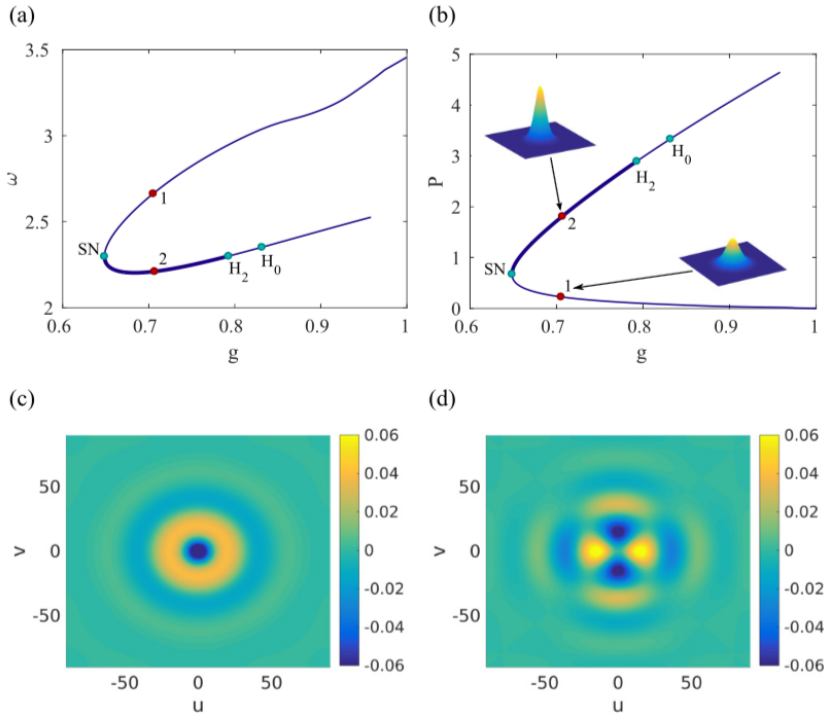

Figure 1.4: Bifurcation diagram for a two-dimensional LS in the spectral parameter (a) and the peal intensity (b) as a function of the gain g. (c) and (d) show The real parts of both n = 0 and n = 2 critical modes calculated at $g = 0.68$, respectively. Figure adapted from [23].

The Rosanov equation is already a satisfactory model to explain the spatial localization in transverse direction. The aim of this master's thesis is to advance the work of S. Gurevich and J. Javaloyes [23] (i.e. the Rosanov equation), by introducing a "hybrid" equation combining the partial differential equation (PDE) of [23] with a delay differential equation [7]. This includes a slight modification of the physical model, changing the VCSEL-SESAM-geometry (e.g. assumed in [23]) to a setup where a mode-locked integrated external-cavity surface-emitting laser (MIXSEL) is coupled to a distant mirror. A MIXSEL is basically a VCSEL with an integrated vertical saturable absorber inside the semiconductor structure [5], see Fig. 1.5. The physical phenomenon of interest in this master's thesis is the formation of transversal patterns in a semiconductor micro-cavity embedded in an optical resonator close to perfect imaging conditions. An example of these transversal patterns is given in Figure 1.6.

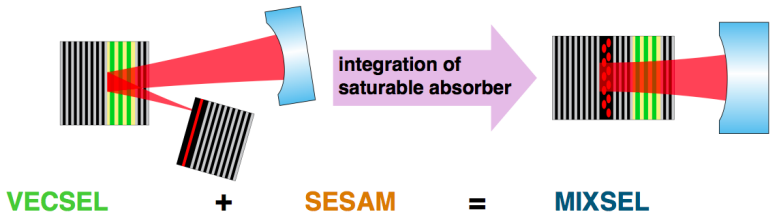

Figure 1.5: Sketch of the MIXSEL setup compared to the VCSEL-SESAM setup. It both reduces the complexity and improves the overall performance. Today MIXSELs are the semiconductor laser type with the highest achievable average output power [24]. Sketch adapted from [5].

In the Near field (i.e. in the micro-cavity) this intensity profile looks similar to a stripe pattern with an approximately Gaussian envelope, while in the far field four intensity dots occur. This intensity pattern is just one example of a variety of experimentally observed ones.

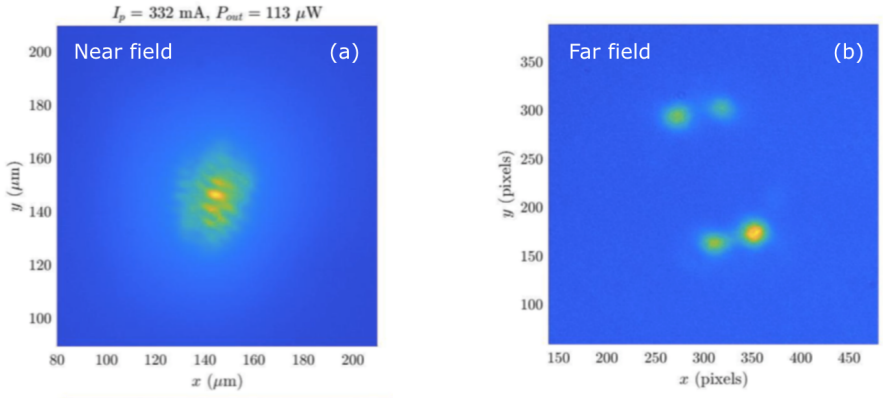

Figure 1.6: Near field (a) and far field (b) optical intensity for an VCSEL-SESAM experimental setup. Source: private communication with the examiner Svetlana Gurevich.

The aim of this master's thesis is to provide a mathematical model of the electric field inside the micro-cavity of a MIXSEL coupled to a distant mirror that shows stable solutions somehow similar to the intensity pattern shown in Fig. 1.6 and to qualitatively understand the stabilization and destabilization mechanisms involved. As aforementioned, this model is a hybrid between a PDE and a DDE and considers a cavity with imperfect imaging conditions (i.e. a realistic cavity). Since the model will be one-dimensional, the solutions of interest are something like a spatially limited comb or just multi-peak solutions, that can theoretically be combined with a Gaussian pulse in the other dimension to end up with an intensity profile comparable to the one in Fig. 1.6 (a). In the theoretical part, the model equation for the one-dimensional electric field dynamics inside the micro cavity of the MIXSEL will be derived, which is a modified Rosanov equation. This includes the prediction of stable multi-mode solutions and an introduction to the numerical methods used. In the second part, an extensive continuation and bifurcation analysis of the analytically predicted stable multi-mode solutions of the model equation will be done. In the supplement, a modification of the model equation of this master's thesis is introduced. At the end, a conclusion and an outlook for possibly future research are given.

2 Theory

2.1 Derivation of the model

The physical system considered is a mode-locked integrated external cavity surface emitting laser (MIXSEL) coupled to a distant mirror with telescopic optics near self-imaging conditions (see Figure 2.1). In this configuration, both the gain and absorber sections needed for PML are contained in the same micro-cavity.

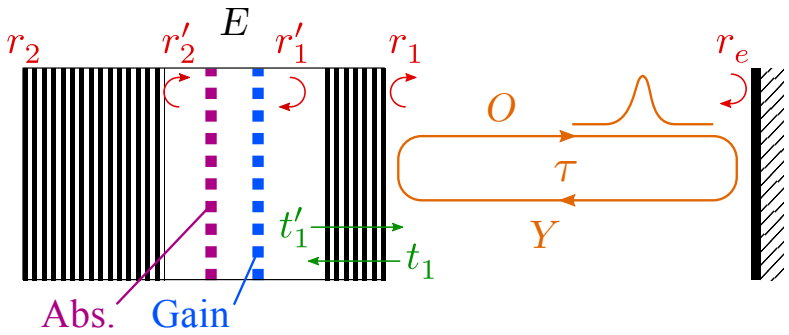

Figure 2.1: Sketch of the MIXSEL configuration laser systems basic setup. Here $E(r_\perp, t)$ is the electromagnetic field inside the micro-cavity, $O(r_\perp, t)$ the output field and $Y(r_\perp, t)$ the injection field in the external cavity. (figure adapted from [7])

The mathematical model describing the transverse electric field profile $E(r_\perp, t)$ inside the micro-cavity shown in Fig. 2.1 is:

$$\kappa^{-1}\frac{\partial E}{\partial t} = [(1-i\alpha)N_1 + (1-i\alpha_2)N_2 - 1]E + (il^2 + d)\Delta_\perp E + hY(r_\perp, t) \tag{2.1}$$

$$\gamma_1^{-1}\frac{\partial N_1}{\partial t} = J_1 - N_1 - N_1|E|^2 \tag{2.2}$$

$$\gamma_2^{-1}\frac{\partial N_2}{\partial t} = J_2 - N_2 - sN_2|E|^2 \tag{2.3}$$

The terms in Eq. (2.1) are the electric field $E(r_\perp, t)$ inside the micro-cavity of the MIXSEL with the corresponding averaged photon lifetime κ, the population inversions $N_i(r_\perp, t)$, with the Einstein-coefficients $(1-\alpha_{1,2})$ (where $\alpha_{1,2}$ are the linewidth enhancement factors of the gain and loss), the diffraction length in transverse direction inside the micro-cavity l, the diffusion d, the transverse laplacian $(il^2+d)\Delta_{r_\perp}$ and an injection field Y with the intra-cavity coupling parameter h - which is specified in the following. The carrier-Eqs. (2.2) and (2.3) include the gain- and loss-coefficients $J_{1,2}$ the population inversions $N_j(r_\perp, t)$, a saturation parameter s and the lifetimes $\gamma_{1,2}$. J_1 for now is assumed to be constant, later an non-homogeneous gain profile will be introduced. The following of the aforementioned parameters are further determinated:

$$l = \sqrt{\frac{L}{q_0}\frac{\rho_1\rho_2}{1-\rho_1\rho_2}}, \tag{2.4}$$

$$\kappa = \frac{1-\rho_1\rho_2}{\rho_1\rho_2}\frac{1}{\tau_c}, \tag{2.5}$$

$$h = \frac{(1+\rho_2)(1-\rho_1)}{1-\rho_1\rho_2}, \tag{2.6}$$

with L the cavity length, $q_0 = n\omega/c$ the carrier wave-vector, ρ_i the reflectivity of the two micro-cavity mirrors and τ_c the micro-cavity round trip time.
The feature of Eq. (2.1) is that it's a hybrid model combining the delay differential equation (DDE) considered in [7] and the partial differential equation (PDE) investigated in [23]. The first simplification introduced to equation (2.1) is the one-dimensionality of the transverse dynamics inside the micro-cavity ($r_\perp \to x$), which necessitates not further mathematical transformations. The justification for this simplification is primarily the reduction of the required mathematical and computational effort. Already the solutions of this dimensionally reduced model have confirmed to provide a good approximation of the two dimensional systems behavior, especially concerning branch-structure and the destabilization mechanisms [23]. The time delay is implicitly included in the injection field Y, which is the relevant improvement compared to the PDE used in [23], where telescopic optics with perfect self-imaging are assumed. The injection field is the reflected output field $O(r_\perp, t)$. The input-ouput relations are given by:

$$Y(x,t) = \mathcal{L}O(x,t) = \mathcal{L}(E(x,t) - Y(x,t)), \tag{2.7}$$

where $\mathcal{L}$ is the so-called round-trip transmission operator of the optical system, accounting for all optical effects occuring in one round trip, like non-perfect imaging conditions, diffraction, parabolic wavefront curvature losses and time delay due to propagation. Since we are interested in *temporal localized states* (TLSs) in the long-cavity regime, the exact time delay is irrelevant for the spatial dynamics inside the micro-cavity. This is simply because the cavity round trip is significantly larger than the gain recovery rate, i.e. the pulse traveling inside the resonator is not experiencing self-interaction. This means that the round-trip transmission operator is not time dependent and just the imaging properties of the optical resonator are relevant. Comparing the longitudinal extension of the laser system $d_{long} \sim 1m$ with the transverse domain size $L \sim 100 - 200\mu m$, the paraxial approximation seems to be appropriate. The exact optical system considered is sketched in Fig. 2.2, consisting of a lens and a mirror. This is the simplest system providing self-imaging besides just a MIXSEL and a mirror with perfect self imaging, i.e. the simplest realistic system.

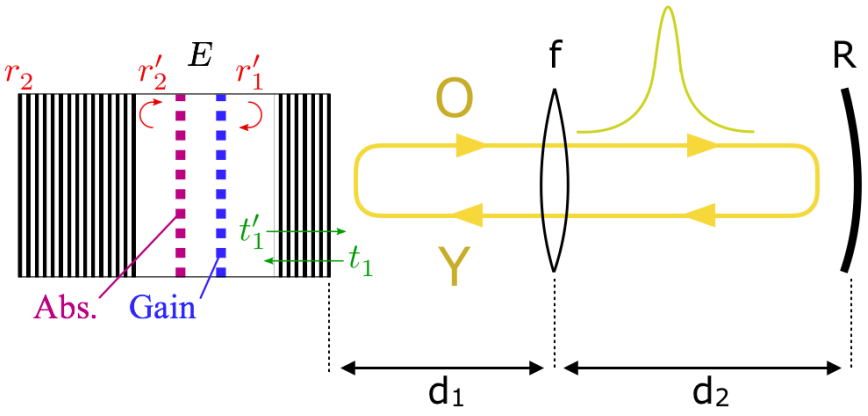

Figure 2.2: Sketch of the MIXSEL configuration laser systems basic setup with the imperfect imaging system, consisting of the laser-cavity, a lens with the focal length f and a mirror with the radius of curvature R, separated by distances d_1 and d_2.

The paraxial approximation and the neglect of aberration effects results in a linearization

of the optical transfer function. This means, that the operator $\mathcal{L}$ becomes a matrix which depends on 1+4 parameters, which are the mirror reflectivity in amplitude η and the $ABCD$-parameters of the matrix describing the first order characteristics of the optical system [1]:

$$\mathcal{L} = \begin{pmatrix} A & B \\ C & D \end{pmatrix} \qquad \text{and} \qquad det(\mathcal{L}) = AD - BC = 0. \tag{2.8}$$

The $ABCD$-matrices for a lens L of focal length f, a mirror M of curvature R and a light beam propagation over the distance d have the simple form:

$$L = \begin{pmatrix} 1 & 0 \\ \frac{-1}{f} & 1 \end{pmatrix}, \qquad M = \begin{pmatrix} 1 & 0 \\ \frac{-1}{R} & 1 \end{pmatrix}, \qquad D_n = \begin{pmatrix} 1 & d_n \\ 0 & 1 \end{pmatrix}. \tag{2.9}$$

Since the influence of a optical system composed of an apposition of different optical components on the light field E is mathematically a composition of the components $ABCD$-matrices in natural order, we can express the influence of the total optical system from Fig. 2.2 in the form of:

$$E_{n+1} = (D_1 L d_2 M M D_2 L d_1) E_n = T E_n \tag{2.10}$$

In that way the transfer matrix $T(f, R, d_1, d_2)$ can be calculated:

$$T = \left(\begin{array}{c|c} 1 + \frac{1}{f} - (\frac{2}{f} - \frac{1}{R^2})d_1 - (\frac{2}{f} - \frac{1}{R^2})d_2 & 2(d_1 + d_2) - (\frac{1}{f} + \frac{1}{R})d_1^2 - \frac{1}{R^2}d_2^2 \\ + \frac{1}{R^2}d_2^2 + (\frac{1}{f} + \frac{1}{fR^2})d_1 d_2 & + 3(\frac{1}{R^2} + \frac{1}{f})d_1 d_2 + \frac{1}{f^2}d_1 d_2^2 + \frac{1}{fR^2}d_1 d_2^2 \\ \hline -\frac{1}{R^2} - \frac{2}{f} + (\frac{1}{f^2} + \frac{1}{fR^2})d_2 & 1 - (\frac{1}{f} + \frac{1}{R^2})d_1 - (\frac{1}{f} + \frac{1}{R^2})d_2 \\ & + (\frac{1}{f^2} - \frac{1}{R^2})d_1 d_2 \end{array}\right) \tag{2.11}$$

Since the deviation from self-imaging is very small, the transfer matrix is just slightly different from the identity and we fix $A = D = 1$ in our first order approximation, while B and C are small. Important is primarily the influence of a translational displacement of the lens or the mirror (i.e., the distances d_1 and d_2) on the parameters B and C. From the transfer matrix T, we can see that C just depends on d_2, while B depends both on d_1 and d_2. For the experiment this obviously means, that moving the lens changes B, while moving the mirror canges both B and C. The explicit result for the transfer matrix (Eg. (2.11)) is not used in the following, but the connection between lens- or mirror-displacement and the parameter values is important to the experimenter. To calculate the influence of an optical system on an incoming light field O using a wave-optical approach, the generalized Huygens-Fresnel integral has to be solved. For a first order optical system characterized by an ABCD-matrix, this integral takes the form [6, 15] :

$$E(x, l) = \sqrt{\frac{-i}{\lambda B}} e^{ikl} \int_{-\infty}^{\infty} E(\alpha, 0) \times \exp\left[\frac{i\pi}{\lambda B}(A\alpha^2 - 2x\alpha + Dx^2)\right] d\alpha. \tag{2.12}$$

The quadratic phase form can be factored to the expression $(A\alpha^2 - 2x\alpha + Dx^2) = A\left(\alpha - \frac{x}{A}\right)^2 + \left(D - \frac{1}{A}\right)x^2$, which leads to

$$E(x,l) = \sqrt{\frac{-i}{\lambda B}} e^{ikl} e^{i\frac{\pi}{\lambda}\frac{1}{B}(D-\frac{1}{A})x^2} \int_{-\infty}^{\infty} E(\alpha,0) \times \exp\left[\frac{i\pi A}{\lambda B}\left(\alpha - \frac{x}{A}\right)^2\right] d\alpha \tag{2.13}$$

Using the simplification $\frac{1}{B}\left(D - \frac{1}{A}\right) = \frac{AD-1}{AB} = \frac{BC+1-1}{AB} = \frac{C}{A}$ we get:

$$E(x,l) = e^{i\frac{\pi C}{\lambda A}x^2} \int_{-\infty}^{\infty} E(\alpha,0) \times \sqrt{\frac{-i}{\lambda B}} \exp\left[\frac{i\pi A}{\lambda B}\left(\alpha - \frac{x}{A}\right)^2\right] d\alpha \tag{2.14}$$

This result can be expressed as a convolution evaluated in $\frac{x}{A}$

$$E(x,l) = e^{ikl} e^{i\frac{\pi C}{\lambda A}x^2} (E * H_{A,B})\left(\frac{x}{A}\right) \tag{2.15}$$

where

$$H_{A,B}(\alpha) = \sqrt{\frac{i}{\lambda B}} \exp\left[\frac{i\pi A}{\lambda B}\alpha^2\right]. \tag{2.16}$$

The result $H_{A,B}$ can be best viewed in Fourier-space:

$$\mathcal{F}[H_{A,B}(\alpha)] = \int \sqrt{\frac{i}{\lambda B}} \exp\left[\frac{i\pi A}{\lambda B}x^2\right] e^{ikx} dx = \frac{1}{\sqrt{A}} \exp\left[-i\frac{\lambda B}{4\pi A}k^2\right] \tag{2.17}$$

The last term can be translated back to the time domain by using that the factor ik in the frequency domain corresponds to the spatial partial derivative operator $\frac{\partial}{\partial x}$ in the time domain. As already mentioned $A = 1$, so we end up with:

$$\mathcal{F}\left[\frac{1}{\sqrt{A}} \exp\left[-i\frac{\lambda B}{4\pi A}k^2\right]\right] = \exp\left[i\frac{\lambda B}{4\pi}\Delta_x\right] \tag{2.18}$$

In the limit $B = 0$ - which we are very close to - the convolution kernel in Eq. (2.15) converges to a Dirac Delta and the Fresnel transformation operator of the field E yields:

$$\mathcal{L} = \eta \exp\left[i\frac{\pi}{\lambda}Cx^2\right] \exp\left[i\frac{\lambda B}{4\pi}\Delta_x\right] \tag{2.19}$$

Using again the assumption that the magnitude of the imaging systems imperfections that we want to examine is small, the operator $\mathcal{L}$ is a near identity operator, that we can expand. In this case the imaging conditions are almost perfect (good cavity limit) and the first order Taylor series expansion reads:

$$\mathcal{L} \simeq \eta(1 + \delta\mathcal{L}) = \eta\left(1 + i\frac{\pi}{\lambda}Cx^2 + i\frac{\lambda B}{4\pi}\Delta_x\right). \tag{2.20}$$

Now Eq. (2.7) can be approximated

$$Y \simeq \eta(1 + \delta\mathcal{L})(E - Y) \tag{2.21}$$

Since $(1 + \delta\mathcal{L})$ is a near identity operator, Eq. (2.21) can be transformed and Taylor-expanded in $\delta\mathcal{L}$

$$Y \simeq \frac{1 + \delta\mathcal{L}}{1 + \eta + \eta\delta\mathcal{L}}\eta E \simeq \left[\frac{\eta}{1+\eta} + \frac{\eta}{(1+\eta)^2}\delta\mathcal{L}\right]E + \mathcal{O}(\delta\mathcal{L}^2). \tag{2.22}$$

This first order approximation of Y is inserted in the main Eq. (2.1), yielding

$$\frac{1}{\kappa}\frac{\partial E}{\partial t} = \left[(1-i\alpha)N_1+(1-i\alpha_2)N_2-1-(il_\perp^2+d)\Delta_\perp+\frac{h\eta}{1+\eta}+\frac{h\eta}{(1+\eta)^2}\left[i\frac{\pi}{\lambda}Cx^2+i\frac{\lambda B}{4\pi}\Delta_x\right]\right]E. \tag{2.23}$$

Now the carrier equations (2.2) and (2.3) need to be solved. The variables $J_{1,2}$ correspond to the gain without any laser light in the cavity, the terms $N_{1,2}$ represent the spontaneous and $sN_{1,2}|E|^2$ the stimulated emission, respectively. The main idea is to solve the carrier equations by considering the multiple timescale nature of the the longitudinal and transversal dynamics of the electric field propagating inside the resonator. Compared to the short optical pulse in longitudinal direction, the transverse profile dynamics are extremely slow. Regarding the temporal evolution of the electric field E inside the micro-cavity, this means, that we can factor $E(t) = p_{fast}(t) \cdot A(t)$. Here $p_{fast}(t)$ is a very short, normalized (and dimensionless) pulse oscillating with the frequency $1/\tau_c$, where τ_c is the cavities round-trip time. During the transition of this very short pulse, the terms including the intensity $|E|^2$ in equation 2.2 and 2.3 are highly dominant and we can approximate [23, 11]:

$$\gamma_1^{-1}\frac{\partial N_1}{\partial t} = -N_1|E|^2 \qquad \gamma_2^{-1}\frac{\partial N_2}{\partial t} = -sN_2|E|^2 \tag{2.24}$$

The solutions of these equations are:

$$N_{1,f} = N_{1,i} \cdot e^{-|E|^2} = J_1 \cdot e^{-|E|^2} \qquad N_{2,f} = s \cdot J_2 \cdot e^{-|E|^2} \tag{2.25}$$

Where $N_{1,i}$ and $N_{1,f}$ is the gain before and after the pulse. The gain before the pulse (i.e. for the off-solution) is just J_1. By inserting the seperation ansatz for the electric field $E(t) = p_{fast}(t) \cdot A(t)$ into equation 2.23 and utilizing the expessions for $N_{1,f}$ and $N_{2,f}$ an equation for the slowly evolving part A of the electric field inside the micro cavity can be derived. A detailed explanation of this derivation is done in [8]. The result is a modified version of the Rosanov equation in one dimension [18]:

$$\begin{aligned}\frac{\partial A}{\partial t} =& \Bigg[(1-i\alpha_1)J_1(r_\perp)h\Big(|A|^2\Big)+(1-i\alpha_2)J_2h\Big(s|A|^2\Big)\\ &-k+i\tilde{C}x^2+\Big(d+i\tilde{B}\Big)\Delta_x\Bigg]A,\end{aligned} \tag{2.26}$$

where $h(P) = (1-e^{-P})/P$, $P = |A|^2$. This is the final equation investigated in the following. Due to the phase shift invariance the electric field can be written as $A = A_0 \cdot e^{-i\omega t}$. The translational invariance is broken due to the presence of the potential. Besides a constant gain parameter J_1, also gain profiles $J_1(r_\perp)$ with a gaussian shape are going to be considered in the following. The parameters of Eq. (2.26) are defined as:

$$\tilde{B} = \frac{\lambda B}{4\pi}\frac{h\eta}{(1+\eta)^2}+l_\perp^2, \tag{2.27}$$

$$\tilde{C} = \frac{\pi}{\lambda}C\frac{h\eta}{(1+\eta)^2}, \tag{2.28}$$

$$k = 1-\frac{h\eta}{1+\eta}. \tag{2.29}$$

In total the system includes 12 main parameters, that are listet in the following tabular including their "standard" values used for all calculations, if not explicitly stated differently.

parameter	value	unit
α_1	1.5	$[a.u.]$
α_2	0.5	$[a.u.]$
J_1	0.062	$[a.u.]$
J_2	-0.06	$[a.u.]$
h	1.98	$[a.u.]$
s	15	$[a.u.]$
η	0.95	$[a.u.]$
d	0.005	$[\mu m^2]$
l	1	$[\mu m]$
B	-18	$[\mu m]$
$\tilde{B}$	0.2914	$[\mu m]$
C	$-5 \cdot 10^{-5}$	$[1/\mu m]$
$\tilde{C}$	$-7.77 \cdot 10^{-5}$	$[1/\mu m]$
Lx	200	$[\mu m]$

Besides these parameters, the spectral parameter ω is a free parameter included in the required auxiliary condition for frequency shift invariance.

2.2 Hermite-Gaussian Modes

2.2.1 Fundamental Gaussian Mode

In the following the modified Rosanov-Eq. (2.26) is simplified and solved analytically for small field amplitudes. The simplifications used are a uniform gain profile J_1, a vanishing intensity and zero diffusion (d=0). Considering this we are left with the equation:

$$\frac{\partial A}{\partial \sigma} = \left[(1 - i\alpha_1)J_1 + (1 - i\alpha_2)J_2 - k + i\tilde{C}r_\perp^2 + i\tilde{B}\Delta_\perp\right]. \tag{2.30}$$

Assuming a spatio-temporal gaussian shaped profile of the electric field $A_0(x,t) = e^{-i\omega t}e^{-x^2/(2\sigma^2)}$ as the initial solution we can write equation 2.30 in the form:

$$-i\omega A_0 = (-i\alpha_1 J_1 - i\alpha_2 J_2) + i\tilde{C}x^2 A_0 + i\tilde{B}\left(.\frac{x^2}{\sigma^4} - \frac{1}{\sigma^2}\right)A_0 \tag{2.31}$$

Here k is removed by the threshold condition $J_1 + J_2 - k = 0$. Because Eq. (2.35) represents a steady state, the derivative in x must be vanishing, which leads to:

$$\tilde{C} = -\frac{\tilde{B}}{\sigma^4} \quad \Longleftrightarrow \quad \sigma^2 = \sqrt{-\frac{\tilde{B}}{\tilde{C}}}. \tag{2.32}$$

This means, that the frequency shift ω can be written as:

$$\omega = \alpha_1 J_1 - \alpha_2 J_2 + \frac{\tilde{B}}{\sigma^2} = \alpha_1 J_1 + \alpha_2 J_2 - \tilde{C}\sqrt{-\frac{\tilde{B}}{\tilde{C}}}. \tag{2.33}$$

2.2.2 Higher Order Hermite-Gaussian Modes

To find more complex solutions for equation 2.30, we incorporate the Hermite polynomials $H_n(x)$, where $H_n(x) = (-1)^n e^{x^2} \frac{d^n}{dx^n} e^{-x^2}$ is the n-th Hermite polynomial [3]. The Product of a Hermite polynomial and a Gauß-function $\psi_n(y) = H_n(y) e^{-\frac{y^2}{2}}$ solves the following equation:

$$\frac{\partial \psi_n}{\partial y^2} + (2n + 1 - y^2)\psi_n = 0 \tag{2.34}$$

This equation is equivalent to the Schroedinger equation of an harmonic oscillator, which is also the non-dissipative approximation of the main equation 2.26. If the ansatz $A_0(x,t) = e^{-i\omega_n \sigma} \psi_n \left(\frac{x}{\sigma}\right)$ is used for equation 2.30, we get similiar to the case of a simple Gauß-function:

$$-i\omega_n \psi_n \left(\frac{x}{\sigma}\right)^2 = \left(-i\alpha_1 J_1 - i\alpha_2 J_2 + i\tilde{C}x^2 - i\frac{\tilde{B}}{\sigma^2}\left[2n + 1 - \left(\frac{x}{\sigma}\right)^2\right]\right)\psi_n \left(\frac{x}{\sigma}\right)^2 \tag{2.35}$$

This equation can be solved in the same way like equation 2.30 by setting $\sigma = \sqrt{-\tilde{B}/\tilde{C}}$ and the free parameter ω to:

$$\begin{aligned} \omega_n &= \alpha_1 J_1 - \alpha_2 J_2 - \sqrt{-\tilde{B}\tilde{C}}(2n+1) \quad for \quad \tilde{C} > 0 \\ \omega_n &= \alpha_1 J_1 - \alpha_2 J_2 + \sqrt{-\tilde{B}\tilde{C}}(2n+1) \quad for \quad \tilde{C} < 0 \end{aligned} \tag{2.36}$$

This means, that the diffraction $\tilde{B}$ and potential $\tilde{C}$ need to have opposite signs, in order to get a positive mode width. Figure 2.3 visualizes the ($\tilde{B}$,$\tilde{C}$)-plane to illustrate this.

$$mode - width: \qquad \sigma^2 = \sqrt{-\frac{\tilde{B}}{\tilde{C}}}$$

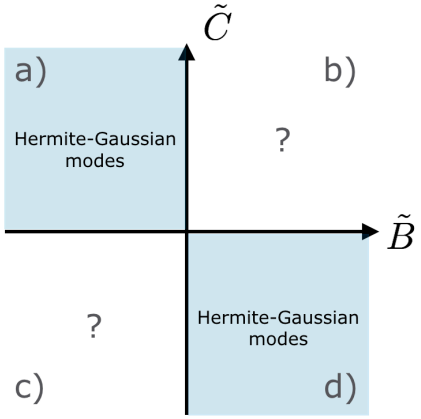

Figure 2.3: The four quadrants of the ($\tilde{B}$,$\tilde{C}$)-plane, corresponding to the four possible combinations of the two parameters. In the quadrants (a) and (d) $\tilde{B}$ and $\tilde{C}$ have opposite signs, i.e. stable Hermite-Gauß modes can exist. In the quadrants b) and c) the signs of the parameters are equal and Hermite-Gauss modes can not exist, due to the theoretical derivation.

2.3 Direct Numerical Simulation

The direct numerical simulations (DNSs) used in this master's thesis are based on the *split-step Fourier method* (SSFM) [22]. This numerical method is part of the family

of pseudo-spectral methods and is routinely used to solve nonlinear partial differential equations like the nonlinear Schrödinger-equation. The basic idea behind the method is to "split" the equation into a linear part, which is suitable to be handled in the frequency domain and a (linear or nonlinear) part, which solution can better be calculated in the time domain. This is normally done by performing half a step in the time domain, then one step in the frequency domain and again a half step in time domain; i.e. the time step is "splitted". The main equation states:

$$\begin{aligned}\frac{\partial A_0}{\partial \sigma} =& \Bigg[(1-i\alpha_1)J_1(x)h\Big(|A_0|^2\Big) + (1-i\alpha_2)J_2h\Big(s|A_0|^2\Big) \\ & - k + i\omega + i\tilde{C}x^2 + \Big(d + i\tilde{B}\Big)\Delta_\perp\Bigg]A_0.\end{aligned} \tag{2.37}$$

The right hand side of this equation now gets "splitted" into a linear part

$$L = (d + i\tilde{B})\Delta_x \tag{2.38}$$

and a nonlinear part

$$N(|A|^2) = (1-i\alpha_1)J_1(x)h(|A|^2) + (1-i\alpha_2)J_2h(s|A|^2) - k + i\omega + i\tilde{C}x^2. \tag{2.39}$$

Now Equation (2.37) can be written as:

$$\partial_\sigma A_0 = LA_0 + NA_0. \tag{2.40}$$

The numerical solution for a defined step size h is calculated in three steps. The first step is a half step ($h/2$) in the time domain and gives the intermediate result A_1:

$$A_1 = A_0 + \frac{h}{2}A_0N(|A_0|^2). \tag{2.41}$$

The second step is performed in the frequency domain, while the nonlinear contribution is neglected. The intermediate solution is Fourier-transformed via the fast Fourier transformation $\mathcal{F}$ (FFT) and (if L is a differential operator with constant coefficients only) multiplied with the factor $exp(-(d+iB)k^2\Delta t)$, which is the spatial derivative in Fourier space. Afterwards the solution is transformed back to the space-time-domain using the inverse fast Fourier transformation ($\mathcal{F}^{-1}$):

$$A_2 = \mathcal{F}^{-1}\Big[e^{-(d+iB)k^2\Delta t}\cdot\mathcal{F}(A_1)\Big]. \tag{2.42}$$

To conclude the split step Fourier-method another half time step is executed:

$$A_{final} = A_2 + \frac{h}{2}A_2N(|A_0|^2). \tag{2.43}$$

2.4 Numerical Path Continuation

Path-continuation is the name for a group of algorithms used to obtain branches of different types of solutions to nonlinear equations. More specific this means, that stationary solutions can be traced with respect to a changing control parameter to numerically construct bifurcation diagrams [21]. Here a short introduction to numerical path continuation is given. For a more detailed explanation, see [4, 20, 21]. We can generally formulate the nonlinear problem as a system of differential equations of the form:

$$\mathbf{M}\frac{d\mathbf{u}}{dt} = -\mathbf{G}(\mathbf{u}, \lambda). \tag{2.44}$$

Here vectors and matrices are represented in bold face. The solution $\mathbf{u} = [u_j]$, (j=1,...,n) is a vector of the n unknown variables. $\mathbf{G}$ is the vector consisting of the right hand sides of the ODEs. In the context of FEM (finite element method) discretizations as in PDE2PATH - which is used in this master's thesis - $\mathbf{M}$ is the so-called mass matrix. Obviously $\mathbf{M}$ is not necessary for the computation of steady solutions of equations, but it influences the spectrum of the linearization around a steady solution. With numerical continuation only stationary solutions can be traced with respect to a changing control parameter λ, which is in general an n-dimensional parameter vector λ, but first we set n=1:

$$\mathbf{G}(\mathbf{u}, \lambda) = 0. \tag{2.45}$$

The continuation method used in this master's thesis is the pseudo-arclength continuation [2]. This continuation method provides the advantage, to follow solution branches through saddle node-bifurcations. This is not possible with natural parameter continuation, where a fixed step size in the control parameter λ is required. This scheme fails at turning points, where the branch of the solution turns around. In this sense arclength is the "ideal" parameterization of a curve. Pseudo arclength is an approximation of the arclength in the tangent space of the curve, i. e. the resulting natural continuation method makes a step in pseudo-arclength s (rather than λ). The difference between both methods is presented in Fig. 2.4.

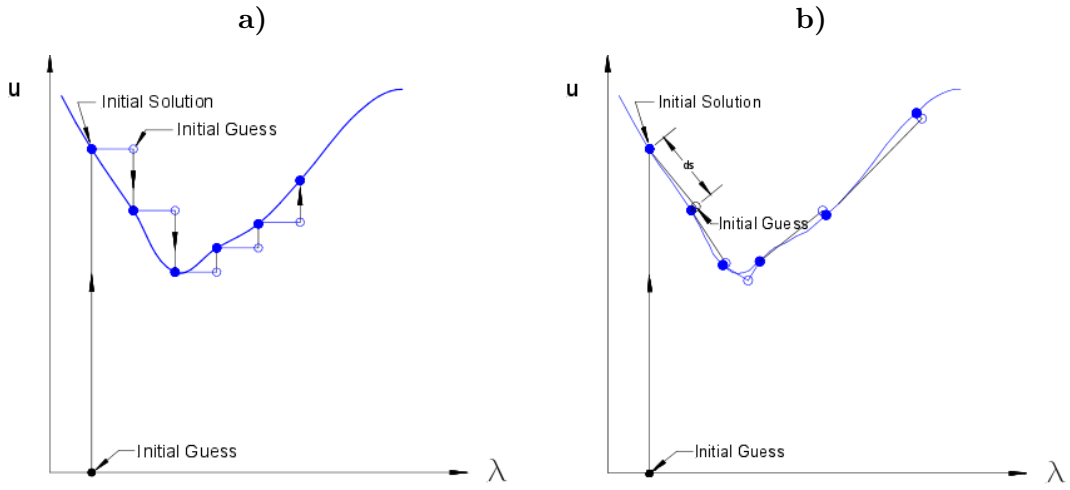

Figure 2.4: Sketch of natural (a) and pseudo-arclength (b) continuation [2].

In the following we take a deeper look on how the continuation of steady solutions with the pseudo-arclength method works.

Continuation of Branches of Steady Solutions

Using arclength continuation, the original control parameter λ as part of the solution vector has to be parametrized in the arclength s. For that we consider an arc or "branch" $s \to z(s) := (u(s), \lambda(s))$. Note that λ in general is an n-dimensional parameter vector, but first we set n=1. The extended system of initial equations we need for the arclength continuation, is of the form:

$$\mathbf{H}(\mathbf{u}, \lambda) = \begin{pmatrix} \mathbf{G}(\mathbf{u}, \lambda) \\ \mathbf{p}(\mathbf{u}, \lambda, s) \end{pmatrix} = 0. \tag{2.46}$$

To derive p, we can start with a local approximation of the arclength from Fig. 2.4 using the Pythagorean theorem:

$$|\Delta \mathbf{u}|^2 + (\Delta \lambda)^2 = (\Delta s)^2. \tag{2.47}$$

We formulate $|\Delta \mathbf{u}|^2$ using the forward difference and multiplie that with $\frac{\Delta s}{\Delta s}$

$$|\Delta \mathbf{u}|^2 = (\mathbf{u}_{j+1} - \mathbf{u}_j) \frac{(\mathbf{u}_{j+1} - \mathbf{u}_j)}{\Delta s} \Delta s \approx (\mathbf{u}_{j+1} - \mathbf{u}_j) \frac{\partial \mathbf{u}}{\partial s}\bigg|_j \Delta s, \tag{2.48}$$

the control parameter can be defined in the same way:

$$|\Delta \lambda|^2 \approx (\lambda_{j+1} - \lambda_j) \frac{\partial \lambda}{\partial s}\bigg|_j \Delta s. \tag{2.49}$$

Inserting equation (2.48) and (2.49) in equation (2.47) we end up with $\mathbf{p}$ from equation (2.46):

$$\mathbf{p}(\mathbf{u}, \lambda, s) \approx (\mathbf{u}_{j+1} - \mathbf{u}_j) \frac{\partial \mathbf{u}}{\partial s}\bigg|_j + (\lambda_{j+1} - \lambda_j) \frac{\partial \lambda}{\partial s}\bigg|_j - \Delta s = 0 \tag{2.50}$$

For all continuation and bifurcation work of this Master's thesis the MATLAB-based framework PDE2PATH [9] is used.

3 Results

3.1 The fundamental Gaussian Mode

For all bifurcation studies the continuation and bifurcation package PDE2PATH was used [9]. The predictions made with PDE2PATH were checked by DNSs of the spatiotemporal dynamics of the system. The initial guesses of the Hermite-Gaussian modes for the PDE2PATH implementations were also generated by DNSs. The first continuation done is a bifurcation diagram of the fundamental Gaussian mode (see Fig. 3.1). Due to it's huge range of stability the fundamental mode was easy to find with DNSs.

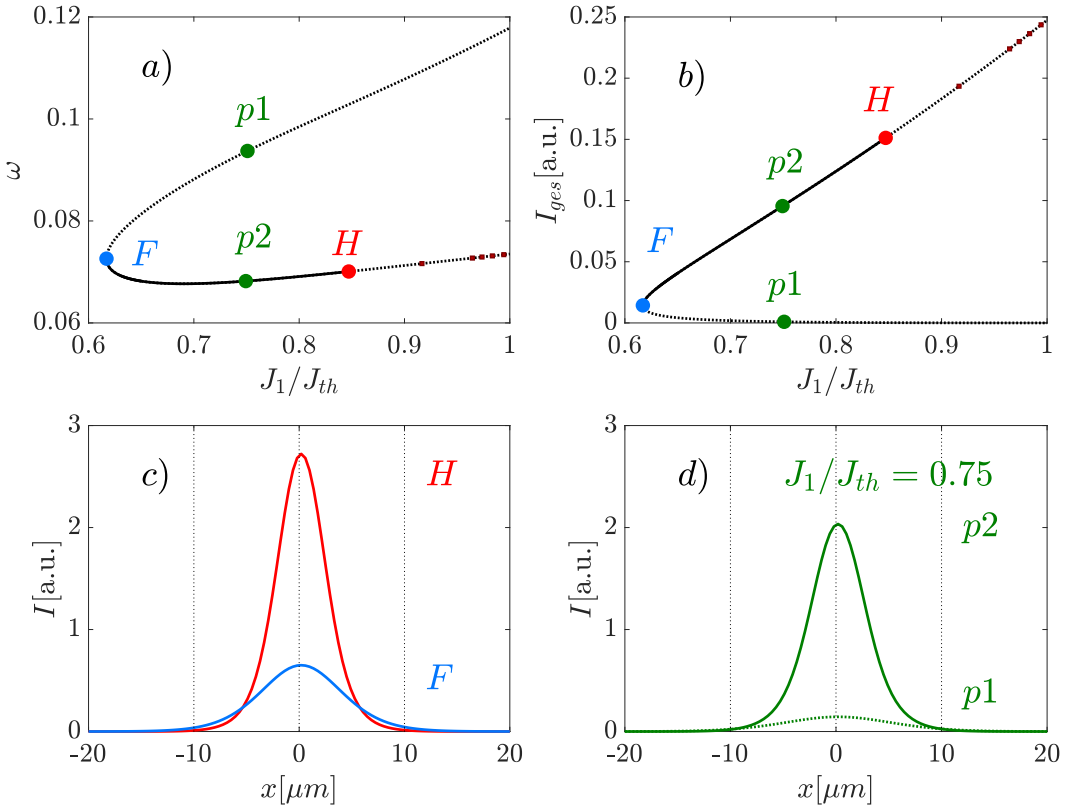

Figure 3.1: Bifurcation diagram of the fundamental Gaussian mode H_0. The spectral parameter ω and the total intensity I_{ges} with respect to the primary continuation parameter J_1/J_{th} are shown in (a) and (b). The continous part of the line represents the stable range of the solution-branch, while the unstable part is illustrated by the dotted line. The range of stability is limited by a saddle-node bifurcation F (blue point) towards low gain and an Andronov-Hopf bifurcation H (red point) towards high gain. The intensity profiles at the fold (blue) and Hopf bifurcation point (red) are displayed in (c), while the ones of the points $p1$ and $p2$ - for a gain value of $J_1/J_{th} = 0.75$ are shown in panel (d).

Figure 3.1 (a) and (b) show the branch of the fundamental Gaussian mode H_0 in the spectral parameter ω as well as the intensity I_{ges}, as a function of the relative gain value J_1/J_{th} (where J_{th} is the threshold gain of the laser). The H_0-branch arises from a saddle-node bifurcation F (blue dot) and consists of a high- and a low-intensity branch.

The high-intensity branch is stable from its emergence at the saddle point up to a maximum current of around $j_1/j_{th} = 0.845$. At this current the branch looses its static stability. The low-intensity branch that emerges from the same saddle point is always unstable and plays the role of a separatrix between the high-intensity solution and the off-solution. To visualize the significant difference in intensity between the low and the high-intensity branch, two solutions for $j_1/j_{th} = 0.75$ are shown in Fig. 3.1 (d). The dotted intensity profile corresponds to the unstable solution at point $p1$, while the solid green line corresponds to the stable solution at point $p2$. The Hopf point at $J_1/J_{th} = 0.845$, which is limiting the range of static stability of the H_0-mode is the most interesting point to investigate. The corresponding spectrum of eigenvalues and the real and imaginary part of the critical eigenfunction ψ_0 are shown in Fig. 3.2.

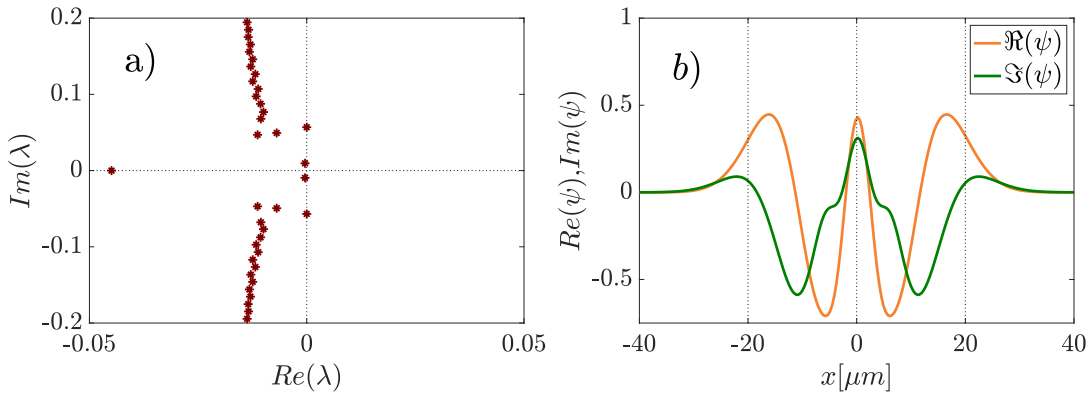

Figure 3.2: (a) The spectrum of eigenvalues for the Hopf point limiting the stable branch of the H_0 mode (see Fig. 3.1). (b) The real (orange) and imaginary part (green) of the corresponding critical eigenfunction ψ_0 at the Hopf point.

As expected, a pair of complex conjugate eigenvalues is crossing the imaginary axis (panel (a)), indicating a Hopf bifurcation. A vertical line of eigenvalues correspond to a conservative system, the dissipative terms cause the modification near the x-axis and the slight deviation of the line of eigenvalues distant the x-axis from a perfectly vertical arrangement. The symmetric real and imaginary part of the critical eigenfunction (Fig. 3.2 (b)) indicates that the perturbation at the Hopf point is symmetric. All solutions on the stable part (solid line) of the H_0 branch (between fold and Hopf point) are static solutions, since the continuation-algorithm is only able to find solutions with vanishing time derivative. However beyond the Hopf point for gain values $J_1/J_{th} > 0.845$, the mode gets destabilized via symmetric oscillations, i.e. breathing of the modes profile. However also beyond the Hopf point oscillating solutions do exist. A spatio-temporal behavior of such an oscillating, stable solution is exemplarily shown in Fig. 3.3 (a).

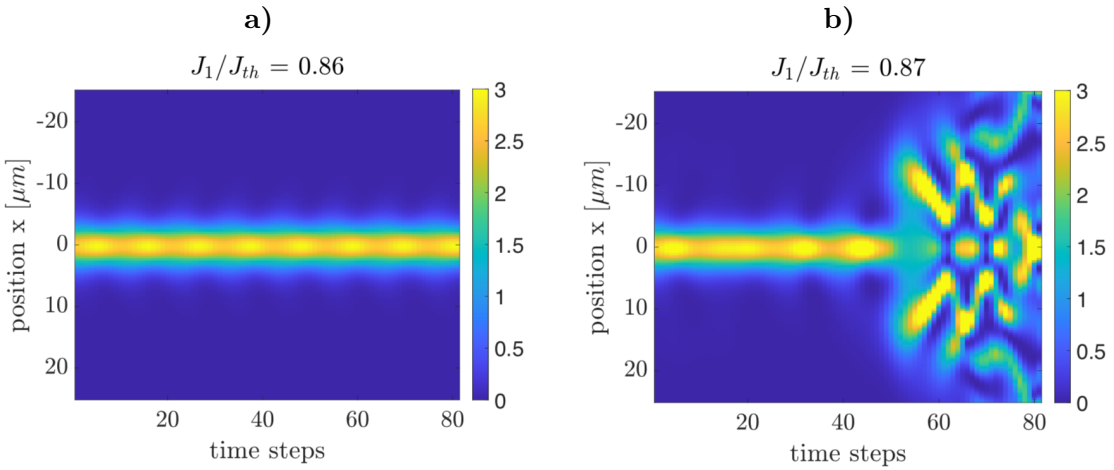

Figure 3.3: Temporal dynamics of the intensity profiles from unstable sections of the H_0 branch, the y-axis visualizes the inner 25% (50 μm) of the cavity, x-axis shows the number of steps in the DNS. (a) shows the stabily oscillating H_0 mode for $J_1/J_{th} = 0.86$, while in (b) the mode collapses symmetrically for $J_1/J_{th} = 0.87$.

As expected by the symmetry of the real and imaginary part of the critical eigenfunction in Fig. 3.2, the H_0 mode is also oscillating symmetrically for gain values slighty above $J_1/J_{th} = 0.845$ (the gain value of the Hopf bifurcation). If the gain value is increased to $J_1/J_{th} = 0.87$ the mode collapses.
Figure 3.4 (a) and 3.4 (b) show stability diagrams in the (J_1/J_{th}, α) plane for fixed values of $\alpha_2 = 0.5$ (a) or $\alpha_1 = 1.5$ (b). One linewidth enhancement factor is varied, while the other is fixed. The results show an increasing range of stability towards higher α_1 values. While the position of the fold point remains almost constant, the Hopf point moves to significantly higher currents. The change of the stability range depending on $alpha_2$ is the exact opposite, it decreases mainly due to the shift of the Hopf point. These results are in very good agreement with those in [23].

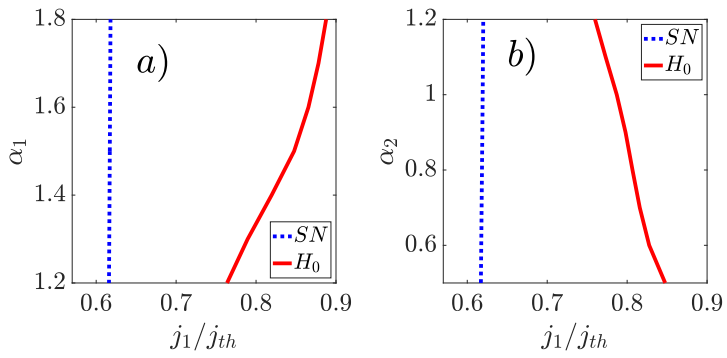

Figure 3.4: Stability diagrams showing the position of the fold (blue) and the Hopf bifurcation (red) in dependence of the linewidth enhancement factors of the gain (α_1) and the absorption (α_1). The distance between the fold and the Hopf bifurcation indicates the stable range of the solution branch of the fundamental Gaussian mode. Other parameter values are $\tilde{B} = 0.2914$, $\tilde{C} = -7.7 \cdot 10^{-5}$.

3.2 Higher Order Hermite-Gaussian Modes

The next step was to investigate the appearence of the theoretically predicted higher order Hermite-Gaussian modes. Knowing the parameters of the H_0 mode and using the calculated intensity profile of the modes as an initial guess, it was pretty easy to find the H_1-mode and the higher order modes via direct numerical simulations and to further implement them into the continuation algorithm of PDE2PATH [9].
Figure 3.5 shows the (J_1/J_{th}, ω)-diagram of the first 9 Hermite-Gaussian modes (b), including a detail picture of the most dynamic region around the fold points (a). The representation in ω is choosen for better clarity compared to the intensity. All branches arise from-saddle node bifurcations at around $J_1/J_{th} \approx 0.61 - 0.62$ and are equidistantly spaced to each other in ω, which is especially true for the low-intensity parts of the branches (above the fold bifurcation). The fundamental mode (black) exhibits the largest range of stability, followed by the H_1 and H_2-mode. The stable part of the branch of the fundamental mode is limited by the saddle node bifurcation at around $J_1/J_{th} \approx 0.617$ and a Hopf bifurcation at $J_1/J_{th} \approx 0.845$.

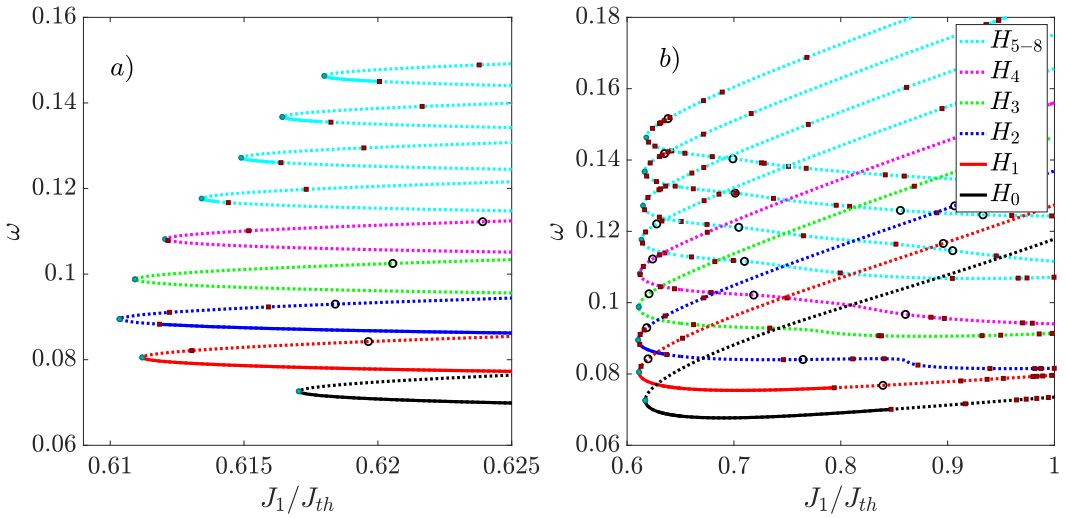

Figure 3.5: The first 9 Hermite-Gaussian branches H_0-H_8. The spectral parameter ω as a function of j_1/J_{th}. (b) shows all the branches over the biggest part of their existence from $j_1/J_{th} \approx 0.6$ to the threshold $j_1/J_{th} = 1$. The range of stability of the H_0 mode is the largest, as expected. Solid lines represent the stable part of the branches, dotted lines the unstable part. Saddle-node bifurcations are marked with green dots, Hopf bifurcations with red dots and branching points with small black circles.

The H_1-mode is stable from the saddle-node bifurcation at $J_1/J_{th} \approx 0.611$ to a Hopf bifurcation at $J_1/J_{th} \approx 0.798$. Interestingly, the mecanism of instability changes from H_1 to H_2. The stabile regime is no longer limited by the saddle-node bifurcation but by a Hopf bifurcation close to the fold point. The stability range shrinks significantly from H_1 to H_2 and is limited by two Hopf bifurcations. The H_3 got no stable regime, while the higher modes H_4 to H_4 got the same stability mechanism like H_0 and H_2 with a fold limiting the stability to smaller j_1/J_{th} values but with much smaller stability ranges (see Fig. 3.5 (a)). The stability range grows continously and approximately linear from H_4 to H_8, which can be caused by the fact, that die higher modes experience a relatively

higher stabilizing potential C due to their wider spatial expansion. When modifying the parameters $\tilde{B}$ and $\tilde{C}$, this behavior - as we will see later - can also be found for the other modes. As later shown in the parameter studies, the ranges of stability of the higher order modes can be increased by vary $\tilde{B}$ or $\tilde{C}$. Fig. 3.6 shows the Hermite-Gaussian branches in the total intensity I_{ges}. The saddle-node bifurcations of the branches happen at very low intensities around $I_{ges} \approx 0.2$ compared to the intensity values of the high-intensity branches. Since the mode width grows with the mode number (see the theory part), the high-intensity branches average slope increases with the mode number. This representation of the modes in I_{ges} also explains, why the representation in ω is prefered.

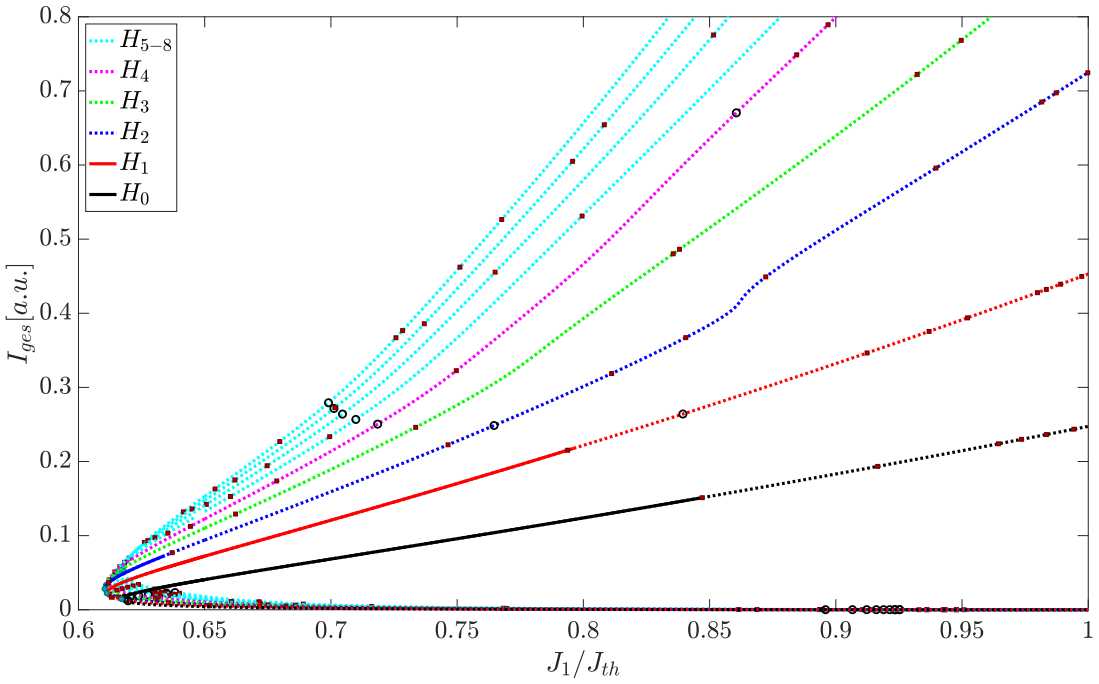

Figure 3.6: The total intensity I_{ges} of the first 9 Hermite-Gaussian branches H_0-H_8 as a function of j_1/J_{th}. The representation is equal to those in Fig. 3.5.

The intensity profiles corresponding to the first nine Hermite-Gaussian modes for J_1/J_{th} = 0.65 are presented in Fig. 3.7. The panels show the intensity distribution (red) compared to the analytically calculated one (blue). Obviously the intensity distribution of the n-th mode exhibits n+1 intensity maxima and its corresponding panel is marked with I_n. The analytic Hermite-Gaussian modes are calculated for zero diffusion ($d = 0$) and for vanishingly small intensity (see equation (2.30)).
For the fundamental mode H_0 the difference between analytical intensity and the intensity profile generated by PDE2PATH is considerable. The maximum amplitude of the modes is pretty constant and just increases slightly and monotonous with increasing mode width. The textitfull width half maximum (FWHM) of the analytical mode is much smaller than the numerical one, while the accordance of the higher modes is performing much better. This can be explained by the fact, that unlike the higher order modes, the fundamental mode is just a Gaussian pulse and can exist in a dispersive and nonlinear medium, i.e. it can also be stable for C=0. The dispersive soliton in Fig. 3.7 (a) is not exactly the fundamental Gaussian mode, predicted in equation (2.34), since the influence of the diffusion d and the deviation from the approximation of vanishing intensity seems to have more influence on the shape of the pulse, than the potential C or

the magnitude of the diffraction B. Generally the accordance with the analytical profiles grows with the mode number. The reason for this behavior is probably that the wider modes experience a relatively higher potential, which means that the aforementioned simplifications are more valid.

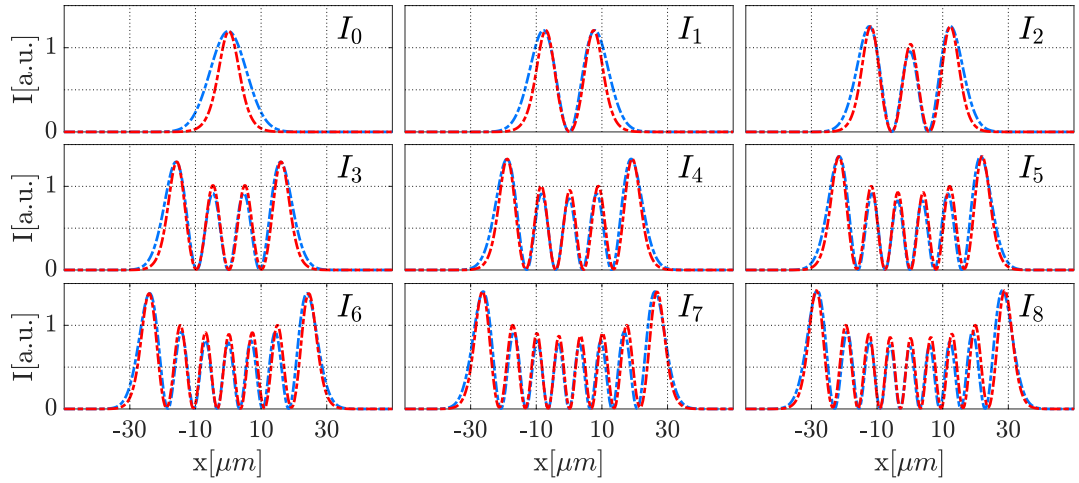

Figure 3.7: Intensity profiles I_n of the first 9 hermite gauss modes (red) and the analytically calculated intensity profiles (blue). The maximum intensity of the analytical intensity profiles is normed to the maximum intensity calculated by PDE2PATH. Parameters are: $J_1/J_{th} = 0.65$, $\tilde{B} = 0.2914$ and $\tilde{C} = -7.7{\cdot}10^{-5}$; ($C = -5 \cdot 10^{-5}$ and $B = -18$).

The ω-spacing $\Delta\omega$ between the different modes is related to the fold points at the end of the high-intensity branches for the maximum value of J_1/J_{th}. This is the point of vanishing intensity, where the accordance of the analytical mode with the result of the continuation should be almost perfect. The analytical value for the ω-spacing between two adjacent hermite gauss modes is $\Delta\omega = 0.0095$. The analytical and numerical values of $\Delta\omega$ are in good accordance with each other, though the analytical values are calculated for $d = 0$. The exact omega spacing $\Delta\omega_n = \omega_n - \omega_{n-1}$ between the modes is: $\Delta\omega_1 = \omega_{H_1} - \omega_{H_0} = 0.0096$, $\Delta\omega_2 = 0.0097$, $\Delta\omega_3 = 0.0096$, $\Delta\omega_4 = 0.0097$', $\Delta\omega_5 = 0.0096$, $\Delta\omega_6 = 0.0097$, $\Delta\omega_7 = 0.0097$, $\Delta\omega_8 = 0.0097$, $\Delta\omega_9 = 0.0096$.
Besides the intensity profiles for the high-intensity branch also the intensity profiles of the low-intensity branch - which is always unstable - are investigated. Figure 3.8 shows the intensity profiles of the unstable low-intensity branch for the same parameters as in Fig. 3.7. As in Fig. 3.7 the analytical intensity profiles are normed to the numerically calculated ones. Interestingly the behavior of the accordance is the exact opposite compared to the high-intensity branch. While the agreement of the H_0 mode is very good, the mismatch increases with mode-number, in the way that the amplitude in the mode center shrinks. Also the kind of mismatch is very different. The intensity profiles of the high-intensity branch for H_0, H_1 and also H_2 are sqeezed spatially, compared to the analytical ones. The intensity profiles on the low-intensity branch doesn't exhibit this spatial pinch. They are damped in amplitude in the mode center compared to the analytical solution (see Fig. 3.8). This damping effect increases with the mode number and is well over 50% for the H_8 mode. The amplitude of the H_6-mode is the biggest, while the fundamental mode got the smallest intensity.

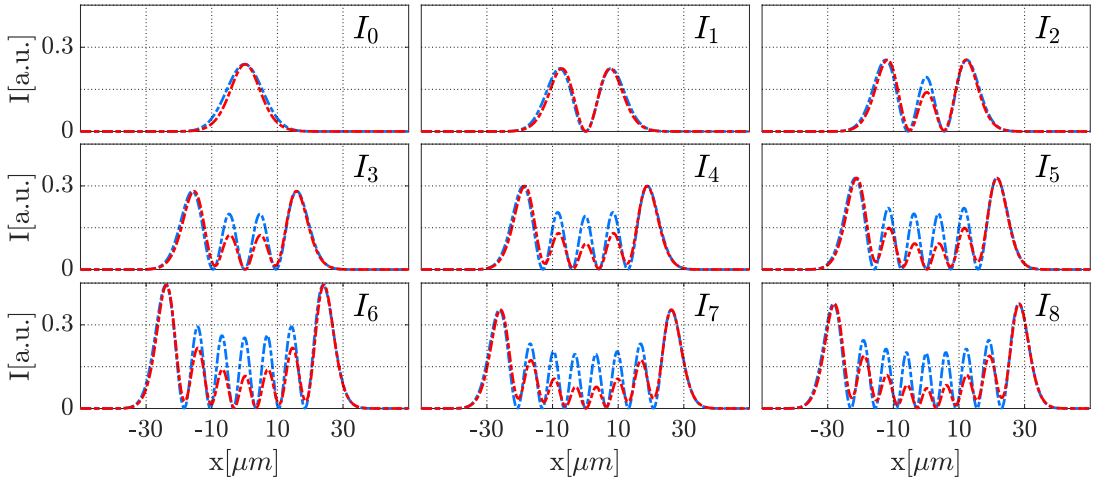

Figure 3.8: Intensity profiles I_n of the first 9 Hermite Gaussian modes for the (unstable) low-intensity branch (red) and the analytically calculated intensity profiles (blue) for the standard value of the gain $J_1/J_{th} = 0.65$, $\tilde{B} = 0.2914$ and $\tilde{C} = -7.7 \cdot 10^{-5}$.

In Fig. 3.9 the potential C is increased to $\tilde{C} = -1.55 \cdot 10^{-3}$. As expected, the agreement of the lower order modes gets better and is almost perfect. Also the mode shrinks together spatially as well as in amplitude. The shrinking in amplitude is caused by the relation between the potential $\tilde{C}$ and the mode width σ ($\sigma^2 = \sqrt{-\tilde{B}/\tilde{C}}$) deduced in the theory part. The reduced amplitude can be explained by the available part of the gain section. The amplitude of the fundamental mode differs from the other modes and is considerably higher than the amplitude of the fundamental mode for $\tilde{C} = -7.7 \cdot 10^{-5}$ (see Fig. 3.7). The amplitude decreases with increasing mode number and the amplitude of the H_8-mode is approximately 50 % of H_0. This behavior is contrary to the one for $\tilde{C} = -7.7 \cdot 10^{-5}$.

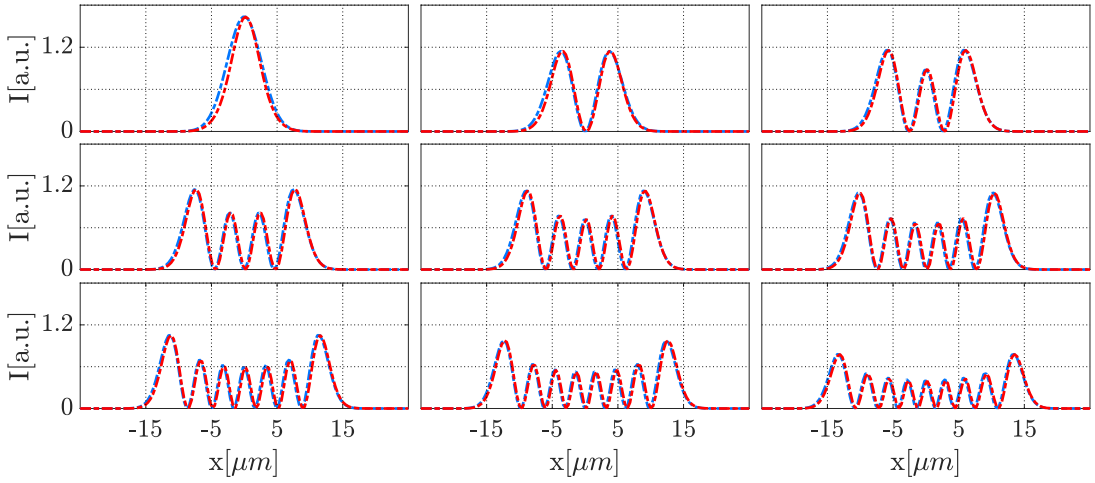

Figure 3.9: Intensity profiles of the first 9 hermite gauss modes (red) and the analytically calculated intensity profiles (blue) for the standard value of the gain J_1/J_{th} = 0.65 and $\tilde{C} = -1.55 \cdot 10^{-3}/C = -1 \cdot 10^{-3}$. The maximum intensity of the analytical intensity profiles is normed to the maximum intensity calculated by PDE2PATH.

3.2.1 Branch Points and bifurcating Branches

The branches of all modes except the H_0 mode contain branch-points, in the following the branch points and bifurcating branches of the H_1 and H_2 mode are investigated. Both branches contain three branch points, two of them on the low-intensity part of the branch and one on the high-intensity part. Figure 3.10 shows the (J_1/J_{th}, I_{max}) diagram of the H_0 branch (black) with bifurcating branches (grey). The branch points bp_2 and bp_1 are located on the unstable part of the branch near to the stability-limiting bifurcations (fold bifurcation F (cyan dot) at $J_1/J_{th} \approx 0.611$ and the Hopf bifurcation H (red dot)) at $J_1/J_{th} \approx 0.798$. Another branch point bp_3 is located on the low -intensity part of the branch at around $J_1/J_{th} \approx 0.9$ and is connected to the branch point bp_2 next to the fold point F. The bifurcating branch on the high-intensity part of the H_1-branch goes backwards in intensity and ω, up to a fold bifurcation labeled as point 4 (green dot). All solutions one this branch are unstable. The solution at this fold point has an asymmetric intensity profile and is shifted to the right side of the cavity (see panel (e)). The right peak of the intensity is higher than the left one. From the fold point 4 the branch goes to higher intensities, running pretty parallel to the H_1-branch. The mode at point 5 (orange dot) on this branch (upper right corner in Fig. 3.10 (a)) is shifted further to the right side of the cavity while the difference between the right and the left intensity peak grows (see panel (f)). Also the maximum intensity is more than doubled compared to point 4, caused by the higher gain value near to the threshold. All solutions on this bifurcating branch show the characteristic that the modes are shifted to the right side of the cavity, while the right peak gets bigger compared to the left one.

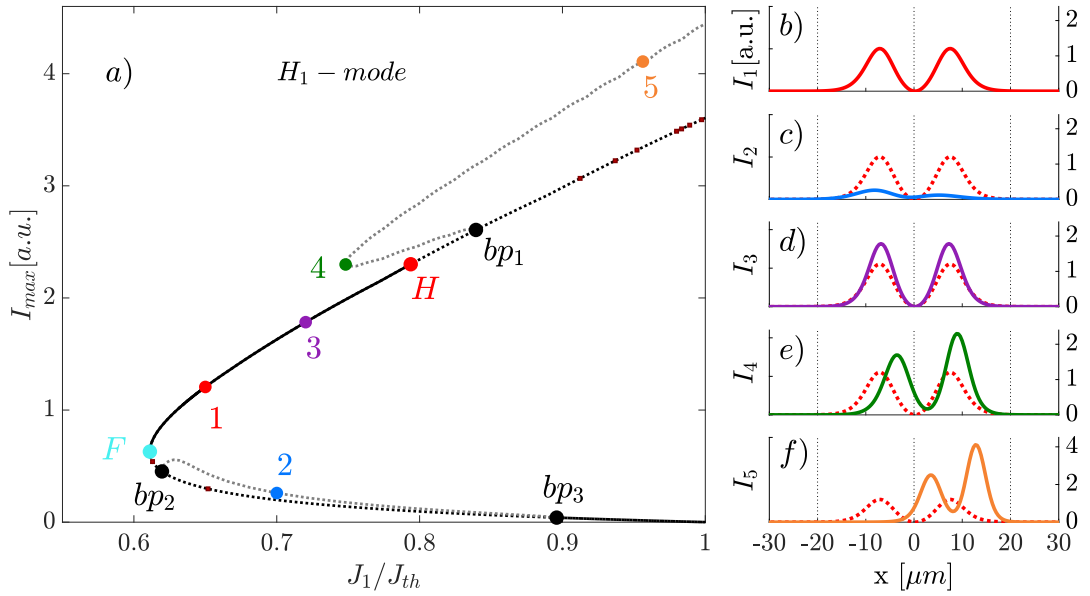

Figure 3.10: (a) H_1 branch (j_1/j_{th}, I_{max}) with branch points bp (black dots) and bifurcating branches (grey). Fold and Hopf bifurcations are marked with cyan and red dots. The intensity profiles shown on the right correspond to the coloured and numbered dots (b-f). The intensity profile of point 1 in the stable regime of the H_1-branch is plotted in every panel b)-f) to have a better comparison.

For the low-intensity branch connecting bp_2 and bp_3 the contrary is the case. The modes

are shifted to the left side of the cavity and the left peak grows compared to the right. Panel (c) shows the intensity profile of point 2 (blue) at $J_1/J_{th} \approx 0.9$ on this branch, compared to the intensity profile of point 1 (dotted red line). The intensity of the solutions on this branch is very low and the whole branch is unstable.
The branch points and the bifurcating branches of the H_2-mode are illustrated in Fig. 3.11. The shapes of the branches look generally pretty similar to the ones for the H_1-mode. The stability range of the H_2-mode is a lot smaller than that of the H_1-mode and is limited by two Hopf points H_1 and H_2 (red dots). As in Fig. 3.10, the fold point on the branch bifurcating from branch point bp_1 is labeled 4 (green) with the corresponding intensity profile in panel (e). The mode is shifted towards the right side of the cavity, the intensity of the three peaks decreases from right to left.

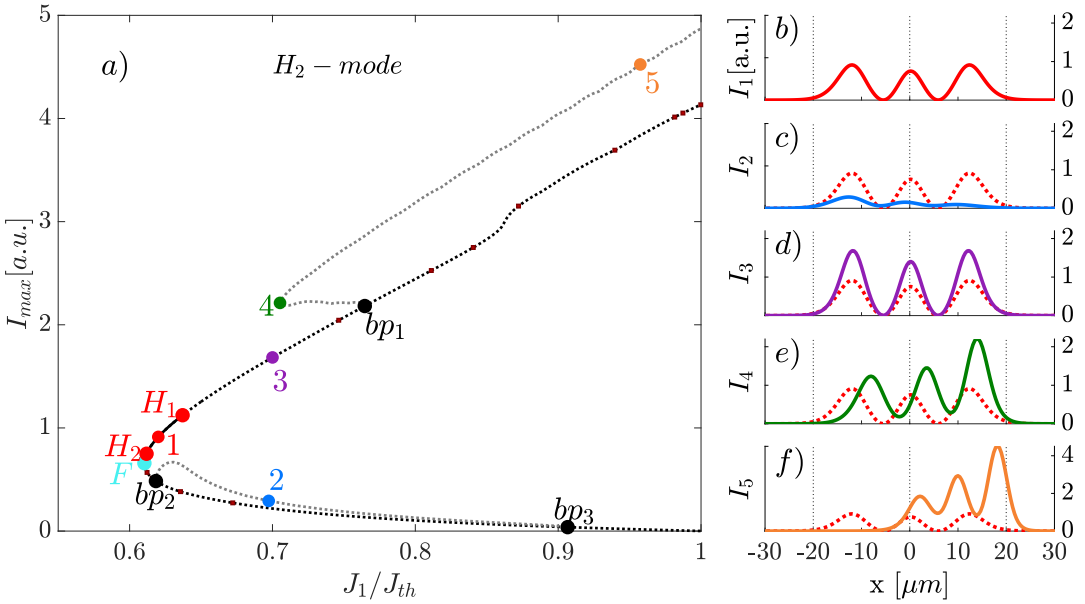

Figure 3.11: H_2 branch (j_1/j_{th}, I_{max}) with branch points (black dots) and bifurcating branches (grey) (a). The intensity profiles shown on the right (b-f) correspond to the coloured and numbered dots.

This behavior is basically the same, like for the H_1-branch in Fig. 3.10. Point 5, which is on the same branch for $J_1/J_{th} \approx 0.95$ shows the same behavior potentiated, meaning that the mode is shifted further to the right side of the cavity and the decrease from the right to the left peak is bigger. Also the mode is squeezed in width, compared to the mode profiles at the points 1 or 3 on the H_2 branch or at the fold point (point 4). The intensity profile at point 2 on the low-intensity part of the H_2-branch exhibits also the same characteristics like the profile of point 2 in Fig. 3.10. It's slightly shifted to the left and the peak height decreases from left to right. The maximum intensity is pretty low compared to the other intensity profiles (the unit of the maximum intensity is arbitrary). The fact that the branch points are located outside the stabile range of the branches seems to be true for all values of $\tilde{C}$. This can be assumed later from Fig. 3.19 where the branches H_0-H_8 are illustrated for different values of $\tilde{C}$. As the stability range of the branches increases, the branch points are shifted to higher gain values, i.e. away from the stable part of the branch.

3.2.2 Critical Eigenfunctions

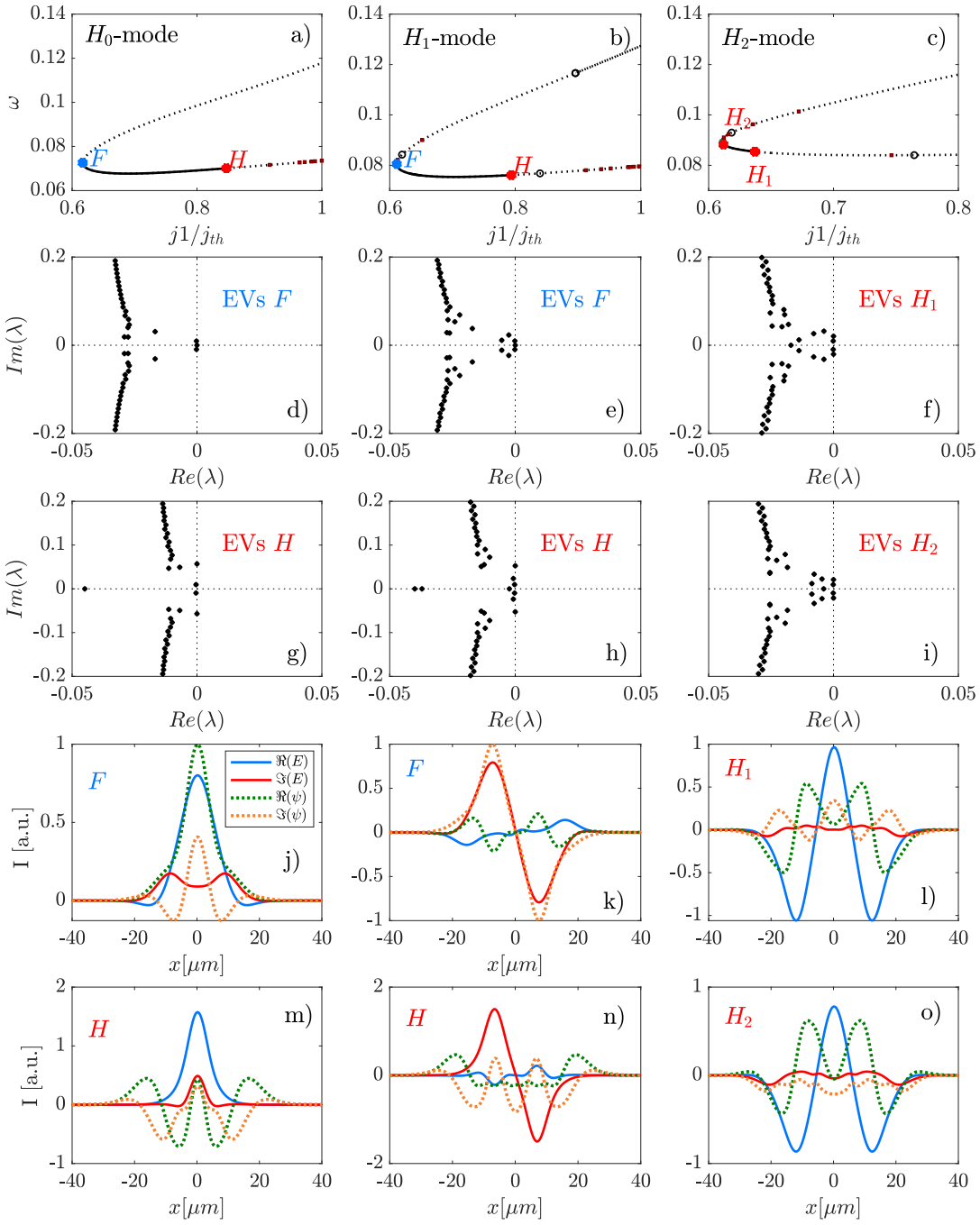

Figure 3.12: **row 1**: $(j_1/j_{th}, \alpha)$ plane of H_0, H_1 and H_2 modes. The bifurcation points limiting the range of stability are coloured and denoted with F (fold) or H (Hopf). One column corresponds to one mode.
row 2-3: Eigenvalue spectrum related to the stability-range-limiting bifurcation points, also marked with F (fold) or H (Hopf). The eigenvalues imaginary part $Im(\lambda)$ is plotted against the real part $Re(\lambda)$.
row 4-5: Critical eigenfunctions and intensities at the fold and Hopf points. Intensity of the mode (black), real part $\Re$ (green) and the imaginary part $\Im$ (orange) of the critical eigenfunction.

The next step is to investigate the critical eigenfunctions of the higher order Hermite-Gaussian modes, to see how the different modes lose their stability. Another important point is to compare the critical eigenfunctions of the Hermite-Gaussian modes fold points (which limit the unstable low-intensity branches for vanishing intensity) with the critical eigenfunctions of the first bifurcation points of the off-solution.
Figure 3.12 shows the bifurcation diagrams (a-c), eigenvalue spectra (d-i) and critical eigenfunctions (h-o) of the first 3 modes. The spectra of eigenvalues for all 3 modes have a basically similiar structure on the macro-scale, consisting of an approximately vertical line of eigenvalues, which is "pulled" to the origin for small imaginary parts $|Im(\lambda)| < 0.1$. A vertical line would correspond to a conservative system, the dissipative terms in equation (2.26) cause the modified form of the spectra of eigenvalues. The complexity of the spectrum of eigenvalues increases with the mode number.

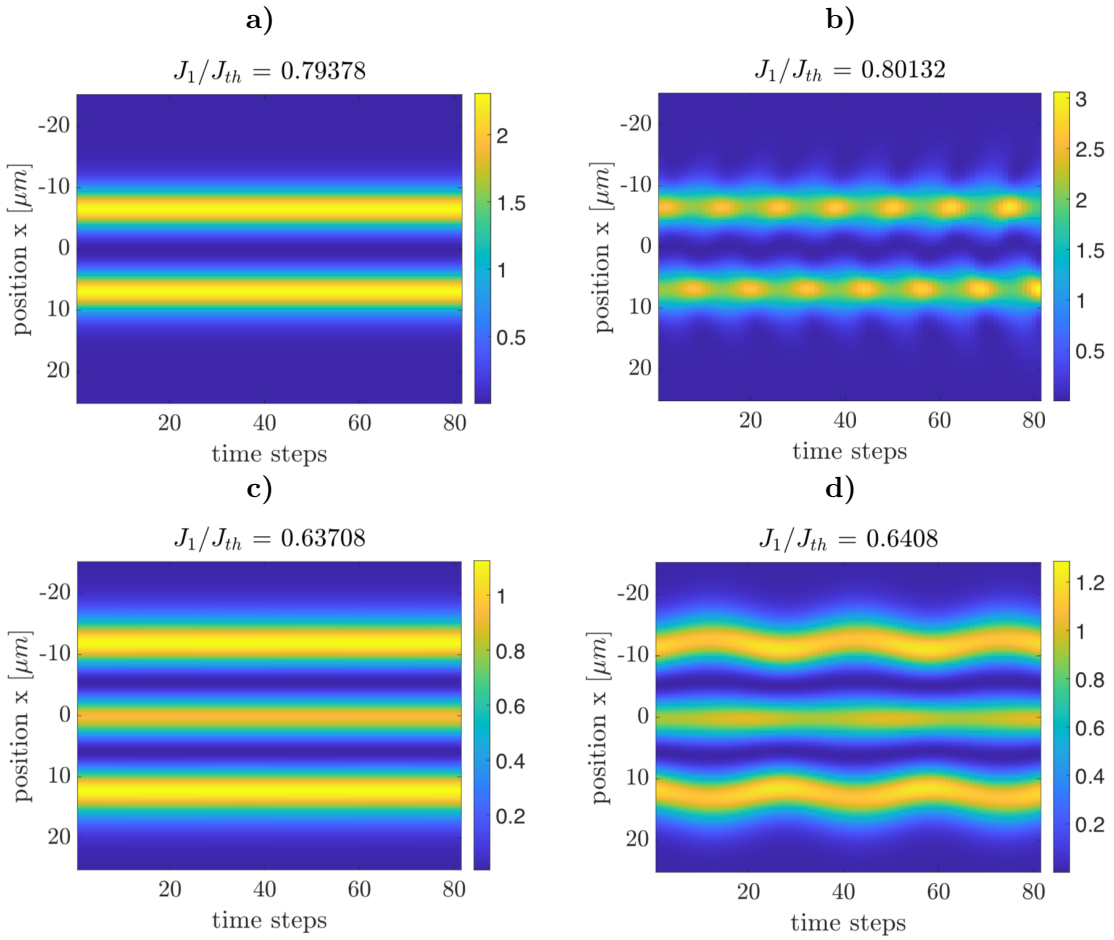

Figure 3.13: Temporal dynamics of the intensity profiles from unstable sections of the H_1-branch (a,b) and H_2-branch (c,d).The y-axis visualizes the inner 25% (50 μm) of the cavity, x-axis shows the number of steps in the DNS. a) and c) show the behavior at the Hopf points limiting the stability range. b) and d) show the spatio temporal dynamics for increased gain.

The symmetrical shape of the critical eigenfunction of the H_0 mode in Fig. 3.12 (m) was already illustrated in Fig. 3.2. The critical eigenfunction at the Hopf point - limiting the stability range of the H_1-mode - (Fig. 3.12 (n)) is also symmetric while the field of the mode is antisymmetric. The symmetric perturbation of the antisymmetric electric

field of the mode results in asymmetric oscillations of the mode. Fig. 3.13 (a) illustrates a direct numerical simulation of the spatio-temporal dynamics of the H_1-mode at the Hopf point ($J_1/J_{th} \approx 0.794$), where the mode is still completely stable. In Fig. 3.13 (b) the mode is shown for a slightly increased gain of $J_1/J_{th} \approx 0.801$. The mode starts to breathe asymmetrically. One of the two peaks of the H_1-mode reaches the maximum intensity while the other one is reaching the minimal intensity. This antisymetric in agreement with the aforementioned critical eigenfunction and it's influence on the modes electric field. The critical eigenfunction at the Hopf point H_1 (red) of the H_2-mode is symmetric (panel (o)). This symmetric pertrubation on the symmetric H_2 mode results in a symmetric oscillation of the mode. Fig. 3.13 (b) and (d) show the spatiotemporal dynamics of the H_2 mode at the Hopf point ($J_1/J_{th} \approx 0.637$) as well as for an increased gain of $J_1/J_{th} \approx 0.641$. The symmetric breathing of the intensity profile is fundamentally different to the lower modes. The intensity of the two outer peaks stays pretty constant. Just the intensity of the weaker, inner peak is oscillating significantly.

3.2.3 Off-Solution and Hermite-Gaussian Branches

The regime of Hermite-Gaussian modes is a regime of bistability with the off-solution, since it's below the lasing threshold J_{th}. The low intensity branch of the Hermite-Gaussian branches plays the role of a seperatrix between the high intensity solution and the off-solution. When following the low-intensity branch towards higher gain values, the intensity is reduced to arbitrary low values and the branches can be continued to $J_1/J_{th} > 1.0$. Between $J_1/J_{th} = 1.0$ and $J_1/J_{th} = 1.008$ the branches of the first nine Hermite-Gaussian branches turn around in a fold bifurcation, which is illustrated in the right part of Fig. 3.14. The intensity of the modes at the fold points for the used step size is neglectable ($\approx 10^{-18}$). In ω the branches are equidistantly spaced on a nearly perfect line.

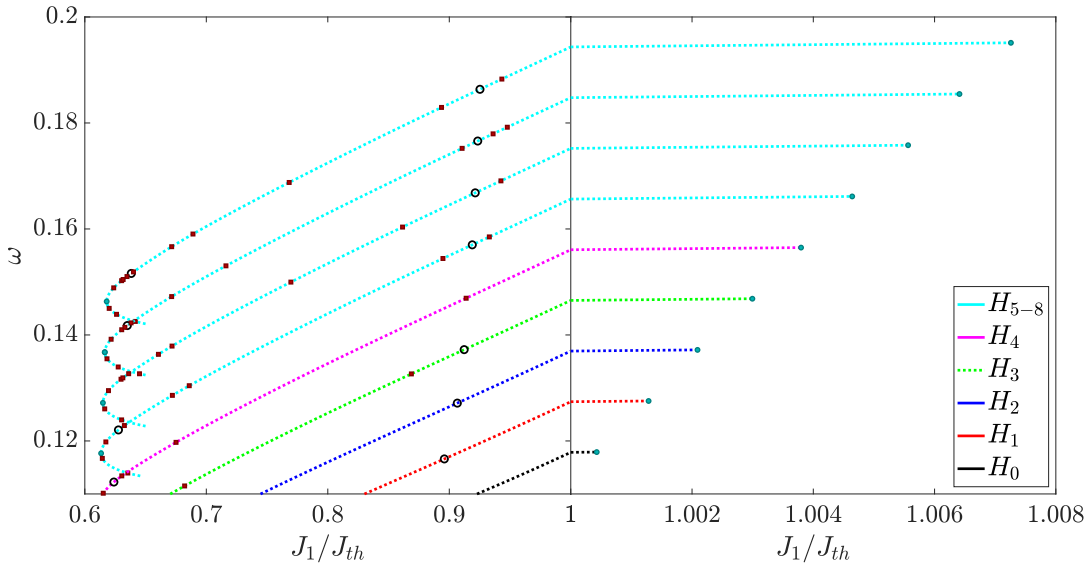

Figure 3.14: Bifurcation diagram of the first nine low-intensity branches of the Hermite Gaussian modes in ω as a function of the normalized gain value J_1/J_{th}. The left part illustrates the branches over the widest range of their existence, the right part zooms in a very small gain interval just above the threshold gain where the branches turn around in a fold bifurcation.

Especially the branching behavior of the off-solution is of paramount importance. The continuation of the off-solution revealed, that the first Hopf points beyond the threshold gain J_{th}, emerge at the same gain values where the Hermite-Gaussian modes fold points are located which limit the unstable low-intensity branches for vanishing intensity. This is illustrated in Fig. 3.15 (a), where the thin vertical black lines represent the gain values of the first Hopf bifurcations of the of solution, which perfectly match the fold points limiting the low-intensity branches (coloured dots). The colour scheme is the same like in the previous plots (H_0 black, H_1 red, H_2 blue, H_3 green, H_4 magenta, H_5 cyan). Fig. 3.15 (b-g) show the real part of the critical eigenfunctions of the off-solutions Hopf points (orange) as well as the real part of the critical eigenfunctions of the branches fold points (coloured) and the imaginary parts of both eigenfunctions (dark green). The arbitrary phase is choosen to be zero in the modes center, so that the imaginary part is zero. Since Hermite Gaussian modes exhibit a constant phase the imaginary part stays very

small over the spatial extension of the modes. In panels (h-m) the corresponding spectra of eigenvalues are compared. As expected the eigenvalues of the HG-modes (coloured) cross the imaginary axis in the origin while the off-solutions eigenvalues (orange) cross the imaginary axis as a pair of complex conjugate eigenvalues.

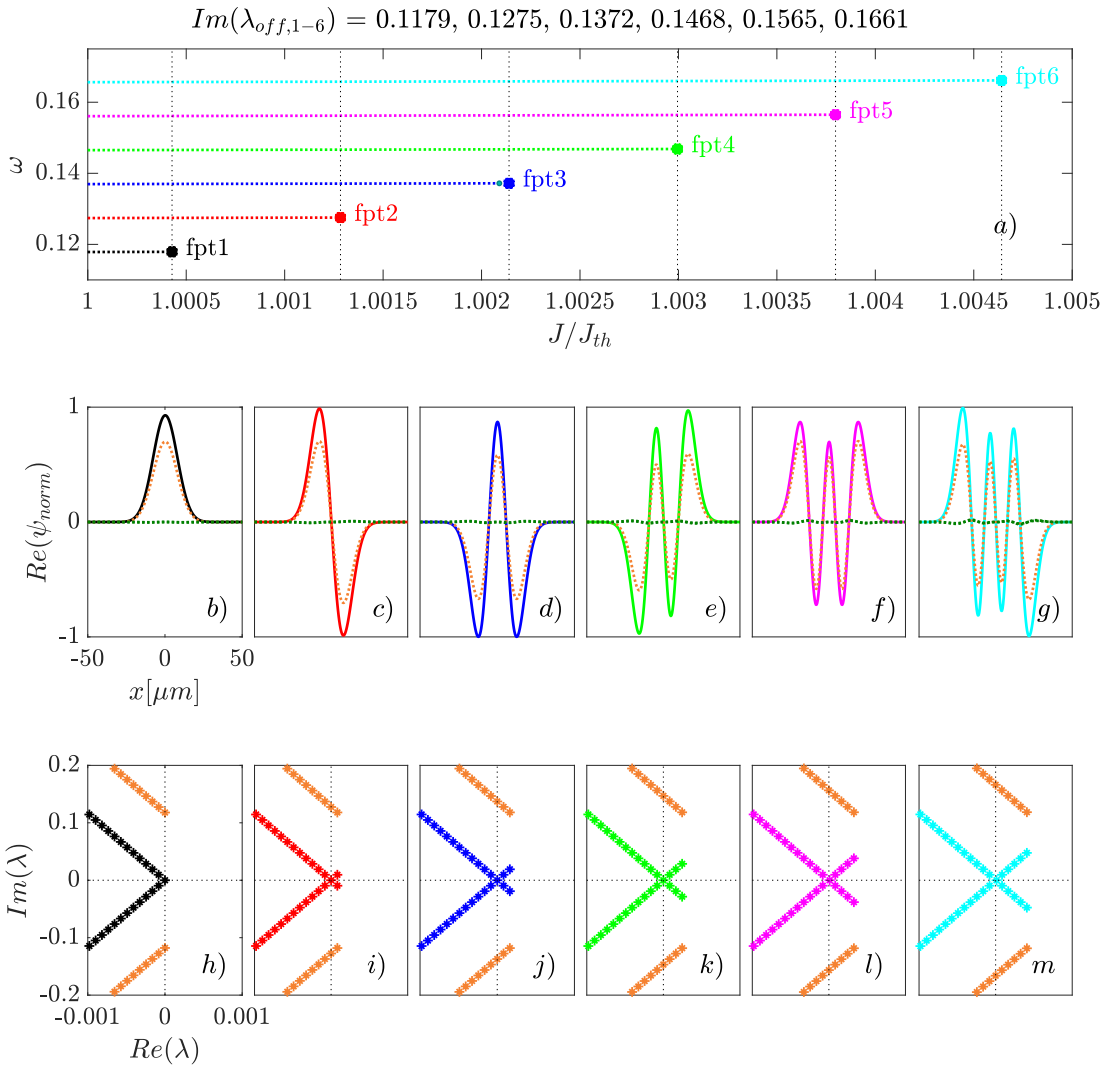

Figure 3.15: (a) The branches of the first six Hermite-Gaussian branches (coloured, same colour scheme like in the previous figures), which are limited by the fold points fpt1 to fpt6. The positions of the first six Hopf points of the off-solution above threshold are marked with thin vertical black lines. (b-g) L2-norm of the real-parts of the Hermite Gaussian modes H_0 to H_5 (solid coloured lines) and the real-part of the critical eigenfunctions at the off-solutions Hopf points for the same gain-values (dotted orange lines), phase is set to zero in the center of the cavity. (h-m) eigenvalue spectra of the off-solutions Hopf points (orange) and the hermite gauss modes fold points (coloured). The imaginary parts of the eigenvalues of the critical eigenfunctions of the off-solution are $Im(\lambda_{off,1-6}) = 0.1179, 0.1275, 0.1372, 0.1468, 0.1565, 0.1661$. They correspond to the values of ω corresponding to the fold points in panel a).

The absolute values of these complex conjugate eigenvalues imaginary parts are equivalent to the ω-values of the Hermite-Gaussian modes branch-limiting fold points. This is evident, because the perturbation of the critical eigenfunction at the off-solutions Hopf points have the form of a factor $e^{i \cdot Im(\lambda) \cdot t}$. This ist the same form, like the phase-factor $e^{i\omega t}$. Other than the Hermite-Gaussian modes the off-solution doesn't reveal a phase, i.e. $\omega = 0$. Due to this a branching from the off-solution to the Hermite-Gaussian branches is not trivial. However the connection between the first Hopf points of the off-solution above threshold and the fold points limiting the Hermite-Gaussian branches towards zero intensity is proven by the accordance of the critical eigenfunctions as well as the precisely matching values of J_1/J_{th} and ω / $Im(\lambda_{off})$.

3.3 The Influence of the System Parameters

Up to this point, only the influence of changes in the gain value j_1 on the Hermite-Gaussian modes were investigated. In the following, the influence of the variation of other system parameters is mainly investigated by numerical continuation. These most important parameters are the diffraction B and the potential C, which specify the imaging behavior of the optical characteristics of the laser cavity, first-order approximated by an $ABCD$-matrix. The values of these parameters can be changed by the variation of the distance d_1 (between the MIXSEL and the lens) and the distance d_2 (between the lens and the mirror) (see Fig. 2.2). Small variations of d_1 change just B while small variations of d_2 changes B as well as C (see theory part). The parameters appearing in Eq. (2.26) are $\tilde{C}$ and $\tilde{B}$ - instead of C and B. That's why the parameter studies are performed in $\tilde{C}$ and $\tilde{B}$. The effective potential $\tilde{C}$ is proportional to C, because the the potential is completely caused by the deviation from perfect self-imaging. The effective diffraction $\tilde{B}$ however is not proportional to B. This is because also for perfect self-imaging the system includes diffraction. The parameter B of the transformation matrix just modifies the field diffraction. B=0 corresponds to $\tilde{B}$=1. Besides $\tilde{B}$ and $\tilde{C}$, the influence of changes in the diffusion parameter d and the introduction of a nonuniform gain profile are considered.

3.3.1 Continuation in $\tilde{C}$

First, the parameter $\tilde{C}$ which considers the first order influence of wavefront curvature on the light propagation is investigated. The standard value used is $\tilde{C} = -7.7 \cdot 10^{-5}$. The continuation of the Hermite-Gaussian modes in ω with respect to $\tilde{C}$, is visualized in Fig. 3.16. The total range of existence of the $H_0 - H_8$-branches is shown in panel (a). The H_0 branch (black) exhibits by far the biggest range of existence and stability. It is stable from $\tilde{C} = 0$ to $\tilde{C} \approx -0.47$ where it turns around in a fold bifurcation. As H_0, all other modes turn around in fold bifurcations as well. Though only the fundamental mode stays stable until this fold bifurcation. All other modes lose their stability in Hopf bifurcations, which can be seen for H_1 and H_2 in panel (b). The more detailed view in Fig. 3.16 (c) around $\tilde{C} \approx -4 \cdot 10^{-4}$ shows the range where the branches lose their stability. This change in stability is caused by a Hopf bifurcation, which shifts to higher $\tilde{C}$-values for $H_0 - H_6$. For $\tilde{C} \to 0$, the H_6 mode loses the stability first (at $\tilde{C} \approx 2.9 \cdot 10^{-4}$). For the higher modes H_7 and H_8, the stability-limiting Hopf bifurcations are again shifted towards zero. Fig. 3.16 (d) reveals, that most branches got very small stable ranges around $\tilde{C} \approx -2 \cdot 10^{-7}$. Besides the fundamental mode, which is getting unstable for $\tilde{C} < 0$, just the H_1 mode is not getting stable again. However the H_1 mode is stable until $\tilde{C} \approx -1 \cdot 10^{-6}$, which is not the case for the higher modes (see panel (c)). These stable ranges of the modes $H_2 - H_6$ are limited by two Hopf points. All branches can be continued above $C = 0$. The branch of the modes H_2 and H_4 for example go back and forth over $C = 0$. Most remarkable is, that for the H_2 mode (blue) two stable ranges exist for $C \approx -1 \cdot 10^{-7}$. This regime of bistability of the H_2 mode is further treated in Fig. 3.17. Panel (a) basically repeats panel (d) from Fig. 3.16. P_1 and P_2 (blue dots) indicate the positions on the branch, where the solutions of the panels (c) and (d) are located. The value of $\tilde{C}$ for both points is $\tilde{C} \approx -1.54 \cdot 10^{-7}$. Panel (c) shows the H_2 mode for the standard parameter values.

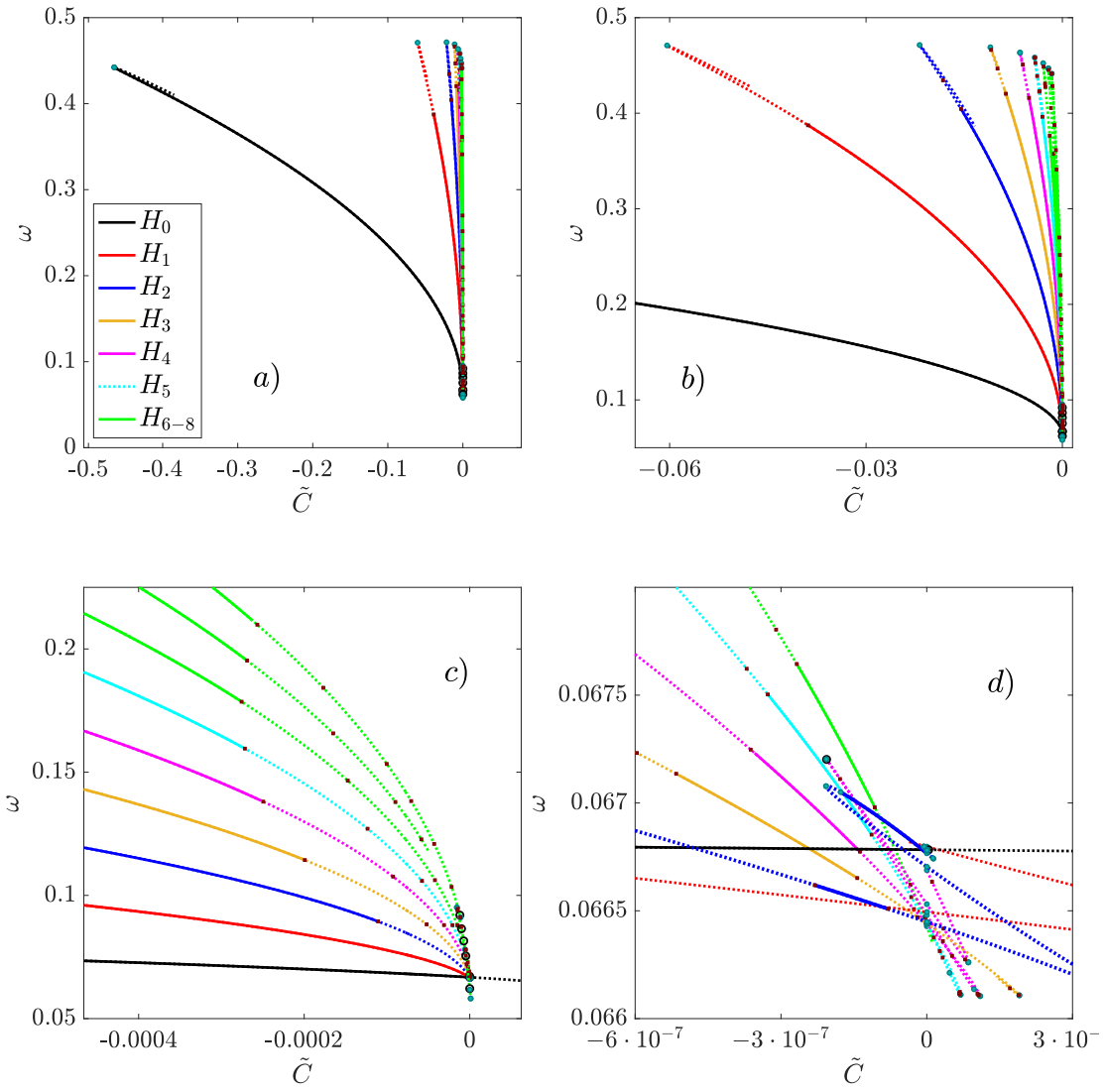

Figure 3.16: Bifurcation diagrams of ω with respect to C for the first 9 Hermite-Gaussian modes. The different panels show different scales. The colour-scheme of the branches is the same for all panels. Hopf bifurcations are marked by red squares, fold bifurcations by green dots. Stable parts of the branches are represented by solid lines, unstable parts by dotted lines.

While the maximum intensity of the three solutions is approximately the same, the distance between these peaks - i.e. the mode width - differs significantly. The width of the H_2 mode for the standard parameter values is $\approx 35\mu m$, for the solution at point P_1 it's $\approx 60\mu m$ and for the solution at point P_2 it's $\approx 80\mu m$. The phase of a Hermite Gaussian mode is constant, which is the case for the solution for the standard parameters (panel (b)) and the solution for point P_1, where the phase is jumping between 0 and $\pm\pi$ in the area of the mode. In contrast the solution for P_2 consists of three solitary peaks, with a totally different phase-behavior. For a Hermite-Gaussian mode, the real and/or the imaginary part is oscillating strongly, like the imaginary part of the solutions in panels (b) and (c). For the solution in panel (d) both the real and the imaginary part got a negative amplitude, indicating that this solution is something different than a Hermite-Gaussian mode. This solution is probably one of a few stable solutions with

three solitary pulses inside the cavity. The stability of both solutions in Fig. 3.17 (c) and (d) is confirmed via DNSs.

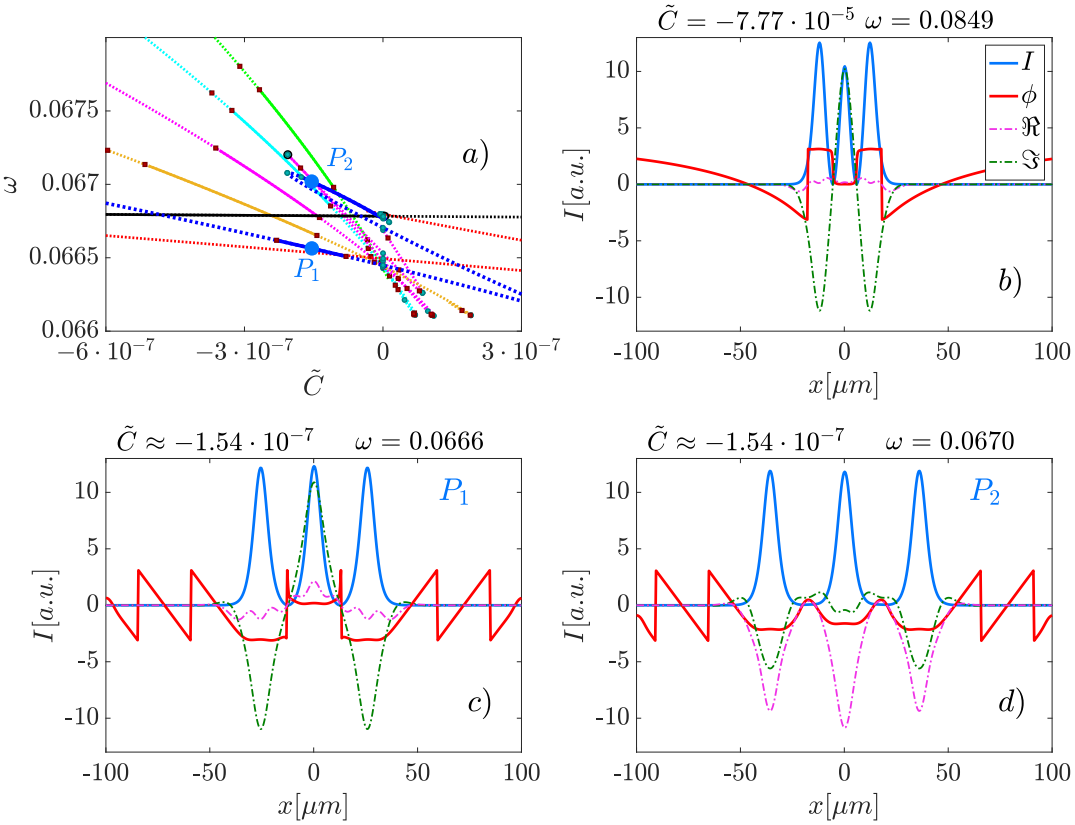

Figure 3.17: (a) Bifurcation diagram of the branches H_0 to H_6 in ω with respect to $\tilde{C}$ close to $\tilde{C} = 0$. The diagram is basically the same like in Fig. 3.16 (d) including the colour-scheme. Hopf bifurcations are marked by red squares, fold bifurcations by green dots. Stable parts of the branches are represented by solid lines, unstable parts by dotted lines. The blue dots in a) mark two different solutions for $C \approx -9.92 \cdot 10^{-8}$. The corresponding intensity profiles I (blue), phases ϕ (red), real parts $\Re$ (orange) and imaginary parts $\Im$ (green) are displayed in (c) and (d). Panel (b) shows the H_2 mode for the standard parameter values, i.e. $\tilde{C} = -7.7 \cdot 10^{-5}$.

Next, the influence changes $\tilde{C}$ one the H_2 mode is studied. The H_2-mode is chosen because it's complex enough to really be a Hermite-Gaussian mode while the computational effort is less than for the higher order modes. The comparison with the analytical mode profiles revealed that - for the standard parameter values - the modes H_0 and H_1 show much more deviation than H_2 (see Fig. 3.7). Also the stability range is significantly smaller than that for H_0 or H_1, so that changes in the stability are potentially better observable. The influence of the value of $\tilde{C}$ on the branch form and stability range with respect to J_1/J_{th} is exemplarily shown in Fig. 3.18 (a). For higher values of $\tilde{C}$, the H_2-branch shifts to higher values of ω, while the range of stability increases significantly. for $\tilde{C} = -3.11 \cdot 10^{-5}$ (grey) the branch contains no stable solutions. For this value the branch also develops a kink at $J_1/J_{th} \approx 0.77$. Here two fold bifurcations induce a change in direction, i.e. the branch is - for a small distance - going backwards. When C increases,

this kink is shifted to higher values of J_1/J_{th} and smoothed. For the standard parameter value $\tilde{C} = -7.7 \cdot 10^{-5}$ (black branch) it's still appearing as a hump at $J_1/J_{th} \approx 0.86$. The branch for $\tilde{C} = -7.7 \cdot 10^{-5}$ shows a stability range of $\Delta J_1/J_{th} \approx 0.025$, limited by two Hopf points. This stability range doubles to $\Delta J_1/J_{th} \approx 0.05$ for $\tilde{C} = -1.55 \cdot 10^{-5}$ (red branch) and shifts to the fold bifurcation - showing the typical bifurcation behavior of Hermite Gaussian modes. The stability range for higher values of $\tilde{C}$ is also limited by a fold and a Hopf bifurcation. It increases to $\Delta J_1/J_{th} \approx 0.1$ for $\tilde{C} = -1.55 \cdot 10^{-3}$. The modes maximum intensity increases slightly with the value of $\tilde{C}$. For the biggest values of ($\tilde{C} = -1.55 \cdot 10^{-3}$) the modes FWHM gets reduced by approximately 100% compared to $\tilde{C} = -7.7 \cdot 10^{-5}$, shrinking from FWHM $\approx 32\mu$m to FWHM $\approx 16\mu$m.

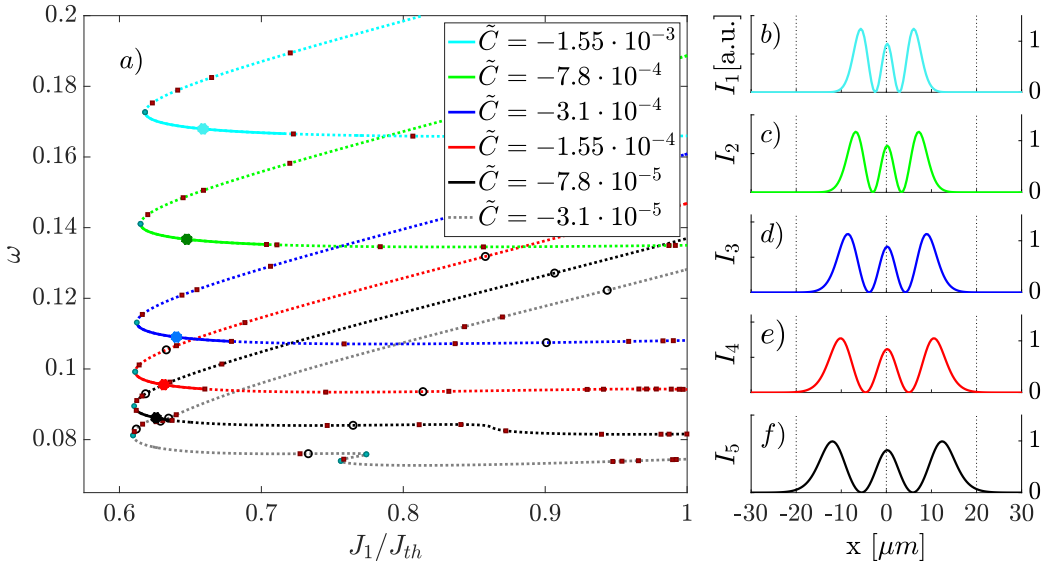

Figure 3.18: (a) Bifurcation diagram of the H_2 mode fin ω with respect to J_1/J_{th} for different values of $\tilde{C}$. For clearity reasons, just the high-intensity branch is plotted. Hopf bifurcations are marked by red squares, fold bifurcations by green dots. Stable parts of the branches are represented by solid lines, unstable parts by dotted lines. b)-f) show the intensity profiles of the stable solutions marked by the coloured dots in panel (a).

To give a general idea about the fundamental dependence of the Hermite-Gaussian modes on $\tilde{C}$ Fig. 3.19 shows the first 9 Hermite-Gaussian modes for three different values of $\tilde{C}$. For $\tilde{C} = -7.7 \cdot 10^{-5}$ (panels (a) and (b)) the H_0 mode is stable from $J_1/J_{th} \approx 0.615 - 0.847$, H_1 from $J_1/J_{th} \approx 0.604 - 0.798$ and H_2 from $J_1/J_{th} \approx 0.605 - 0.634$. The H_3 mode is always unstable and the stability ranges of H_4 - H_8 are very small. The stability range of the modes grow from H_4 to the higher modes. This is expectable because for growing mode width the mode experiences more influence of the parabolic potential. However, this idea is just appropriate for small enough values of $\tilde{C}$ and it doesn't hold true for $\tilde{C} \geq -1.55 \cdot 10^{-4}$.
For $\tilde{C} = -1.55 \cdot 10^{-4}$ (panels (c) and (d)), the stability ranges of the higher order Hermite-Gaussian modes increase significantly (Fig. 3.19 (c)). The stability range of H_8 increases by a factor 5 compared to $\tilde{C} = -7.7 \cdot 10^{-5}$. The stability ranges of all modes are now limited by a fold and a Hopf bifurcation. Also the H_3 mode becomes stable. The size of the stability range now decreases with increasing mode number. Just the range

of stability of the fundamental mode is slightly reduced compared to $\tilde{C} = -7.7 \cdot 10^{-5}$. For $\tilde{C} = -3.11 \cdot 10^{-4}$ (panels (e) and (f)) all modes exept H_0 and H_1 get more stable. The range of stability of H_0 shrinks so much, that now H_1 becomes the mode with the biggest stability range. The panels (b), (d) and (f) reveal, that the branch points (black dots) are shifted to higher gain values for growing $\tilde{C}$.

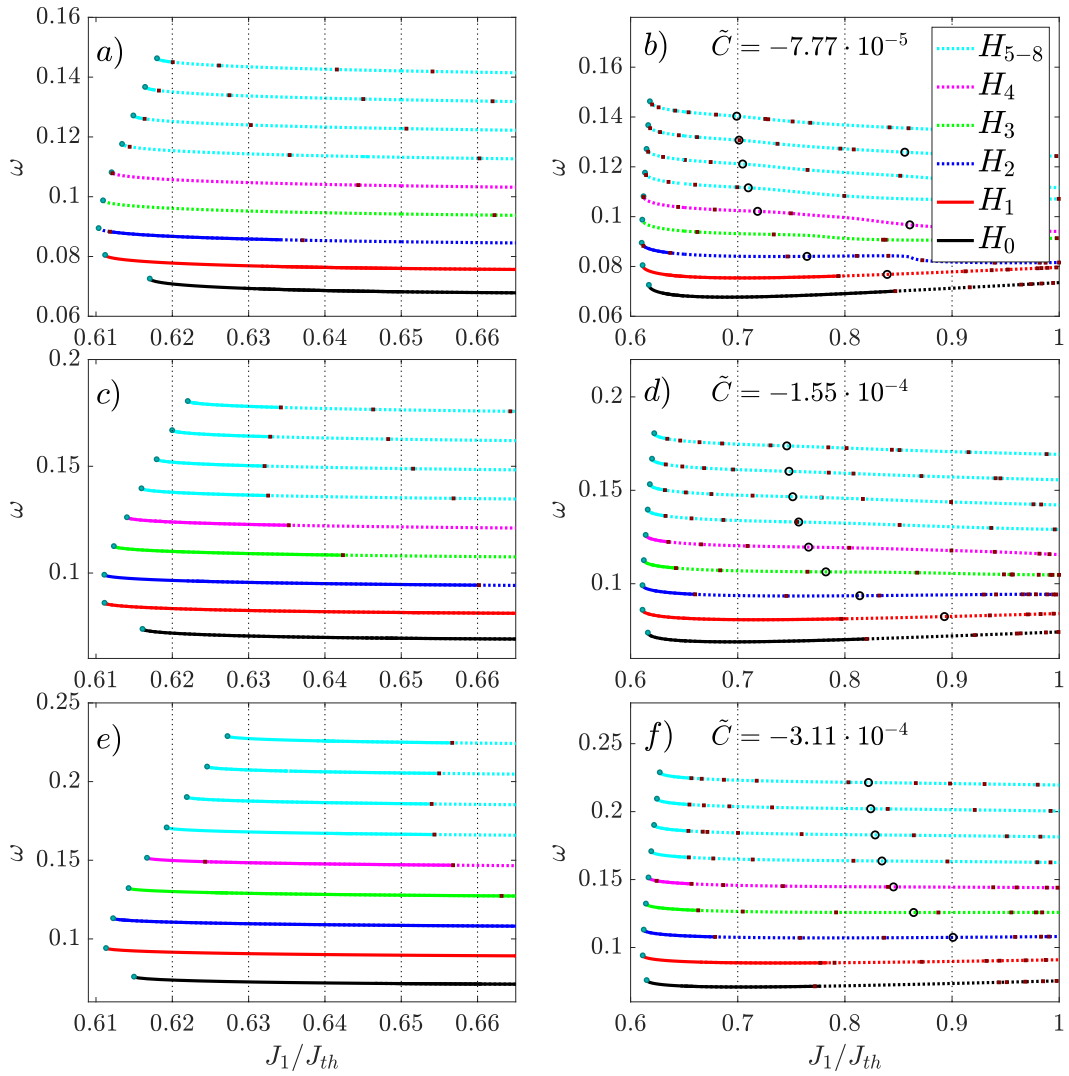

Figure 3.19: First 9 Hermite-Gaussian branches (for different values of C) in ω with respect to J_1/J_{th}, due to clarity reasons only the high-intensity branches are plotted. (a) and (b) show the branches for $\tilde{C} = -7.7 \cdot 10^{-5}$, (c) and (d) for $\tilde{C} = -1.55 \cdot 10^{-4}$, (e) and (f) for $\tilde{C} = -3.11 \cdot 10^{-4}$. Stable parts of the branches are represented by solid lines, unstable parts by dotted lines. Hopf bifurcations are marked by red squares, fold bifurcations by green dots.

Besides the modes H_0 - H_8, also a very high mode was investigated. Figure 3.20 shows the bifurcation diagram and some intensity profiles of the H_{16} mode for different values of $\tilde{C}$. The three solutions of the mode (coloured profiles in panels (b-d)) are related to the correspondent coloured dots in panel (a). They match very good with the analytically calculated intensity profiles, which are represented by the dashed black profiles. The

matching is also very good for the red mode profile for $\tilde{C} = -6.22 \cdot 10^{-5}$. For this value of $\tilde{C}$ the mode is always unstable. The spatial extension of this mode is almost 100μm, i.e. about 50% of the cavity. The modes intensity slightly decreases when $\tilde{C}$ is increased. The mode gets stable between $\tilde{C} = -6.22 \cdot 10^{-5}$ and $\tilde{C} = -7.77 \cdot 10^{-5}$ in the way, that Hopf point emerges next to the fold point. The stability range is located between these bifurcations. When the value of $\tilde{C}$ increases the Hopf-point shifts towards higher values of J_1/J_{th}, which results in a bigger stability range. For $\tilde{C} \approx -1 \cdot 10^{-4}$, the destabilization mechanism changes and the fold bifurcation is no longer limiting the stability range. From $\tilde{C} \approx -1 \cdot 10^{-4}$ to $\tilde{C} \approx -1.5 \cdot 10^{-4}$, the stability range is limited by two Hopf points. For $\tilde{C} \lesssim -1.5 \cdot 10^{-4}$ the Hopf points collide and the stability range vanishes. This means, that the H_{16} mode looses it's stability for a value of $\tilde{C}$ where the modes H_2 to H_8 are still significantly growing for an increase of the absolute value of $\tilde{C}$ (see Fig. 3.19).

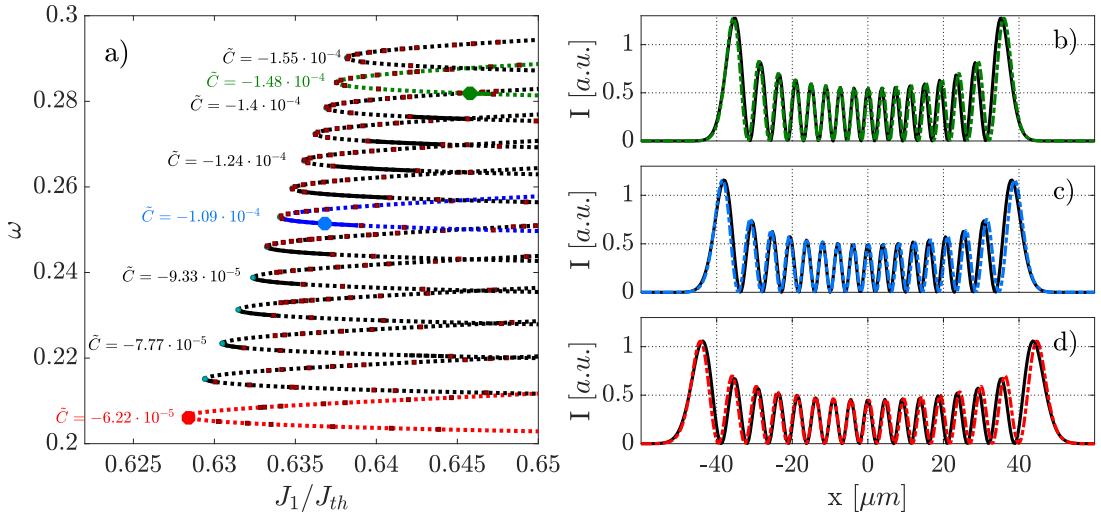

Figure 3.20: (a) Bifurcation diagram in ω with respect to J_1/J_{th} of the H_{16} mode for different values of $\tilde{C}$. The intensity profiles in (b-d) are related to the equivalently coloured dots in panel (a). The dashed black profiles are the analytically calculated intensities. Stable parts of the branches are represented by solid lines, unstable parts by dotted lines. Hopf bifurcations are marked by red dots, fold bifurcations by green dots.

To investigate the influence of $\tilde{C}$ on the mode width, the FWHM of the fundamental mode is illustrated in Fig. 3.21. The FWHM is choosen because it's probably more relevant to the experimenter than σ of the mode width. Both quantities are equivalent, since:

$$\text{FWHM} = 2\sqrt{s \ln 2} \cdot \sigma \quad = \text{const} \cdot \sqrt[4]{-\frac{\tilde{B}}{\tilde{C}}} \tag{3.1}$$

Over the most part of the range of existence of the fundamental mode (panel (a)), the accordance of the analytical and the numerical FWHM is very good. The FWHM just increases slightly from $\tilde{C} \approx -0.47$ to $\tilde{C} \approx -0.1$, going from slightly under to slightly over 2 μm. From there ($-\tilde{C}| \lesssim -0.1$) the FWHM really starts to increase. In panel (b) ($|\tilde{C}| \lesssim -0.01$), the analytical and numerical FWHM show an increasing mismatch.

The analytical value gets a lot bigger, following the inverse fourth-root dependence of Eq. (3.1). E.g., for the standard parameter value ($\tilde{C} = -7.77 \cdot 10^{-5}$) this means FWHM $\approx 7.7\mu$m and FWHM$_{analytical} \approx 13.9\mu$m. This can also be seen in panel (g), which shows the intensity profiles for $\tilde{C} = -7.77 \cdot 10^{-5}$. The panels (c-h) also show the phase (red) of the modes, that changes a lot from $\tilde{C} = -0.455$ (panel (c)) to $\tilde{C} = -1.7 \cdot 10^{-5}$ (panel(h)). For a Hermite-Gaussian mode the phase should be constant over the spatial extension of the mode. This is obviously the case in panel (c) and (d). In panel (e) the phase starts to rise at the tails of the mode. This effect gets stronger for $\tilde{C} \to 0$ and for $\tilde{C} = -1.7 \cdot 10^{-5}$ the phase rise very steap at the tails of the mode. This effect is probably connected to the squeezing of the mode vor small values of $\tilde{C}$. For $|\tilde{C}| \lesssim -0.01$ the simplifications used for the derivation of the fundamental Gaussian mode are obviously not really valid. For the higher modes the matching of the analytical and numerical profiles is significantly better (see e.g. Fig. 3.7 or Fig. 3.9).

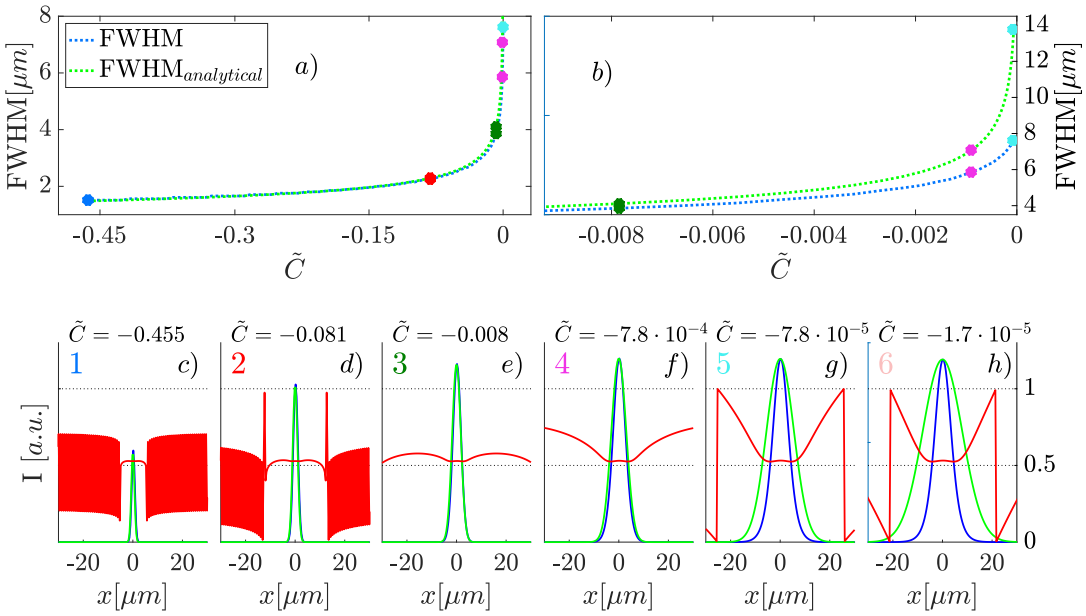

Figure 3.21: (a) FWHM (full width half maximum) of the fundamental Gaussian mode in dependence of $\tilde{C}$ (blue) and the corresponding analytical value (green). (b) detail view for $\tilde{C}$=[-0.009,0]. The panels (c-h) show the analytical (green) and the numerical (blue) intensity profiles of the mode as well as the phase (red) of the solutions marked by the colored dots in (a) and (b). The maximum intensity is normed to the numerical maximum intensity.

3.3.2 Continuation in $\tilde{B}$

Besides $\tilde{C}$, the effective diffraction $\tilde{B}$ is the most relevant parameter to study. Figure 3.22 (a) shows a bifurcation diagram in $\tilde{B}$ with respect to ω for the first seven Hermite-Gaussian modes for $J_1/J_{th} = 0.65$ and $\tilde{C} = -7.7 \cdot 10^{-5}$. The branches got a smooth shape and are well ordered in ω. They differ quite much for high values of $\tilde{B}$ and come together for $\tilde{B} \approx 0.005$, between $\omega = 0.07 - 0.08$ where they turn around in a fold bifurcation and go back to higher values of $\tilde{B}$. The modes H_0 and H_1 are stable from approximately $\tilde{B} = 0.005$ up to $\tilde{B} = 1.7$. The H_2 mode shows a very similar stability range, but interrupted by an unstable region from around $\tilde{B} = 0.12$ to $\tilde{B} = 0.7$. The

stability ranges of H_3, H_4 and H_5 are much smaller and just observable in the detail view of Fig. 3.22 (b), whereas H_6 is always unstable. A detail look at the region close to $\tilde{B} \approx 0$ is done in Figure 3.24, where the branches for $\tilde{C} = -7.7 \cdot 10^{-5}$ and $\tilde{C} = -1.55 \cdot 10^{-4}$ are compared. But first a more general visualization of the branches for $\tilde{C} = -1.55 \cdot 10^{-4}$ is done in Fig. 3.23.

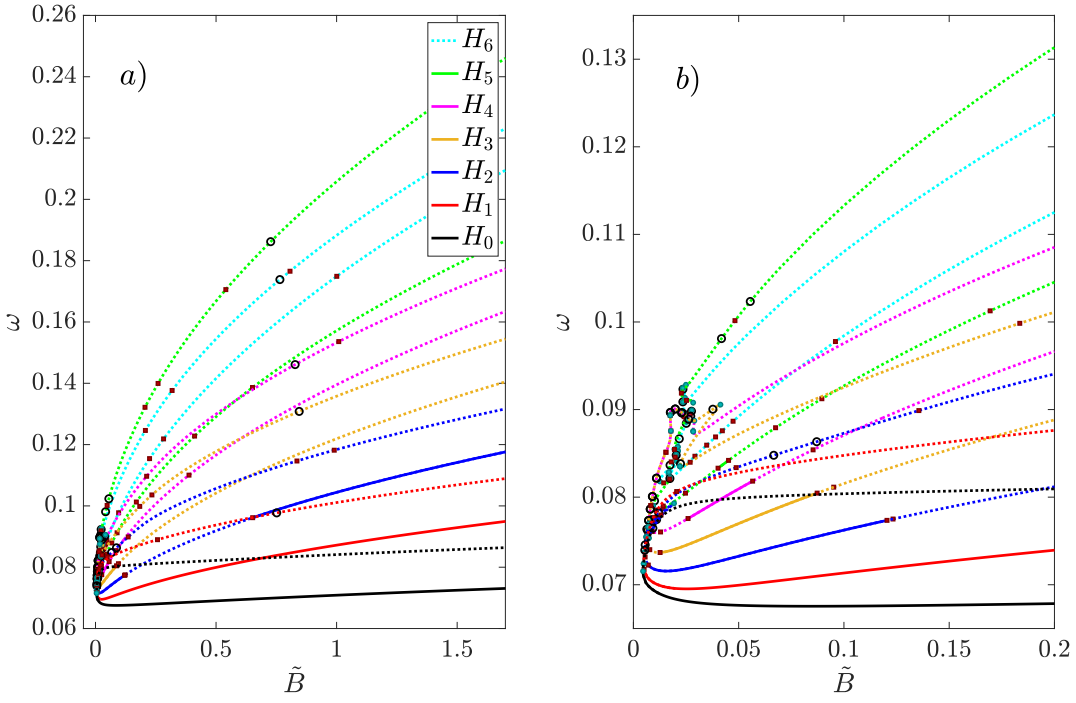

Figure 3.22: Bifurcation diagram of the first seven Germite-Gaussian branches in ω with respect to $\tilde{B}$. (a) illustrates the macro-scale behavior of the braches, while (b) shows a detail view of the most interesting area where the branches turn around. Parameter values: $J_1/J_{th} = 0.65$, $\tilde{C} = -7.7 \cdot 10^{-5}$. Stable parts of the branches are represented by solid lines, unstable parts by dotted lines. Hopf bifurcations are marked by red dots, fold bifurcations by cyan dots.

Figure 3.23 shows the branches in the same range of $\tilde{B}$ and ω as in Fig. 3.22, but for a doubled potential of $\tilde{C} = -1.55 \cdot 10^{-4}$. While the shape of the branches for $\tilde{C} = -1.55 \cdot 10^{-4}$ looks basically very similar like for $\tilde{C} = -7.7 \cdot 10^{-5}$ (just the higher branches shift to higher values of ω), the stabilty ranges for the branches H_2 and H_3 grow significantly bigger. The H_2 mode is now stable from $\tilde{B} \approx 0.01$ to $\tilde{B} = 1.7$. The stable part of the branch of H_3 in the interval $\tilde{C} = [0, 0.2]$ (Fig. 3.23 (b)) grows - compared to $\tilde{C} = -7.7 \cdot 10^{-5}$ - just a bit towards higher values of C. However the branch gets stable around $\tilde{B} \approx 0.85$ and stays stable up to $\tilde{B} \approx 1.7$. The stability ranges of H_4 and H_5 are also bigger, H_6 stays unstable.

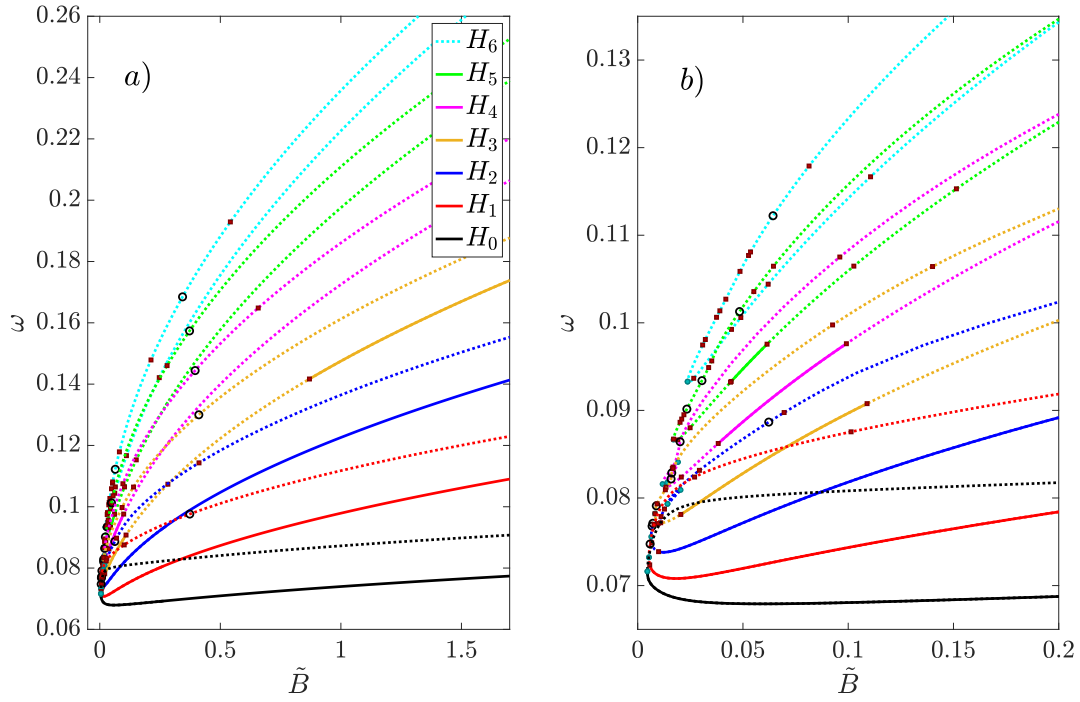

Figure 3.23: Bifurcation diagram of the first five Hermite-Gaussian branches in ω with respect to $\tilde{B}$. (a) illustrates the macro-scale behavior of the branches, while (b) shows a detail view of the most interesting area. Here the stable branches lose their stability and turn around in a saddle-node bifurcation. Parameter values: $J_1/J_{th} = 0.65$, $\tilde{C} = -7.7 \cdot 10^{-5}$. Stable parts of the branches are represented by solid lines, unstable parts by dotted lines. Hopf bifurcations are marked by red dots, fold bifurcations by cyan dots.

Figure 3.24 illustrates the area close to $\tilde{B} \approx 0$. Here we can see, that all branches turn around in a saddle-node bifurcation, but just H_0 loses its stability there, all other branches - if not always unstable - lose their stability in a Hopf bifurcation. The distance of that Hopf bifurcation to the fold point grows with the mode number. For $C = -7.7 \cdot 10^{-5}$ the branches show a more complex structure than for $\tilde{C} = -1.55 \cdot 10^{-4}$. For both values of $\tilde{C}$, H_0 and H_1 turn around at $\tilde{B} \approx 0.005$, going back to bigger values of $\tilde{B}$. For $\tilde{C} = -7.7 \cdot 10^{-5}$ all other branches show a more complex branch, with numerous fold and branch points, going back and forth in $\tilde{B}$. For $\tilde{C} = -1.55 \cdot 10^{-4}$ just H_2 and H_4 show such a shift of direction, but especially the branches of the H_5 and H_6 modes show a way less complex behavior.

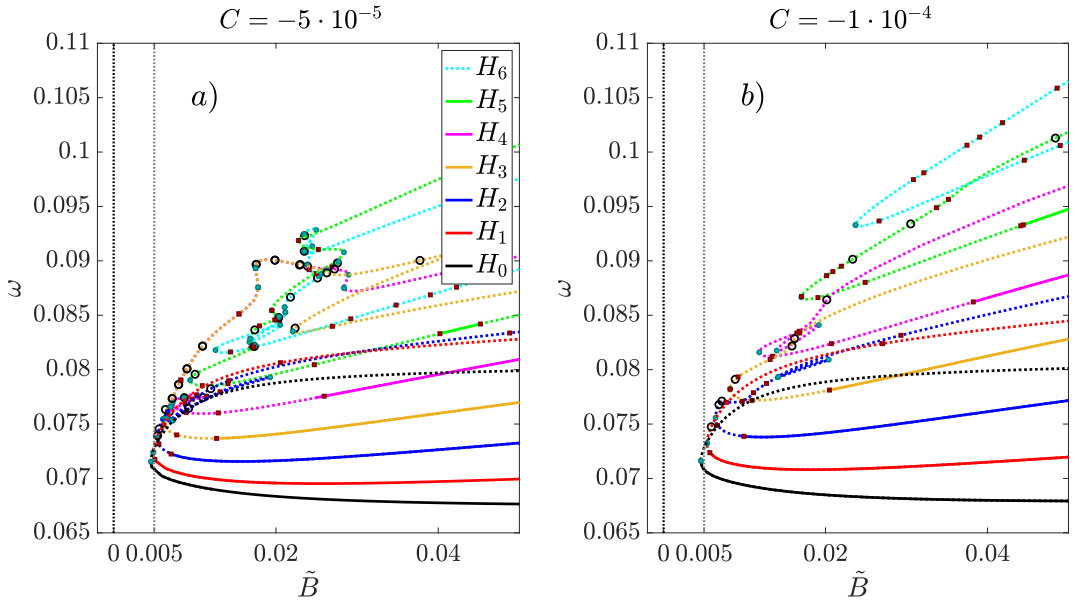

Figure 3.24: Detail view of the bifrucations diagram of the branches of H_0 to H_6 in ω with respect to $\tilde{B}$ close to $\tilde{B} = 0$ for $J_1/J_{th} = 0.65$. (a) shows the branches for $\tilde{C} = -7.7 \cdot 10^{-5}$ and (b) for $\tilde{C} = -1.55 \cdot 10^{-5}$. Stable parts of the branches are represented by solid lines, unstable parts by dotted lines. Hopf bifurcations are marked by red dots, fold bifurcations by cyan dots.

The most interesting observation in Fig. 3.24 is, that the lower-order branches turn around very close to $\tilde{B} = 0.005$, which is the value of the diffusion d. Since the diffraction $\tilde{B}$ and the diffusion d are closely connected by the laplacian $(d+i\tilde{B})\Delta_x$ in equation 2.37, this value seems not to be a coincidence. The Hermite-Gaussian mode vanishes if the diffusion and the diffraction compensate each other.
Figure 3.25 shows the branch of H_0 and some intensity profiles for different values of $\tilde{B}$. In (a) the H_0 branch is shown in ω for six $\tilde{B}$-values from 0.004 to 1.394 and the panels (b)-(g) visualize the intensity profiles (coloured) and phases (black) for these six branches for $J_1/J_{th} = 0.65$. The branches for $\tilde{B} = 1.394$, $\tilde{B} = 1$, $\tilde{B} = 0.528$ and $\tilde{B} = 0.095$ shift to smaller values of ω with growing ranges of stability. From $\tilde{B} = 0.095$ to $\tilde{B} = 0.016$ the branch shifts to higher ω and the stability range grows further, shifting the stability-limiting Hopf point to around J_1/J_{th}=0.87. For $\tilde{B} = 0.004$ the branch gets deformed in J_1/J_{th}, so that the fold point shifts to $J_1/J_{th} = 0.65$, while the Hopf point shifts to $J_1/J_{th} \approx 0.815$.
As expected by the theory (equation 2.32, $\sigma^2 = \sqrt{-\frac{\tilde{B}}{\tilde{C}}}$), the mode width grows with $\tilde{B}$, though the biggest change of the mode width happens close to $\tilde{B} = 0$, due to the fourth root dependence. This can be seen in Fig. 3.25 (b-g). For the profiles in the panels (f) and (g), where the mode width is less than 5μm, also the maximum intensity reduces significantly. The same behavior was already observed for very large values of $\tilde{C}$ (see Fig. 3.21) and is expectable by the fact, that the available gain area reduces with the mode width.

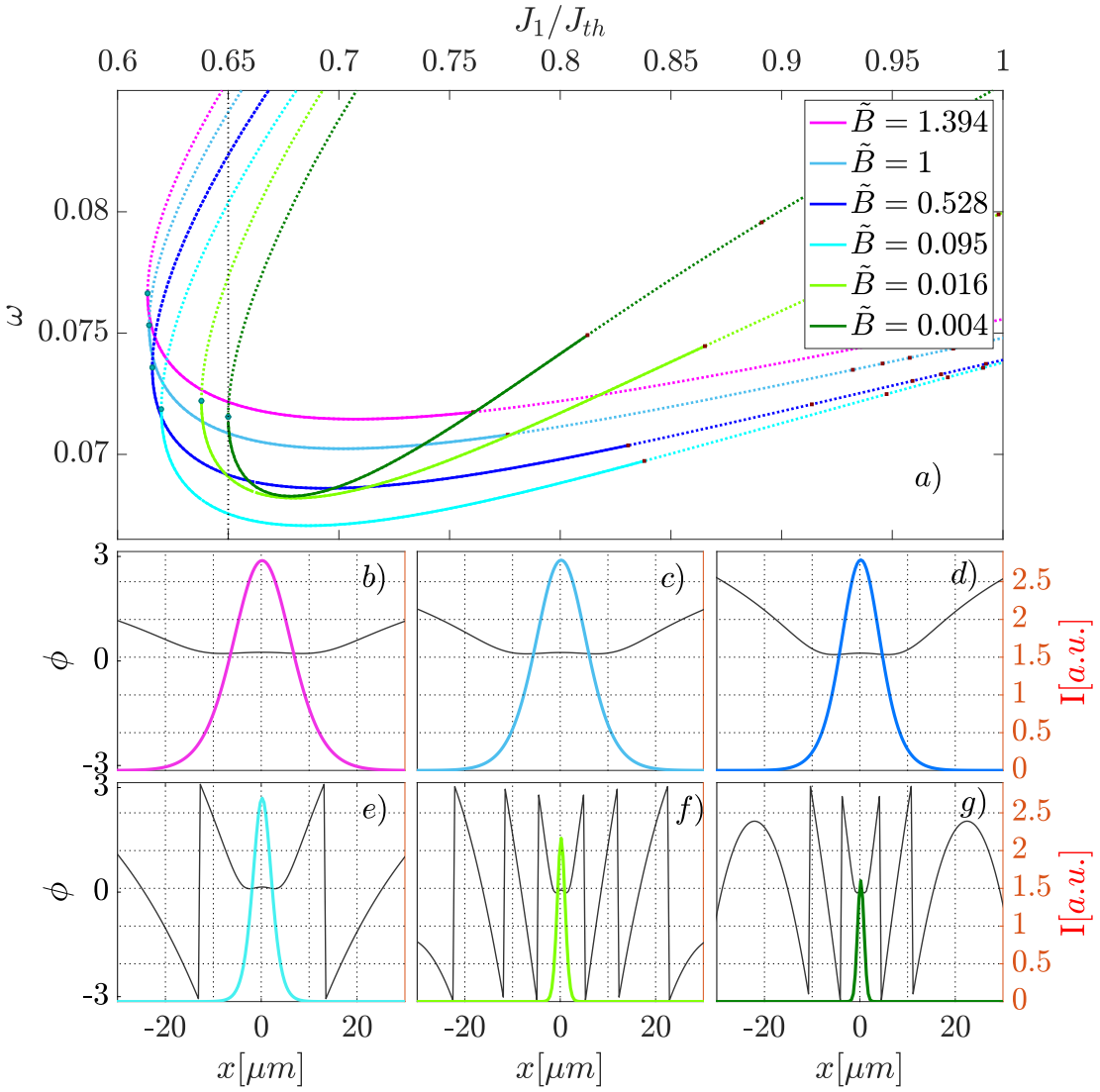

Figure 3.25: (a) Bifurcation diagram in ω with respect to J_1/J_{th} for the H_0 mode and different values of $\tilde{B}$. (b)-(g) Intensity profiles (equivalently coloured) and the phase (black) for all branches in (a) for $J_1/J_{th} = 0.65$.

3.3.3 Continuation in d

d is the parameter of the linear field diffusion. Because the diffusion d and the diffraction $\tilde{B}$ are connected by the laplacian in equation 2.26, they have a strong interaction. In the bifurcation diagram of $\tilde{B}$ for the Hermite-Gaussian branches, we saw that the minimal value of $\tilde{B}$ for the existence of the modes is limited by the value of d. However, for the theoretical derivation of the Hermite-Gaussian modes, the assumption of vanishing diffusion was made.
Figure 3.26 shows bifurcation diagrams of the first five Hermite-Gaussian branches for the total intensity I_{tot} (a) and the spectral parameter ω (b) with respect to the diffusion parameter d. For $d < 0$ all branches show many Hopf points but stable states do not exist. The branches are only stable in the range $d \geq 0$ (just H_0 and H_1 are stable for $d = 0$) and the range of stability reduces with increasing mode number. The H_0 mode shows the biggest range of stability, limited by a Hopf bifurcation at $d = 0$ and a saddle-

node bifurcation at $d \approx 0.23$. The stability range of H_1 is limited by a Hopf bifurcation at $d = 0$ and a fold bifurcation at around $d = 0.105$. The H_2 mode gets unstable for $d \approx 0.01$. The stability ranges towards increasing d are limited by Hopf bifurcation next to the saddle-node bifurcation, where the branch turns around. The branches of H_3 and H_4 show the same behavior, exept that the stability range reduces. These statements are highly dependent on the values of J_1/J_{th}, $\tilde{B}$ and $\tilde{C}$.

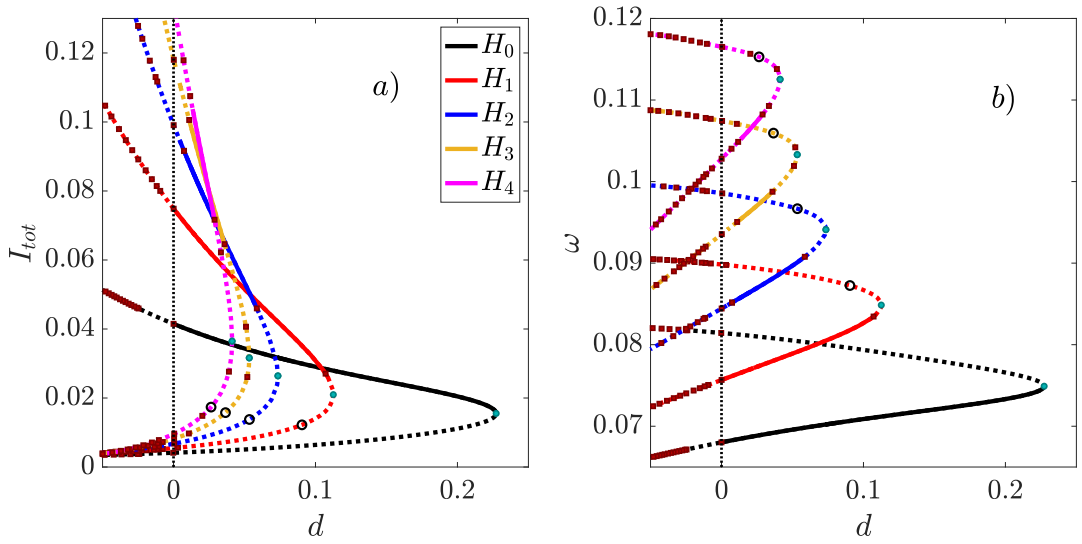

Figure 3.26: Bifurcation diagram of the first five Hermite-Gaussian branches for the total intensity I_{tot} (a) and the spectral parameter ω (b) with respect to the diffusion parameter d. Stable parts of the branches are represented by solid lines, unstable parts by dotted lines. Hopf bifurcations are marked by red squares, fold bifurcations by cyan dots. Other parameter values are: $J_1/J_{th} = 0.65$, $\tilde{B} = 0.2914$, $\tilde{C} = -7.77 \cdot 10^{-5}$.

3.3.4 Nonuniform Gain Profile

Up to this point, all calculations were performed considering a gain section which is uniform and extended over the hole transverse domain (periodic boundary conditions). However in a real experimental setup, the gain section is obviously spatially limited and not constant. Also the light field is not spatially limited to the gain section. In the following, the gain profile is changed to a Gaussian shape with a cut off at a certain percentage of the transverse domain extention.

Figure 3.27 (f) visualizes the branches for a constant gain (black) compared to a gaussian shaped gain profile with a FWHM (full width half maximum) of 100 μm and a cut off at 80% of the domain (grey). Also the intensity of the H_3 mode (which is also plotted in panel (e)) is illustrated to give an idea about the scales. The branches corresponding to the Gaussian gain profile are marked by thick lines in panel (a), while the branches for the costant gain value are marked by thiner lines. The H_0 mode branches of both gain profiles are very similar. The higher branches for the gaussian gain profile show a growing shift to higher gain values compared to the branches for a constant gain. This shift is expectable for a Gaussian gain profile, because the gain reduces significantly (in first order quadratic) with linearly growing mode width. Besides this shift in gain the branches show a very similar shape. Compared to the constant gain branches the ranges of stability of H_0 and H_1 stay approximately the same. For the H_2-mode the range of

stability grows significantly and for H_3 it decreases, while the higher modes are alwaly unstable. For all modes exept H_0 the ranges of stability are limited by two Hopf points.

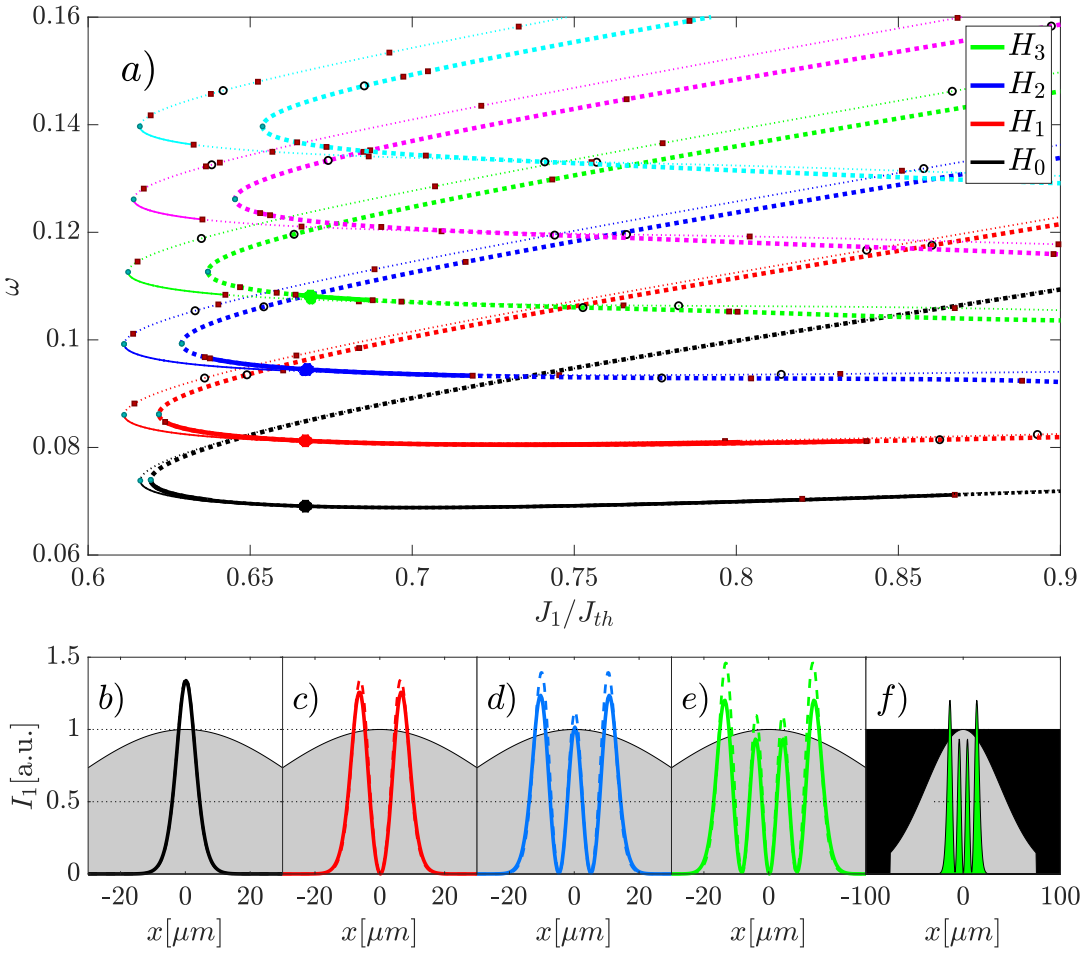

Figure 3.27: Bifurcation diagram for the spectral parameter ω with respect to the normalized primary continuation parameter J_1/J_{th} for the first six Hermite-Gauss modes (a). The thicker branches (right) correspond to a gaussian gain profile with a FWHM of 100 μm and a cut-off at 80% of the domain, while the thiner branches (left) correspond to the constant gain profile over the hole domain. The two gain profiles are shown in f) together with the H_3 mode for a visualization of the relative size of the mode compared to the (pumped) domain. b)-e): the intensity profiles corresponding to the coloured dots in (a). The profiles for the constant gain are visualized dashed, the profiles corresponding to the gaussian shaped gain are prepresented by solid lines. Other parameter values are: $\tilde{C} = -1.55 \cdot 10^{-4}$, $\tilde{B} = 0.2914$.

Figure 3.27 (b-e) presents the intensity profiles of the first 4 modes (solid line) together with the shape of the gain profile. The dashed line shows the intensities for the constant gain. The difference between both intensities is not noticeable for H_0 and very small for H_1. For the higher mode it grows pretty similar like the branches shift to higher gain values.

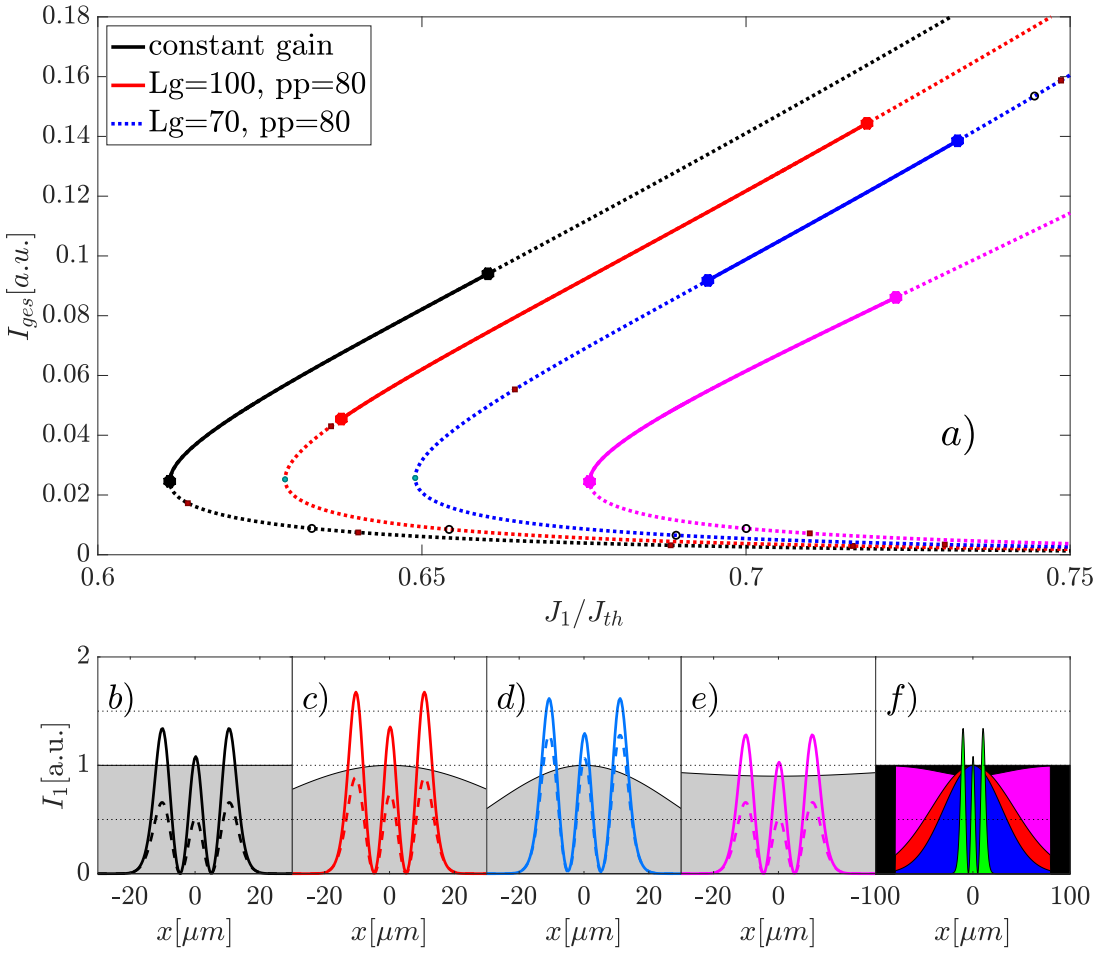

Figure 3.28: Bifurcation diagram of H_2-modes corresponding to different gain profiles for the total intensity I_{ges} with respect to the normalized primary continuation parameter J_1/J_{th}. The colour of the branches indicates how the branches in a) are related to the gain profiles (grey) and intensity profiles (coloured) in b)-e). f) shows the different gain profiles in the colour of their corresponding branch and the H_2 modes intensity profile for constant gain at the stability-limiting Hopf point. Other parameter values are: $\tilde{C} = -1.55 \cdot 10^{-4}$, $\tilde{B} = 0.2914$.

To evaluate the influence of the gain profile on the mode stability in more detail the branch of the H_2-mode is shown in Fig. 3.28 for three different profiles. The H_2 mode is choosen because its the only mode which range of stability is larger for a gaussian gain profile with a FWHM of 100 μm than for the constant gain.
Figure 3.28 (a) shows the branches for the constant gain (black), two gaussian profiles (FWHM 100 μm = red, FWHM 70 μm = blue) and a constant gain profile with a small, gaussian shaped depression (magenta). Obviously the range of stability grows significantly from the black to the red branch and shrinks again for the blue branch. Also it shifts to higher gain values, while the fold point loses it's stability. The magenta coloured branch of the gain profile doesnt really differs from the black one, despite the shift to higher gain values. This is also evident by looking at the corresponding intensity profiles in Fig. 3.28 (b-e). The dashed intensity profile is related to the coloured dot

limiting the range of stability to low gain values in, while the solid line is related to the dot on the high intensity end of the stable range. Here also the intensity profiles in b) and e) look very similar, affirming that the shift in gain is caused by the fact, that the magenta gain profile is 10% reduced in value in the middle of the cavity, compared to the constant gain profile. The intensity profiles related to the gaussian shaped gain profile in the panels (c) and (d) are considerably higher.

3.3.5 Sign Change of $\tilde{B}$ and $\tilde{C}$

Up to this point, all parameter studies where limited to the case $\tilde{B} > 0$ and $\tilde{C} < 0$ (quadrant (d) in Fig. 3.29). However stable Hermite-Gaussian modes should also exist for $\tilde{B} < 0$ and $\tilde{C} > 0$ (quadrant (a)), which follows from the expression of the mode width σ, as already stated in the theoretical introduction of the Hermite-Gauss modes (see Fig. 3.29).

$$mode - width:$$

$$\sigma^2 = \sqrt{-\frac{\tilde{B}}{\tilde{C}}}$$

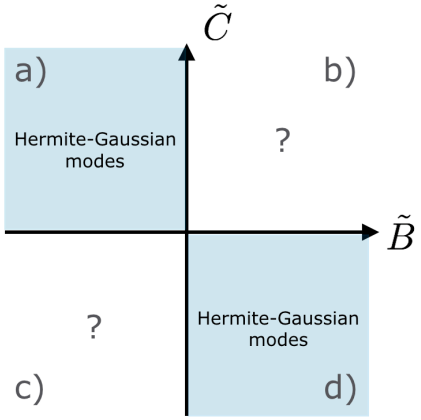

Figure 3.29: The four quadrants to of the ($\tilde{B}$,$\tilde{C}$)-plane, corresponding to the four possible combinations of the two parameters. In the quadrants (a) and (d) $\tilde{B}$ and $\tilde{C}$ have opposite signs, i.e. the stability of Hermite-Gaussian modes is theoretically predicted. In the quadrants (b) and (c) the signs of the parameters are equal and Hermite-Gaussian modes can not exist due to the theoretical derivation.

These Hermite-Gaussian modes are investigated in the following and compared to the ones in quadrant (d). Due to the theory, Hermite-Gaussian modes do not exist in the quadrants (b) or (c), since their width become negative for equal signs of $\tilde{B} > 0$ and $\tilde{C} < 0$. However continuations revealed that the fundamental H_0 mode can cross the boundary from quadrant (a) to b) as we will see later. Other types of solutions can potentially exist in these quadrants. A short introduction to the possible existence of multimode stable states in the quadrants (b) and (c), in the context of a modified equation will be treated in the outlook.
A comparison of the first seven Hermite-Gaussian branches for ω with respect to J_1/J_{th} for the (standard) parameter values $\tilde{B} = 0.2914/B = -18$ and $\tilde{C} = -7.8 \cdot 10^{-5}/C = -5 \cdot 10^{-5}$ (upper seven branches) and the inverted values $\tilde{B} = -0.2914/B = -32.8$ and (lower seven branches) $\tilde{C} = 7.8 \cdot 10^{-5}/C = 5 \cdot 10^{-5}$ is presented in Fig. 3.30.

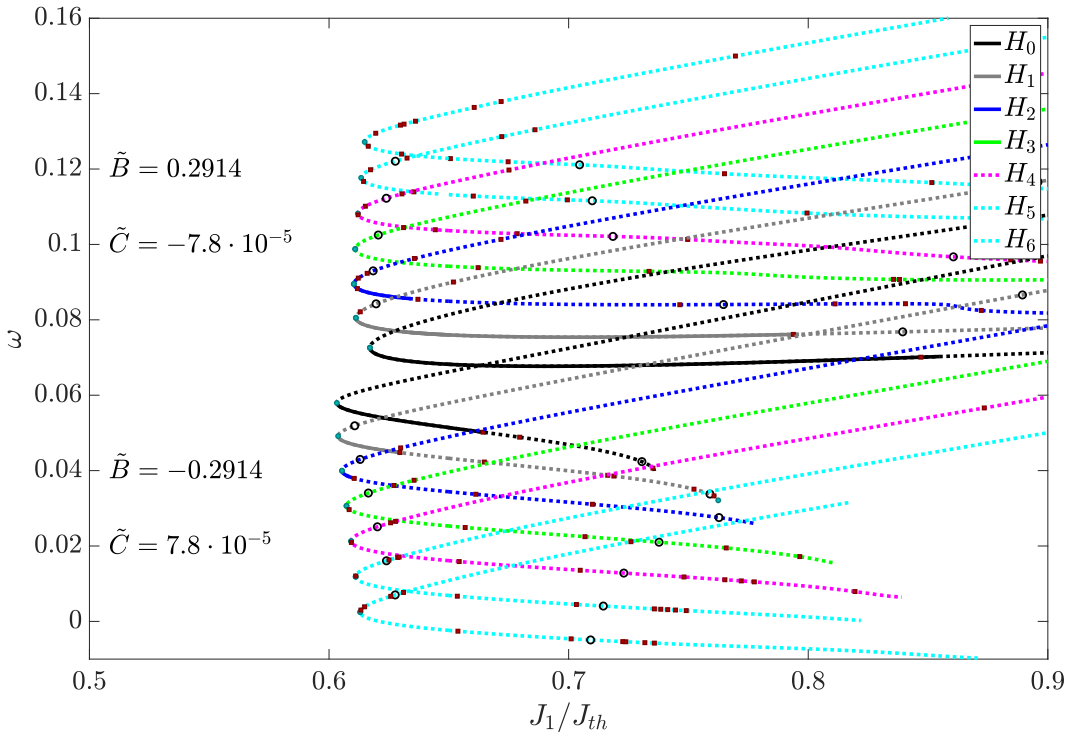

Figure 3.30: Bifurcation diagram of the first seven Hermite-Gaussian branches for the spectral parameter ω with respect to the gain value J_1/J_{th}. The values of the diffraction and the potential are $\tilde{B} = 0.2914$ and $\tilde{C} = -7.8 \cdot 10^{-5}$ for the upper 7 branches (quadrant (d) in Fig. 3.29) and the inverted values $\tilde{B} = -0.2914$ and $\tilde{B} = 7.8 \cdot 10^{-5}$ for the lower 7 branches (quadrant (a)).

Like the branches for the standard parameter values (upper seven branches in Fig. 3.30), the branches for the inverted values (lower seven branches) are also well sorted in ω, but with decreasing ω for growing mode number.The stabilization mechanisms are basically the same. The branches arise of saddle-node bifurcation, that are the stability-limiting bifurcations. Other than for the standard parameter values ($\tilde{C} = -7.7 \cdot 10^{-5}$,$\tilde{B} = 0.291$), where the H_2-mode is limited by two Hopf bifurcations, the stable parts of the branches for the inverted parameter values are always limited by a saddle-node and a Hopf bifurcation.
The stability ranges for the inverted parameter values are significantly reduced. The stability range of H_0 is reduced by approximately 70% and of H_1 by more than 80% compared to the standard values of $\tilde{B}$ and $\tilde{C}$. The branches of H_4, H_5 and H_6 are always unstable. This behavoir changes dramatically, when the values of $\tilde{B}$ and $\tilde{C}$ are significantly increased. This is examplarily illustrated in Fig. 3.31, which shows the Hermite-Gaussian branches H_0 to H_7 for $\tilde{B} \pm 0.9682$ and $\tilde{C} \mp 1.6 \cdot 10^{-3}$ in the upper/lower half. For these values all branches show significant stability and especially the stability ranges of the higher modes $H_4 - H_7$ are considerably larger for the inverted parameter values.

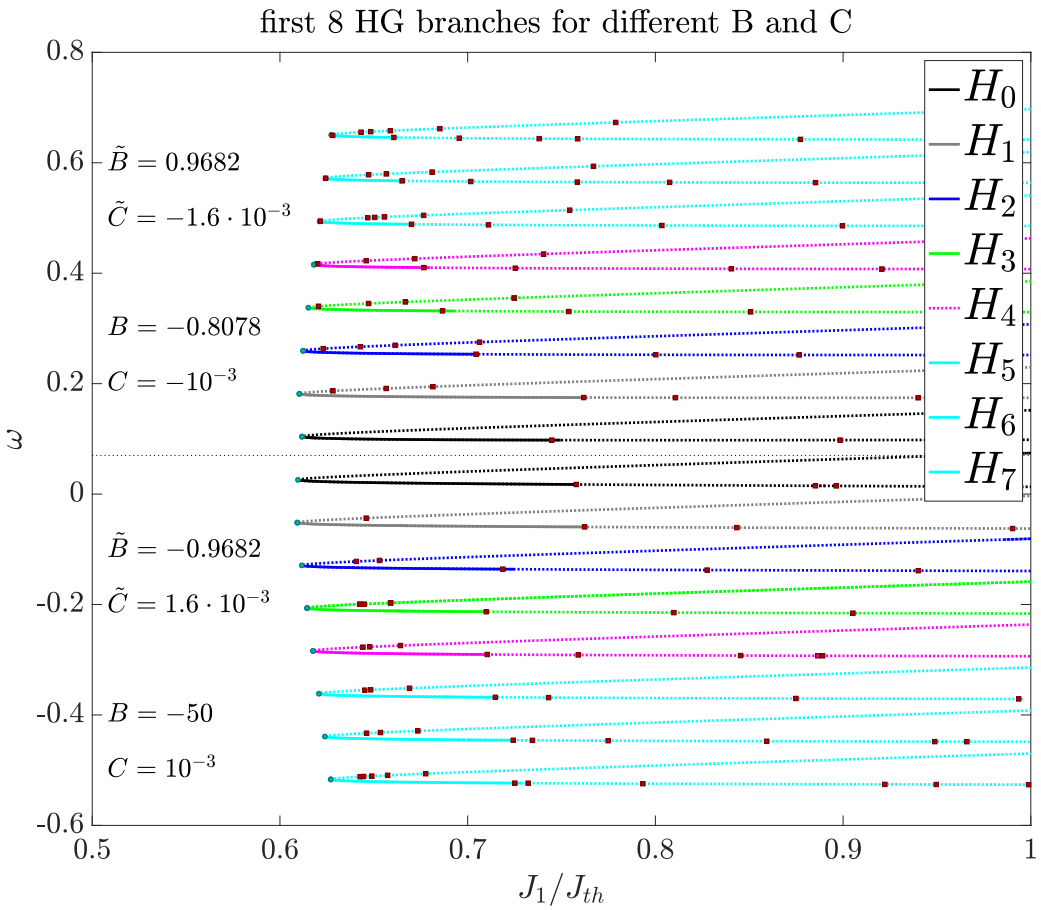

Figure 3.31: Bifurcation diagram of the branches $H_0 - H_7$ in ω with respect to the gain parameter J_1/J_{th}.

Remarkable is that for both signs of the parameters the stability range of H_1 is bigger than that of the fundamental mode H_0. Also the stability for $\tilde{B} = 0.9682$ and $\tilde{C} = -1.6 \cdot 10^{-3}$ decreases continuously from H_1 to H_7 (upper branches), while for $\tilde{B} = -0.9682$ and $\tilde{C} = 1.6 \cdot 10^{-3}$ it decreases from H_1 to H_4 but grows again from H_4 to H_6, which is pretty counterintuitive. To get a better picture of the stability behavior of the HG-modes in the $(\tilde{B}, \tilde{C})$-plane the Figs. 3.32 and 3.33 show a 3-dimensional plot of the stability range in J_1/J_{th} for a given pair of $(\tilde{B}, \tilde{C})$-values. The parameter values are in the intervals $|\tilde{B}| < 1.4$ and $|\tilde{C}| < 7.8 \cdot 10^{-4}$. For the choosen parameter ranges the total stability of both H_0 and H_2 is significantly larger in quadrant (d) than in quadrant (a).
For the standard parameter values of $(\tilde{B}, \tilde{C}) = (0.2914, -7.7 \cdot 10^{-5}$ the range of stability of the fundamental mode is approximately 3 times bigger than for $(\tilde{B}, \tilde{C}) = (-0.2914, 7.7 \cdot 10^{-5}$ (Fig. 3.32). However in quadrant (c) the stability range quickly decreases for growing parameter values, while in quadrant (a) the contrary is the case, both for a growing diffraction $\tilde{B}$ and a growing potential $\tilde{C}$. For the values at the boundaries of Fig. 3.32 the stability ranges of quadrant (a) are very compareable to those of quadrant (d).

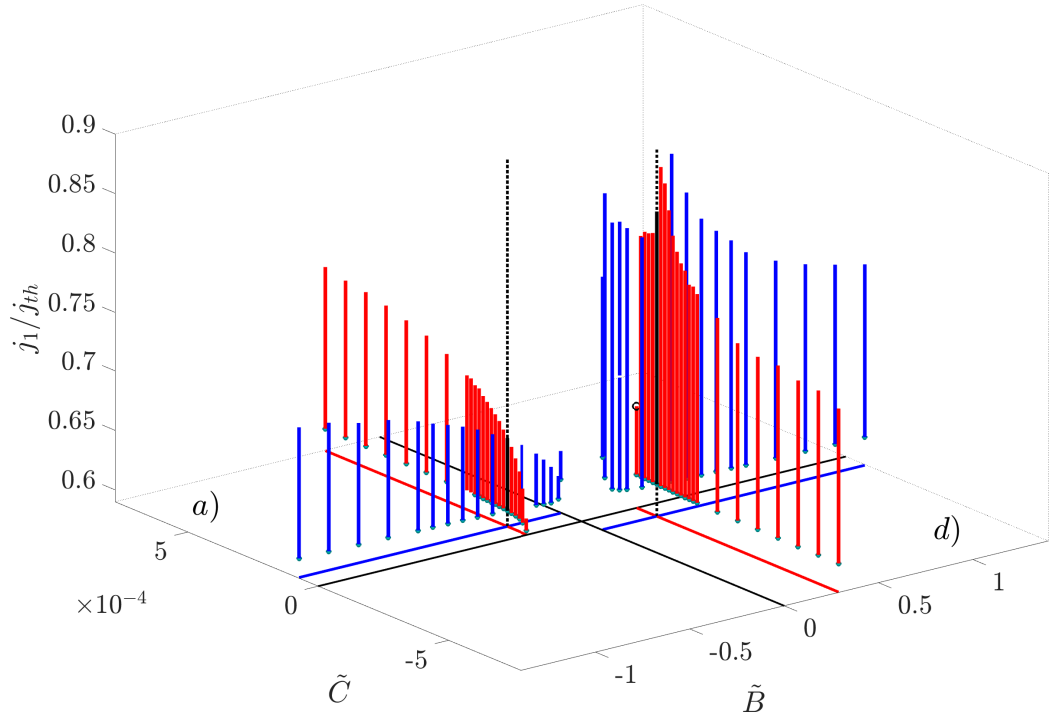

Figure 3.32: Plot of the stability range in J_1/J_{th} with respect to $\tilde{B}$ and $\tilde{C}$ for the fundamental mode. The colored vertical bars show the stability range in J_1/J_{th}, while the bars in the $(\tilde{B}, \tilde{C})$-plane show the corresponding projection of the stability range to provide a better overview. The red bars represent pairs of ($\tilde{B}$,$\tilde{C}$)-values, with $\tilde{B}$ fixed to $\tilde{B} = \pm 0.2914$, while the blue bars correspond to a fixed $\tilde{C}$ of $\tilde{C} = \pm 7.7 \cdot 10^{-5}$ and the two vertical black bars visualize the "standard" parameter values, i.e. the pair $(\tilde{B}, \tilde{C}) = (\pm 0.2914, \mp 7.7 \cdot 10^{-5}$. For clarity reasons the bar density increases towards $\tilde{B} = \tilde{C} = 0$. The quadrants (a) and (d) are labeled like in Fig. 3.29.

The H_2-mode (Fig. 3.33) is generally less stable than the fundamental mode, this is espacially true for ($\tilde{B}$,$\tilde{C}$)-values near to the standard values (horizontal black lines in Fig. 3.33). While the stability range in quadrant (a) is increasing constantly for growing values of $\tilde{B}$ and $\tilde{C}$, the behavior in quadrant (d) is more complex. Starting from the standard values the growth of the stability range is less steep and flattens towards the boundaries of the panel, whereas in quadrant (a) the growth is much more constant and increases slightly to bigger parameter values.

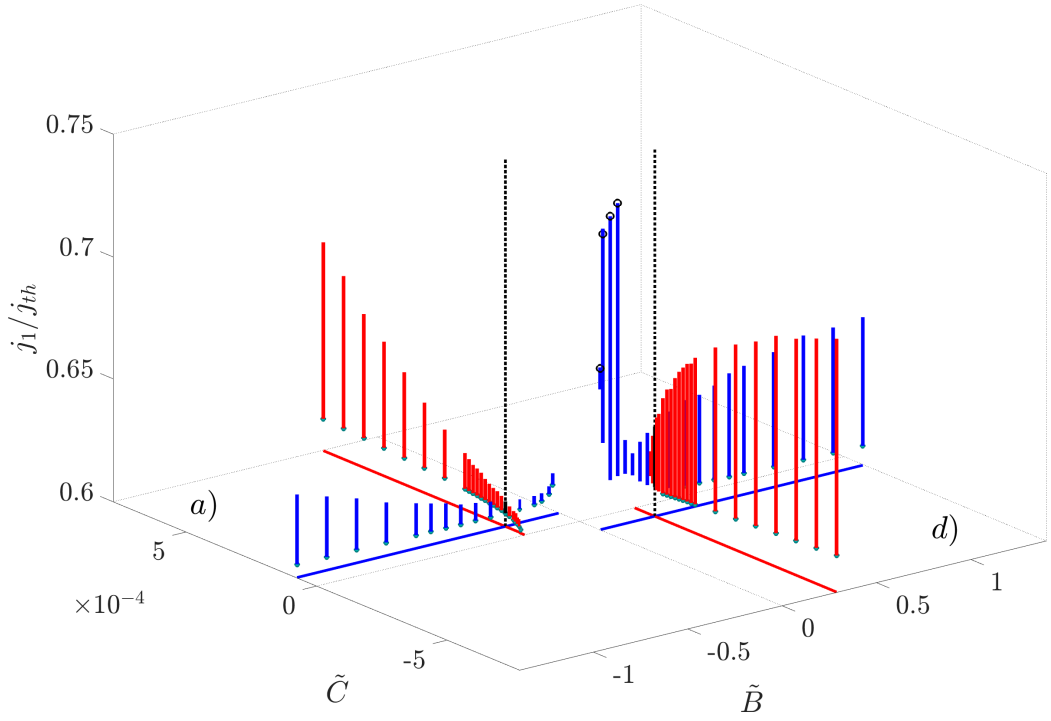

Figure 3.33: Plot of the stability range in J_1/J_{th} with respect to $\tilde{B}$ and $\tilde{C}$ for the H_2-mode. The representation is equal to that of the fundamental mode in Fig. 3.32.

The change of the stability range in quadrant (d) of Fig. 3.33 for $\tilde{B} \to 0$ (blue bars) is the most interesting observation. For $B \approx 0.1$ the stability reaches it's maximum, ranging from $J_1/J_{th} \approx 0.62$ to $J_1/J_{th} \approx 0.75$. Fig. 3.34 provides a more detailed view on this highly nonlinear behavior of the H_2 mode in quadrant (d) and reveals that it is not limited to a specific pair of ($\tilde{B}$,$\tilde{C}$)-values. For $\tilde{B} = 0.095$ the range of stability stays pretty constant from $\tilde{C} = -0.1 \cdot 10^{-4}$ to $\tilde{C} = -1.6 \cdot 10^{-4}$. To bigger values of $\tilde{B}$ the stability decreases significantly. For $\tilde{B} = 0.291$ and $\tilde{C} \gtrsim -5 \cdot 10^{-4}$ no stable solutions exist and the stability range for $\tilde{C} \lesssim -5 \cdot 10^{-4}$ is much smaller than for $\tilde{B} = 0.095$. It would be interesting to see how the stability of the other modes looks like in this representation.

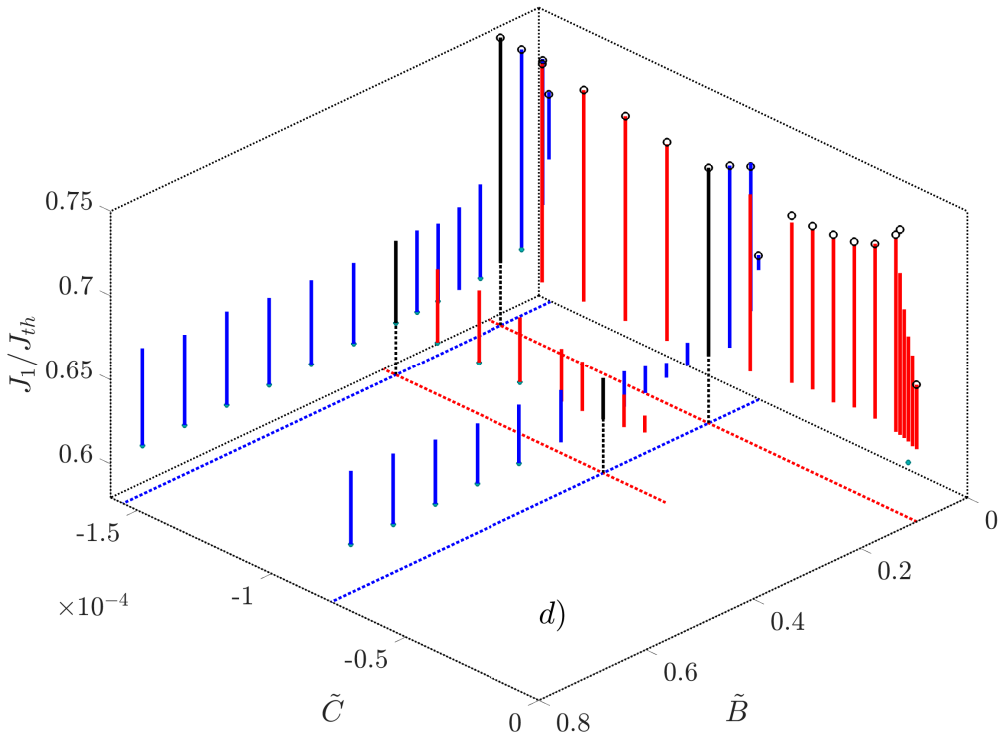

Figure 3.34: Detail view of the stability range in J_1/J_{th} with respect to $\tilde{B}$ and $\tilde{C}$ for the H_2-mode. The vertical lines represent the stability range for a given pair of ($\tilde{B}$,$\tilde{C}$)-values. The vertical blue bars exhibit a fixed value of $\tilde{C} = -7.8{\cdot}10^{-5}$ and $\tilde{C} = -1.55{\cdot}10^{-4}$, whereas the red vertical bars correspond to the values $\tilde{B} = 0.095$ and $\tilde{B} = 0.291$. The dotted horizontal lines are a projection within the range of the vertical lines in the ($\tilde{B}$,$\tilde{C}$,0)-plane. The vertical lines at the intersection points of these horizontal lines are black with a dotted connection to the ($\tilde{B}$,$\tilde{C}$,0)-plane for better visualization.

Besides the investigation of the Hermite-Gaussian modes in the quadrants (a) and (d) of the sketch in Fig. 3.29, the search for solutions in the quadrants (b) and (c) was of interest. The attempt to try different initial solutions and parameter combinations in direct numerical sumilations to find stable solutions in these quadrants was unsuccessful. Though the existence of Hermite-Gaussian modes for equal signs of $\tilde{B}$ and $\tilde{C}$ is theoretically not possible, the possibility of crossing the boundary from one quadrant to another is of high interest. One example is given in Fig. 3.35. This example is the changeover from quadrant (a) to quadrant (b), going from $\tilde{B} < 0$ to $\tilde{B} > 0$ given $\tilde{C} = 2 \cdot 10^{-2}$. The fundamental mode (black) looses its stability at around $\tilde{B} = -0.03$ in a Hopf bifurcation and becomes stable again at $\tilde{B} = 0.04$, then the branch turns around and gets unstable in a fold bifurcation at $\tilde{B} \approx 0.11$. The mode - which shows a gaussian intensity distribution for $\tilde{B} < 0$ (panel b) - gets deformed for $\tilde{B} > 0$. The deeper the localized state ingresses in the region $\tilde{B} > 0$, the further it's dispersed spatially. The real part, which is just a single pulse for $\tilde{B} < 0$ starts to oscillate with a growing number of oscillations (see Fig. 3.35 (d-f)).

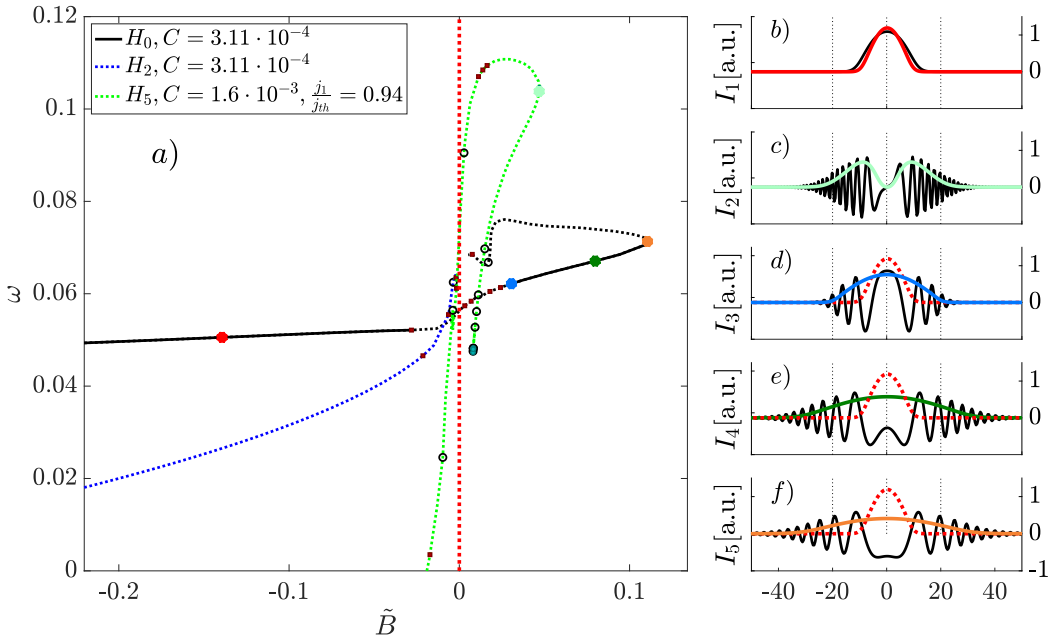

Figure 3.35: (a): Bifurcation diagram of the Hermite-Gaussian modes H_0 (black), H_2 (blue) and H_5 (green) in ω with respect to $\tilde{B}$ around $\tilde{B} = 0$. The panel (b-f) show the intensity profiles (coloured) related to the coloured dots and the real parts in a).

Exept the fundamental mode, no other mode can be continued over the boundary $\tilde{B} = 0$ and show stable solutions for $\tilde{B} > 0$. The H_2-mode solution (blue in fFig. 3.35 (a) is either not converging for $\tilde{B} \to 0$ or it "jumps" on the branch of the fundamental mode, if the step size is choosen big enough. Just for gain values near to the laser threshold, some Hermite-Gaussian modes can be continued to the region $\tilde{B} > 0$. As an example the H_5-mode (green in Fig. 3.35 (a) is continued for $J_1/J_{th} = 0.94$. Though the solution of the mode can be continued to $\tilde{B} > 0$, the branch turns around at $\tilde{B} \approx 0.05$ and is not becoming stable. The profile is a spatially extended double pulse (Fig. 3.35 (c) with a strongly oscillating real part (black). This solution is something very different to the H_5-Hermite-Gaussian mode, also the gain value of $J_1/J_{th} = 0.94$ is - due to the earlier results - out of the range of the stable existence of Hermite-Gaussian modes. When trying to continue this solution to smaller gain values, it disappears pretty fast. All results of the continuation work and direct numerical simulations agree with the theoretical prediction, that Hermite-Gaussian modes cannot exist for equal signs of the diffraction $\tilde{B}$ and the potential $\tilde{C}$.. The fundamental mode is just a simple localized state, in the form of a gaussian shaped pulse. Such dissipative solitons can also exist for equal signs of $\tilde{B}$ and $\tilde{C}$, but their stability range and spatial size as well as the characteristics of their real/imaginary parts differ significantly from the properties of Hermite Gaussian modes.

3.4 Supplement

The next step to improve the main equation of this master's thesis is to introduce a bilaplacian diffraction-term (marked red in Eq. (3.2)), which results from a consideration of aberation effects of the lens in our model system:

$$\frac{\partial A}{\partial t} = \Big[(1-i\alpha_1)J_1(r_\perp)h\Big(|A|^2\Big) + (1-i\alpha_2)J_2h\Big(s|A|^2\Big) - k + i\tilde{C}r_\perp^2 + \Big(d+i\tilde{B}\Big)\Delta_\perp + i\tilde{S}\Delta_\perp^2\Big]A. \tag{3.2}$$

This equation is subject of the current research of the examiners of this master's thesis. The derivation of the bilaplacian term will not be done here. For detail information, please contact the examiners. It turns out, that Equation (3.2) is solved by a product of a Hermite-Gaussian function and a sine/cosine. These solutions (called GauCosine and GauSine) can be stabilized for equal signs of $\tilde{B}$ and $\tilde{C}$, which makes them a very interesting subject of future research. Besides this feature, the additional bilaplacian diffraction term in Equation (3.2) can also further stabilize the (Hermite-Gaussian) solutions for opposite signs of $\tilde{B}$ and $\tilde{C}$. In the following, the effect of a bilaplacian diffraction term on the modes H_8 and H_{16} will be illustrated. Figure 3.36 shows the H_8 mode for different values of of $\tilde{C}$ and also $\tilde{S} = 0$ (red branches).

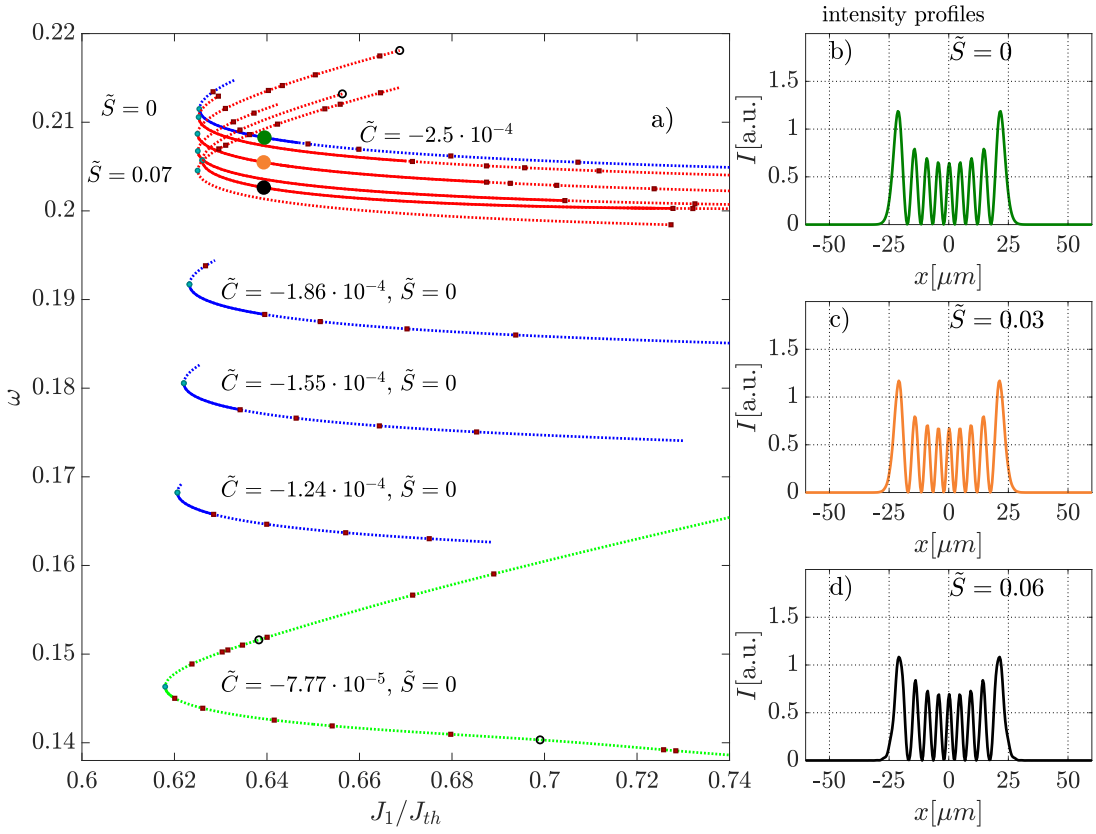

Figure 3.36: (a): Bifurcation diagram of the H_8 mode for different values of $\tilde{C}$ in ω with respect to J_1/J_{th}. The green branch corresponds to the standard parameter values ($\tilde{C} = -7.77 \cdot 10^{-5}$, $\tilde{B} = 0.2914$, $\tilde{S} = 0$), the blue branches correspond to the labeled values of $\tilde{C}$, with $\tilde{S} = 0$. The red branches corresponds to $\tilde{C} = -2.5 \cdot 10^{-4}$, $\tilde{B} = 0.2914$ and $\tilde{S} \neq 0$. The panels (b-d) show the intensity profiles (coloured) related to the equivalently coloured dots in (a). Stable solutions are indicated by solid lines, unstable by dotted lines. Hopf bifurcations are marked by red dots, fold bifurcations by cyan dots.

As already seen in the earlier parameter studies, the range of stability increases with the value of $\tilde{C}$. For $\tilde{S} = 0$, the upper blue branch for $\tilde{C} = -2.5 \cdot 10^{-4}$ has the biggest range of stability. By introducing $\tilde{S} \neq 0$ the range of stability can be increased drastically. Already a value of $\tilde{S} = 0.01$ results in a doupling of the stability range, which rises up to a factor of approximatelly 4 for $\tilde{S} = 0.06$. For $\tilde{S} = 0.07$ however, the mode gets totally unstable. The panels (b-d) show the influence of $\tilde{S}$ on the modes intensity profile. The mode gets deformed in the way, that the two outer peaks shrink a bit while the multiple inner peaks grow slightly, for $\tilde{S} > 0$. The result is obviosly a flattening of the mode.
The H_{16} mode is investigated for a wider range of $\tilde{S} = 0$. Figure 3.37 illustrates that the mode exhibits at least two regimes of stability for $\tilde{S} > 0$. The range of stability grows for $\tilde{S} > 0$ up to $\tilde{S} = 0.04$. Sixteen branches with distance $\Delta\tilde{S} = 0.01$ from $\tilde{S} = -0.02$ to $\tilde{S} = 0.13$ are shown. Compared to the branch for $S = 0$ (upper black branch), the stability range grows even more than for the H_8 mode.

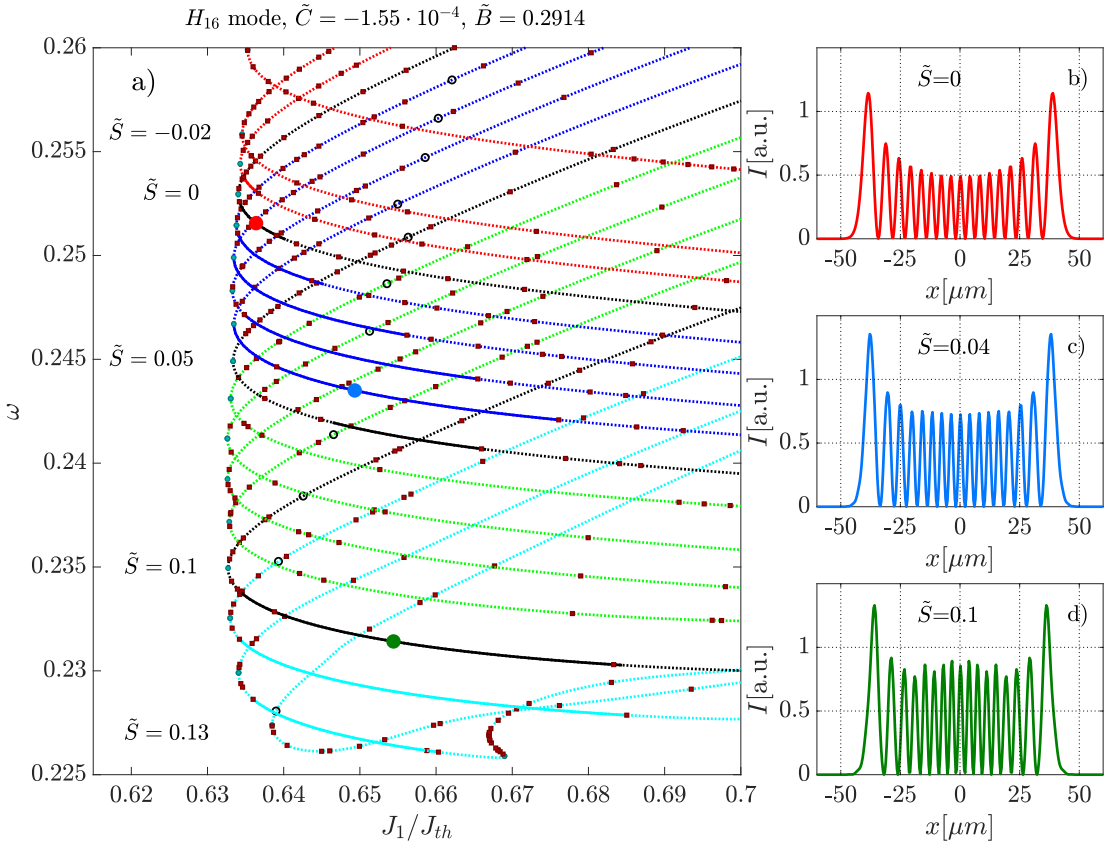

Figure 3.37: (a): Bifurcation diagram of the H_{16} mode in ω with respect to J_1/J_{th} for different values of $\tilde{S}$ ($\tilde{C} = -1.55 \cdot 10^{-4}$ and $\tilde{B} = 0.2914$ for all branches). The branches are equidistantly spaced in S with 0.01 distance and the black branches correspond to the values $\tilde{S} = 0$, $\tilde{S} = 0.05$ and $\tilde{S} = 0.1$. The panels (b-d) show the intensity profiles (coloured) related to the equivalently coloured dots in (a). Stable solutions are indicated by solid lines, unstable by dotted lines. Hopf bifurcations are marked by red dots, fold bifurcations by cyan dots.

The range of stability of the branch for $\tilde{S} = 0.04$ is approximately 5 times bigger than the one for $\tilde{S} = 0$, ranging from $J_1/J_{th} \approx 0.633$ to $J_1/J_{th} \approx 0.676$. For the parameter

values $\tilde{S} = 0.06$ to $\tilde{S} = 0.09$ the branch is always unstable. For $\tilde{S} = 0.1$ the branch suddenly gets stable again, with a bigger range of stability than for a smaller values of $\tilde{S}$. For $\tilde{S} = 0.12$ the branch shows a kink containing numerous Hopf and two fold-bifurcations at around $J_1/J_{th} \approx 0.67$. For $\tilde{S} = 0.13$ the branch is always unstable and deformed compared to the other - well ordered - branches. The influence of $\tilde{S}$ on the intensity profile of the $H_{16}mode$ (panels (b-d)) is generally comparable to the one for the H_8 mode. In panel (c) ($\tilde{S} = 0.04$)the mode is flattenend compared to panel (b) ($\tilde{S} = 0$). For $\tilde{S} = 0.1$ (panel (d)) the inner peaks get enhanced so much that a hump forms in the middle of the mode. Also the mode is slightly spatially shrinking compared to $\tilde{S} = 0$. These results suggest a further investigation of the modified equation including the bilaplacian term not only to find stable solutions for equal signs of $\tilde{B}$ and $\tilde{C}$ but also to stabilize the solutions for opposite signs of $\tilde{B}$ and $\tilde{C}$.

4 Conclusion and Outlook

In this master's thesis a one-dimensional *partial differential equation* (PDE) was derived and analyzed with the aim to describe the electric field inside the micro-cavity of a *mode-locked integrated external-cavity surface emitting laser* (MIXSEL) coupled to a distant mirror via telescopic optics near self-imaging.
In the introduction, a brief overview of the physical background on *lasing localized states* LLSs was given. It was emphasized that these multiple-timescale objects can occur in laser systems below threshold, if a mode-locked solution coexists with the off-solution and the cavity round trip is much larger than the gain recovery time (long cavity limit) [14, 11]. So-called *light bullets* (LBs) were introduced as a special case of these LSs in three dimensions and an experimental setup was introduced where LSs appear [7]. This system consists of a MIXSEL coupled to a distant mirror and is the model system of this master's thesis. The aim of this master thesis was defined as creating a hybrid model combining a PDE and a *delay differential equation* (DDE) that potentially explains pattern formation in the micro-cavity of the MIXSEL.
In the theoretical part, this hybrid model of a MIXSEL and a mirror, coupled via an possibly imperfect imaging system, was derived. This hybrid model first-order approximates the optical system by an $ABCD$-matrix. The final result was found to be a modified Rosanov equation [18], describing the electric field inside the micro-cavity of the MIXSEL (Eq. (2.26)). It was shown that a product of a Hermite polynomial [3] and and a Gaussian pulse (so-called Hermite-Gaussian modes) solves the model equation of our system and also an analytical term for the mode width was deduced (Eq. (2.32)). The term of the mode width indicated, that the Hermite-Gaussian modes exist for opposite signs of the effective diffraction $\tilde{B}$ and the potential $\tilde{C}$. Further, the necessary mathematical tools were described, including *direct numerical simulation* (DNS) and numerical path continuation. For all continuation and bifurcation studies the software package PDE2PATH [9] was used.
In the results section, the occuring stable solutions of the modified model equation where investigated. First, a bifurcation study of the fundamental Gaussian mode in the spectral parameter ω with respect to the normalized laser gain J_1/J_{th} was performed. It revealed that this mode arises of a saddle-node bifurcation and exhibits a partially stable high-intensity branch and a low-intensity branch which is always unstable. The mode is stable for a wide range of the laser gain on the high-intensity branch (below threshold) and gets destabilized via symmetric oscillations in a Hopf bifurcation.
Besides this simple Gaussian pulse, also the other higher order Hermite-Gaussian modes where found and show a similar behavior like the fundamental mode over the widest range of the parameters. Also the branches of the Hermite-Gaussian modes are well sorted in the spectral parameter ω. However, the stability ranges of the higher order modes are significantly smaller. The modes intensity profiles where found to generally match very good with the predicted analytical intensity profiles (see Fig. 3.7). The branch points of some higher order Hermite-Gaussian modes where investigated and it was found that the branching solutions are asymmetrically deformed Hermite-Gaussian modes that are always unstable (see Figs. 3.10 and 3.11).
Next, the critical eigenfunctions at the stability-limiting Hopf bifurcations of the first three Hermite-Gaussian modes were explored. It was demonstrated that the fold points which limit the Hermite-Gaussian branches to vanishing intensity correspond to the first Hopf points of the off-solution above the lasing threshold. Not only match the critical eigenfunctions perfectly, furthermore the imaginary part of the critical eigenvalue of the

off-solution corresponds to the spectral parameter ω of the Hermite-Gaussian modes. Further, the influence of the parameters $\tilde{C}$ (potential) and $\tilde{B}$ (effective diffraction) on the Hermite-Gaussian modes were investigated. The continuation in $\tilde{C}$ showed that the fundamental mode is stable over the hole range of their existence and the stability ranges of the higher order modes are not only a lot smaller, but seperated in two regimes of stability at different orders of magnitude of $\tilde{C}$. The most interesting observation in this context was that the third Hermite-Gaussian mode H_2 shows a regime of bistability of two solutions for a very small value of $\tilde{C} \approx -1 \cdot 10^{-7}$. One of these solutions is rather a combination of three solitary pulses than a Hermite-Gaussian mode.
The analysis also confirmed the theoretical prediction that Hermite-Gaussian modes can only exist for opposite signs of $\tilde{B}$ and $\tilde{C}$. It further showed that the size of the stability range of the modes is highly dependent on the values of $\tilde{B}$ and $\tilde{C}$, and that the modes generally get more stable for increasing values of the parameters. However, a realistic range of $\tilde{B}$ and $\tilde{C}$ is limited by the approximations used in the derivation of the model equation. This is namely the simplification of an $ABCD$-matrix, representing the imaging behavior of the laser cavity, which is valid for the paraxial approximation for very small angles to the optical axis. The highest mode analyzed - the seventeenth Hermite-Gaussian mode H_{16} - showed the biggest stability range for a lot smaller values of C than the lower order modes and matched very well with the analytically predicted mode profile. Whereas the analysis of the fundamental modes width revealed that the mode significantly differs from the analytical one for realistic values of C. The continuation in $\tilde{B}$ showed that the minimum value of $\tilde{B}$ (where the modes turn around in a fold bifurcation) is approximately 0.005, which is the value of the diffusion coefficient in our model equation. The continuation in the diffusion coefficient d showed that stable modes only exist for $d \simeq 0$.
Afterwards, the effect of a nonuniform (instead of a uniform) gain profile was examined and a Gaussian shaped gain profile with a cut-off on each end of the cavity was assumed. The continuation work for this gain profile showed that the stability range of the modes can significantly be increased, if the parameters are choosen correctly.
The last part of the work compared the Hermite-Gaussian modes for pairs of the parameters $\tilde{B}$ and $\tilde{C}$ with inverted signs (i.e. $(\pm\tilde{B}, \mp\tilde{C})$ for $\tilde{B}$,$\tilde{C} > 0$). It turned out that for pairs of inverted values of $\tilde{B}$ and $\tilde{C}$ the modes show quite different ranges of stability. For realistic parameter ranges the case $\tilde{B} > 0$ and $\tilde{C} < 0$ generally leads to a bigger range of stability of the modes. The analysis of the stability range of the third Hermite-Gaussian mode H_2 revealed a highly nonlinear behavior of the stability range for $\tilde{B} \to 0$. Trying to continue the modes from the regime of opposite signs of $\tilde{B}$ and $\tilde{C}$ to equal signs, was unsuccessful. Only the fundamental mode can be continued to the regime of equal signs of $\tilde{B}$ and $\tilde{C}$ but gets distorted to a solitary pulse with a small range of stability which is no longer a Hermite-Gaussian mode.
In the supplement, a modification of the model equation (Eq. (3.2)) was introduced that is subject of current research and delivers stable solutions also for equal signs of $\tilde{B}$ and $\tilde{C}$. It was demonstrated that this modified equation (that considers higher order diffraction due to abberation effects with an additional bilaplacian term) also stabilizes the Hermite-Gaussian modes for opposite signs of $\tilde{B}$ and $\tilde{C}$. The solutions of this equation can be approximated by a product of a Hermite-Gaussian function and a cosine/sine function. In order to further develop the results of this master's thesis, a multiparameter bifurcation study of this equation would be of high relevance. In addition, a full bifurcation study of the main equation of this master's thesis in two dimensions could be considered as a future project.

References

[1] URL: https://www.rp-photonics.com/abcd_matrix.html.

[2] URL: https://en.wikipedia.org/wiki/Numerical_continuation.

[3] Irene Ann Abramowitz Milton; Stegun. "Handbook of Mathematical Functions with Formulas, Graphs, and Mathematical Tables". Applied Mathematics Series. Vol. 55 (December 1972); first ed.1.

[4] Georg K. Allgower E.L. "Introduction to Numerical Continuation Methods. Classics in Applied Mathematics". Society for Industrial Mathematics, Philadelphia (1987).

[5] S. M. Link D. Waldburger M. Golling B. W. Tilma E. Gini C. G. E. Alfieri M. Mangold and U. Keller. "Sub-300fs-MIXSEL". ETH Zurich, Institute for Quantum Electronics, Ultrafast Laser Physics.

[6] V. Bagini C. Palma. "Extension of the Fresnel transform to ABCD systems". J. Opt. Soc. Am. A/Vol. 14, No. 8/August 1997.

[7] Julien Javaloyes Christian Schelte Denis Hessel and Svetlana Gurevich. "Dispersive instabilities in passevely mode-locked external-cavity surface emitting lasers". Phys. Rev. A. 13, 054050 (2020).

[8] Fabian Dohmen. "Bound States of Light Bullets in Semiconductor Laser Systems with Saturable Absorber". Institute for Theoretical Physics, Westfalische Wilhelms-Universitat Munster, 2019.

[9] D. Wetzel H. Uecker and J. D. M. Rademacher. "pde2path – A Matlab package for continuation and bifurcation in 2D elliptic systems". Math. Theory Methods Appl. 7, 58 (2014).

[10] H. A. Haus. "Mode-locking of lasers". IEEE J. Sel. Top. Quantum Electron. 6, 1173 (2000).

[11] J. Javaloyes. "Cavity Light Bullets in Passively Mode-Locked Semiconductor Lasers". Phys. Rev. Lett. 116, 043901 (2016).

[12] Robert Keolian Junru Wu and Isadore Rudnick. "Observation of a Nonpropagating Hydrodynamic Soliton". Phys. Rev. Lett. 52, 1421, 16 April 1984.

[13] L. A. Lugiato. "Nonlinear Optical Structures, Patterns, Chaos". Chaos, Solitons, and Fractals Vol. 4 (Pergamon, New York, 1994), p. 1251.

[14] S. Balle M. Marconi J. Javaloyes and M. Giudici. "How Lasing Localized Structures Evolve Out of Passive Mode Locking". Phys. Rev. Lett. 112, 223901 (2014).

[15] Sebastien Coetmellec Marc Brunel Huanhuan Shen and Denis Lebrun. "Extended ABCD matrix formalism for the description offemtosecond diffraction patterns; application tofemtosecond digital in-line holography withanamorphic optical systems". Rouvray cedex, France (2012).

[16] Afric S Meijer. "Coherent far-infrared excitation processes with ultrafast pulses in multilevel systems". Journal of Physics D-applied Physics, 2008/01/01.

[17] Francisco Melo Harry L. Swinney Paul B. Umbanhowar. "Localized excitations in a vertically vibrated granular layer". Nature volume 382, pages793–796 (1996).

[18] N. N. Rosanov and S. V. Fedorov. "Diffraction switching waves and autosolitons in a saturable-absorber laser". Opt. Spectrosc. 72, 782 (1992).

[19] M. Brambilla L. A. Lugiato S. Balle M. Giudici T. Maggipinto L. Spinelli G. Tissoni T. Knodl M. Miller S. Barland J. R. Tredicce and R. Jager. “Cavity solitons as pixels in semiconductor microcavities”. Appl. Phys. B, vol 88, pp 493, 2007.

[20] H.Uecker D.Wetzel S.Engelkemper S.V. Gurevich and U.Thiele. “Continuation for thin film hydrodynamics and related scalar problems”. Springer International Publishing AG, part of Springer Nature 2019.

[21] Rüdiger Seydel. “Practical Bifurcation and Stability Analysis.” Springer, third edition, 2010.

[22] Pablo U. Suarez. “An introduction to the split step fourier method using matlab”. 2013.

[23] J. Javaloyes S.V. Gurevich. “Spatial instabilities of light bullets in passively-mode-locked lasers”. Phys. Rev. A. 96, 023821 (2017).

[24] Martin Hoffmann et al. Valentin J. Wittwer Mario Mangold. “MIXSEL: Pikosekunden-Halbleiterscheibenlaser mit integriertem sättigbaren Absorber”. Photonik vol. 5, pp. 54-56, 2012.

I want to thank Svetlana Gurevich and Julien Javaloyes for the perfect mentoring of my master's thesis. Especially Svetlana Gurevich for her patient, very kind and always helping assistance and Julien Javaloyes for his help with the mathematical framework of the master's thesis and his entertaining comments in the provided materials.

Declaration of Academic Integrity

I hereby confirm that this thesis on *Spatial Localization in coupled nonlinear Micro-Cavities near self-imaging Conditions* is solely my own work and that I have used no sources or aids other than the ones stated. All passages in my thesis for which other sources, including electronic media, have been used, be it direct quotes or content references, have been acknowledged as such and the sources cited.

2th March 2022 L. Jäckel
(date and signature of student)

I agree to have my thesis checked in order to rule out potential similarities with other works and to have my thesis stored in a database for this purpose.

2th March 2022 L. Jäckel
(date and signature of student)